Measurement of the Branching Fraction And Search for Direct CP-Violation in the B+- --> J/Psi Pi+- Decay Mode at BaBar

Francesco Fabozzi

SLAC-R-837

Prepared for the Department of Energy
under contract number DE-AC02-76SF00515

Printed in the United States of America. Available from the National Technical Information Service, U.S. Department of Commerce, 5285 Port Royal Road, Springfield, VA 22161.

This document, and the material and data contained therein, was developed under sponsorship of the United States Government. Neither the United States nor the Department of Energy, nor the Leland Stanford Junior University, nor their employees, nor their respective contractors, subcontractors, or their employees, makes an warranty, express or implied, or assumes any liability of responsibility for accuracy, completeness or usefulness of any information, apparatus, product or process disclosed, or represents that its use will not infringe privately owned rights. Mention of any product, its manufacturer, or suppliers shall not, nor is it intended to, imply approval, disapproval, or fitness of any particular use. A royalty-free, nonexclusive right to use and disseminate same of whatsoever, is expressly reserved to the United States and the University.

Università degli Studi di Napoli "Federico II"

Dottorato di Ricerca in Fisica Fondamentale ed Applicata
XIV ciclo 1998-2001

Francesco Fabozzi

Measurement of the branching fraction and search for direct CP-violation in the $B^{\pm} \to J/\psi\,\pi^{\pm}$ decay mode at *BABAR*

A thesis submitted for the degree of Doctor of Philosophy

Advisor: **Prof. Crisostomo Sciacca**

Coordinator: **Prof. Renato Musto**

Contents

Introduction

The phenomenon of CP-violation in weak interactions, discovered in 1964 in decays of neutral kaons, receives a simple and elegant explanation in the Standard Model with three generations of quarks. Indeed, in this model the common source of CP-asymmetry phenomena is represented by a simple complex phase in the unitary matrix (the Cabibbo-Kobayashi-Maskawa matrix) describing the charged weak couplings of the quarks.

This simple scheme has never received an accurate validation, because the phenomenological parameters determined from measurements of CP-violation in kaons decays are related to the fundamental parameters of the theory in a complex way, sensitive to large theoretical uncertainties. On the contrary, decays of neutral B mesons like $B^0 \to J/\psi\, K^0_S$ represent a unique laboratory to test the predictions of the theory because they are expected to show significant CP-violation effects, the magnitude of which is cleanly related to the Standard Model parameters. Thus experimental facilities have been built with the purpose of performing extensive studies of B decays.

The *BABAR* experiment is operating at one of these facilities, at the Stanford Linear Accelerator Center. It is collecting data at the PEP-II asymmetric e^+e^- collider ($E_{e^-} = 9.0\,\mathrm{GeV}$; $E_{e^+} = 3.1\,\mathrm{GeV}$), a high-luminosity accelerator machine ($\mathcal{L} = 3 \times 10^{33}\, cm^{-2}s^{-1}$). The center-of-mass energy ($10.58\,\mathrm{GeV}$) of the e^+e^- system at PEP-II allowes resonant production of the $\Upsilon(4S)$, a $b\overline{b}$ bound state, which decays almost exclusively in a $B^0\overline{B}^0$ or a B^+B^- pair. A high-acceptance detector, projected and built by a wide international collaboration, detects and characterizes the decay products of the B mesons. From the analysis of the data collected during the first two years of operation, the *BABAR* collaboration has established CP-violation in decays of neutral B mesons at the 4.1σ level.

Besides the primary goal of CP-violation studies, the high luminosity of PEP-II, coupled with the high acceptance of the *BABAR* detector, allowes

competitive studies of the properties of a wide set of B decay modes. In particular, measurements of non-leptonic decays are extremely useful to understand the dynamics of the non-perturbative strong interactions involved in these processes.

In this thesis a study of the non-leptonic decay mode $B^{\pm} \to J/\psi\,\pi^{\pm}$ is presented. This channel is Cabibbo-suppressed, and its branching fraction is expected to be of the order of 10^{-5}. Detailed predictions are obtained using the hypothesis of factorization of the hadronic matrix elements, a theoretical approach widely used in the treatment of non-leptonic decays of heavy mesons. However, the absence of strong theoretical arguments supporting factorization and the use of phenomenological models, which are source of theoretical uncertainties, weaken the reliability of these predictions, that need to be accurately tested on data. Furthermore, significant interference terms between the suppressed tree and penguin amplitudes could be the source of significant direct *CP*-violation at the few percent level. No searches for direct *CP*-violation in this channel have been previously performed.

The analysis reported here is based on data recorded in 1999-2000 with the *BABAR* detector; the integrated luminosity is $20.7\,\mathrm{fb}^{-1}$, corresponding to 22.7 million $B\overline{B}$ pairs. A measurement of the ratio of branching fractions $\mathcal{B}(B^{\pm} \to J/\psi\,\pi^{\pm})/\mathcal{B}(B^{\pm} \to J/\psi\,K^{\pm})$, along with a search for direct *CP*-violation in $B^{\pm} \to J/\psi\,\pi^{\pm}$ and $B^{\pm} \to J/\psi\,K^{\pm}$ decays, is described. Since the Standard Model does not predict a significant direct *CP*-violation in the $B^{\pm} \to J/\psi\,K^{\pm}$ channel, it has been used as a control mode to test the analysis for the asymmetry determination. The high luminosity recorded by the *BABAR* detector allowes a significant improvement in the statistical precision of the measurements.

The present thesis is organized in five chapters. Chapters 1 and 2 represent an introduction to the *BABAR* experiment. The *CP*-violation in the framework of the Standard Model and its manifestations in the phenomenology of B decays are discussed in Chapter 1, while Chapter 2 is devoted to a detailed description of the *BABAR* detector, built around the e^+e^- interaction region of PEP-II. Chapter 3 is a brief introduction to the study of the $B^{\pm} \to J/\psi\,\pi^{\pm}$ mode, in which the theoretical expectations are discussed. The remaining part of the thesis gives a detailed description of the analysis developed to study the $B^{\pm} \to J/\psi\,\pi^{\pm}$ channel. A sample of $B^{\pm} \to J/\psi\,h^{\pm}$ ($h = \pi, K$) decays is fully reconstructed, and the yields and *CP*-violating charge asymmetries are determined from an unbinned maximum likelihood

fit that exploits the kinematics of the decay to identify the $B^{\pm} \to J/\psi\,\pi^{\pm}$, $B^{\pm} \to J/\psi\,K^{\pm}$, and background components in the sample. The measurement of $\mathcal{B}(B^{\pm} \to J/\psi\,\pi^{\pm})/\mathcal{B}(B^{\pm} \to J/\psi\,K^{\pm})$ is reported in Chapter 4, while Chapter 5 describes the study of direct CP-violation in the $B^{\pm} \to J/\psi\,\pi^{\pm}$ and $B^{\pm} \to J/\psi\,K^{\pm}$ channels.

A signal of 51 ± 10 $B^{\pm} \to J/\psi\,\pi^{\pm}$ events is observed, and the ratio $\mathcal{B}(B^{\pm} \to J/\psi\,\pi^{\pm})/\mathcal{B}(B^{\pm} \to J/\psi\,K^{\pm})$ that has been determined is in agreement with previous measurements and with the Standard Model expectation. No evidence of direct CP-violation in the $B^{\pm} \to J/\psi\,\pi^{\pm}$ and $B^{\pm} \to J/\psi\,K^{\pm}$ channels has been found. This confirms the Standard Model expectation for $B^{\pm} \to J/\psi\,K^{\pm}$ decays.

Chapter 1

CP-violation in B mesons decays

This chapter is a theoretical introduction to the study of CP-violation in the decays of B mesons, which is the primary goal of the *BABAR* experiment. We first introduce the Cabibbo-Kobayashi-Maskawa matrix, which describes the flavor-changing weak couplings between the quarks: in the Standard Model it contains the source of CP-violation. Then we discuss the three possible manifestations of CP-asymmetries in B mesons phenomenology (CP-violation in decay, CP-violation in mixing, and from interference between mixing and decay). Finally, we show that in certain decays of neutral B mesons a measurement of the time-dependent CP-violation allowes a clean test of the Standard Model predictions.

1.1 CP-violation in the Standard Model

The Standard Model (SM) of the electro-weak interactions [1, 2, 3] is a gauge theory based on the $SU(2)_L \times U(1)_Y$ symmetry group. Considering only the quark sector, the fermion fields are divided into three generations of the following SU(2) multiplets:

$$Q_L^I = \begin{pmatrix} u_L^I \\ d_L^I \end{pmatrix}, u_R^I, d_R^I \,. \tag{1.1}$$

With the symbols u_L^I (u_R^I)and d_L^I (d_R^I) we denote the left-handed (right-handed) components of the up-type (u, c, t) and down-type (d, s, b) weak

eigenstates of the quarks, respectively. They interact with the $SU(2)_L \times U(1)_Y$ gauge bosons according to the following Lagrangian:

$$\begin{aligned} -L_{ew} &= \sum_i \bar{Q}^I_{Li}\gamma^\mu \left(g\vec{T}\cdot\vec{W}_\mu + \frac{1}{2}g'YB_\mu \right) Q^I_{Li} + \\ &+ \bar{u}^I_{Ri}\gamma^\mu \left(\frac{1}{2}g'YB_\mu \right) u^I_{Ri} + \bar{d}^I_{Ri}\gamma^\mu \left(\frac{1}{2}g'YB_\mu \right) d^I_{Ri} \,. \end{aligned} \tag{1.2}$$

In Eq. 1.2 we have denoted with g, $\vec{T}$, $\vec{W}_\mu$ and g', Y, B_μ the coupling constants, the generators and the gauge fields of $SU(2)_L$ and $U(1)_Y$ respectively; the index i runs over the three quarks generations.

In order to preserve the gauge invariance and therefore the renormalizability of the theory, the masses of the gauge bosons are generated by spontaneous symmetry breaking of $SU(2)_L \times U(1)_Y$. This mechanism requires the introduction of an SU(2) doublet of scalar fields:

$$\Phi = \begin{pmatrix} \phi^+(x) \\ \phi^0(x) \end{pmatrix} , \tag{1.3}$$

with vacuum expectation value $\langle\Phi\rangle_0 = v \neq 0$. The scalar fields in Eq. 1.3 are coupled with the fermion fields through the following Yukawa interaction:

$$-L_Y = \sum_{ij} F_{ij}\bar{Q}^I_{Li}\Phi u^I_{Rj} + G_{ij}\bar{Q}^I_{Li}\Phi d^I_{Rj} + h.c. \,, \tag{1.4}$$

where the indices i, j run over the quarks generations, and F_{ij}, G_{ij} are in general complex matrices.

Denoting with Φ_0 a particular vacuum state:

$$\Phi_0 = \frac{1}{\sqrt{2}} \begin{pmatrix} 0 \\ v \end{pmatrix} ,$$

and exploiting the gauge symmetry of the Lagrangian, we can write the field Φ in the following "expanded" form around Φ_0:

$$\Phi = \begin{pmatrix} \phi^+(x) \\ \phi^0(x) \end{pmatrix} \rightarrow \frac{1}{\sqrt{2}} \begin{pmatrix} 0 \\ v + h(x) \end{pmatrix} , \tag{1.5}$$

that, substituted in Eq. 1.4 generates the mass terms of the quarks:

$$-L_M = \frac{1}{\sqrt{2}}v \sum_{i,j} F_{ij}\bar{u}^I_{Li}u^I_{Rj} + \frac{1}{\sqrt{2}}v \sum_{i,j} G_{ij}\bar{d}^I_{Li}d^I_{Rj} + h.c. \,. \tag{1.6}$$

In general, the weak (or interaction) eigenstates (that we have denoted so far with the superscript I) are different from the mass eigenstates, and the mass matrices:

$$M_u = \frac{1}{\sqrt{2}} vF \tag{1.7}$$

$$M_d = \frac{1}{\sqrt{2}} vG \tag{1.8}$$

are not diagonal. After the diagonalization of the mass matrices, performed with the introduction of four unitary matrices V_{uL}, V_{uR}, V_{dL}, V_{dR} such that:

$$M_u^{Diag} = V_{uL} M_u V_{dR}^\dagger \tag{1.9}$$

$$M_d^{Diag} = V_{dL} M_d V_{uR}^\dagger \,, \tag{1.10}$$

Eq. 1.6 becomes:

$$-L_M = \sum_i (M_u^{Diag})_{ii} \bar{u}_{Li} u_{Ri} + \sum_i (M_d^{Diag})_{ii} \bar{d}_{Li} d_{Ri} + h.c. \,, \tag{1.11}$$

and the charged current weak interactions in the Lagrangian L_{ew} assume the following form:

$$-L_{CC} = \frac{g}{2\sqrt{2}} \sum_{i,j} \bar{u}_{Li} \gamma^\mu V_{ij} d_{Lj} W_\mu^\dagger + h.c. \,. \tag{1.12}$$

In Eq. 1.12 with the symbols u and d we have denoted the mass eigenstates of the quarks, W_μ is the field of the weak boson $W^\pm$, and $V = V_{uL} V_{dL}^\dagger$ represents the unitary mixing matrix for the quarks generations, known as the Cabibbo-Kobayashi-Maskawa (CKM) matrix [4]:

$$V_{CKM} = \begin{pmatrix} V_{ud} & V_{us} & V_{ub} \\ V_{cd} & V_{cs} & V_{cb} \\ V_{td} & V_{ts} & V_{tb} \end{pmatrix} \,. \tag{1.13}$$

The generic element $V_{q_1 q_2}$ describes the strength of the flavor-changing weak coupling between the quarks q_1 and q_2.

Even if it is evident the deep connection of the CKM matrix elements with the quarks masses generation, the SM does not provide any mechanism to derive their values, which are considered input parameters of the theory and need to be inferred from experimental data.

1.1.1 Parameterizations of the CKM matrix

In a generic $n \times n$ complex matrix there are $2n^2$ real parameters. Unitarity of the matrix ($VV^\dagger = 1$) implies n real constraints $\sum_{q_2} |V_{q_1 q_2}|^2$ (normalization of each row) and $n(n-1)/2$ complex constraints $\sum_{q_2} V^*_{q_3 q_2} V_{q_1 q_2}$ (orthogonality of each pair of rows) that reduce the number of independent real parameters to n^2. Exploiting the degree of freedom in the definition of the phases of the quarks fields we can still eliminate $2n-1$ unphysical phases, and leave in the matrix only $(n-1)^2$ independent and physical parameters.

In a model with two generation of quarks [5] there is just one independent parameter represented by a rotation angle in a two-dimensional space: the Cabibbo angle θ_C [6]. In the SM model with three generations of quarks there are instead four independent parameters represented by three rotation angles and a complex phase. Since the transformation properties of the fields in Eq. 1.12 imply that L_{CC} is invariant under a *CP*-transformation only if $V_{ij} = V^*_{ij}$, the complex phase in the CKM matrix is essential to account for *CP*-violation in weak interactions, a phenomenon discovered in 1964 in decays of neutral kaons [7]. Furthermore, it is evident that *CP*-violation is forbidden in a model with just two generations of quarks.

Several equivalent parameterizations for the CKM matrix have been developed, differing for the particular choice of the arbitrary phase of the quarks fields.

In the *standard parameterization* [8] the CKM matrix is explicitly written in terms of three rotation angles θ_{ij} and a complex phase δ:

$$V_{CKM} = \begin{pmatrix} c_{12}c_{13} & s_{12}c_{13} & s_{13}e^{-i\delta} \\ -s_{12}c_{23} - c_{12}s_{23}s_{13}e^{i\delta} & c_{12}c_{23} - s_{12}s_{23}s_{13}e^{i\delta} & s_{23}c_{13} \\ s_{12}s_{23} - c_{12}c_{23}s_{13}e^{i\delta} & -s_{23}c_{12} - s_{12}c_{23}s_{13}e^{i\delta} & c_{23}c_{13} \end{pmatrix},$$

where $c_{ij} = \cos\theta_{ij}$ and $s_{ij} = \sin\theta_{ij}$. The small measured value of V_{ub} ($|V_{ub}| = s_{13} \sim 10^{-3}$) implies $c_{13} \sim 1$, and with these approximations the matrix becomes:

$$V_{CKM} = \begin{pmatrix} c_{12} & s_{12} & s_{13}e^{-i\delta} \\ -s_{12}c_{23} & c_{12}c_{23} & s_{23} \\ s_{12}s_{23} - c_{12}c_{23}s_{13}e^{i\delta} & -s_{23}c_{12} & c_{23}c_{13} \end{pmatrix}, \tag{1.14}$$

where it is evident that the dominant terms carrying the phase factor are V_{ub} and V_{td}.

In the *Wolfenstein parameterization* [9] the empirical hierarchy of the CKM matrix elements is shown explicitly through an expansion in powers of the parameter $\lambda = sin\,\theta_C \sim 0.22$:

$$V_{CKM} = \begin{pmatrix} 1-\frac{\lambda^2}{2} & \lambda & A\lambda^3(\rho - i\eta) \\ -\lambda & 1-\frac{\lambda^2}{2} & A\lambda^2 \\ A\lambda^3(1-\rho-i\eta) & -A\lambda^2 & 1 \end{pmatrix} + O(\lambda^4)\,. \quad (1.15)$$

In this representation the four independent parameters of the matrix are (λ, A, ρ, η), and $\eta \neq 0$ is responsible for the complex phase.

1.1.2 The Unitarity Triangle

From the orthogonality of two rows or two columns of the CKM matrix we obtain the following six equations:

$$\begin{aligned}
(ds) \quad V_{ud}V_{us}^* + V_{cd}V_{cs}^* + V_{td}V_{ts}^* &= 0 && (1.16)\\
(db) \quad V_{ud}V_{ub}^* + V_{cd}V_{cb}^* + V_{td}V_{tb}^* &= 0 && (1.17)\\
(sb) \quad V_{us}V_{ub}^* + V_{cs}V_{cb}^* + V_{ts}V_{tb}^* &= 0 && (1.18)\\
(uc) \quad V_{ud}V_{cd}^* + V_{us}V_{cs}^* + V_{ub}V_{cb}^* &= 0 && (1.19)\\
(ut) \quad V_{ud}V_{td}^* + V_{us}V_{ts}^* + V_{ub}V_{tb}^* &= 0 && (1.20)\\
(ct) \quad V_{cd}V_{td}^* + V_{cs}V_{ts}^* + V_{cb}V_{tb}^* &= 0\,, && (1.21)
\end{aligned}$$

that can be interpreted as closure relations of triangles in the complex plane. Each term in a sum represents a side of the corresponding triangle. Using the Wolfenstein parameterization we can investigate the relative magnitude of the sides:

$$\begin{aligned}
&(ds) \quad O(\lambda) + O(\lambda) + O(\lambda^5)\\
&(db) \quad O(\lambda^3) + O(\lambda^3) + O(\lambda^3)\\
&(sb) \quad O(\lambda^4) + O(\lambda^2) + O(\lambda^2)\\
&(uc) \quad O(\lambda) + O(\lambda) + O(\lambda^5)\\
&(ut) \quad O(\lambda^4) + O(\lambda^2) + O(\lambda^2)\\
&(ct) \quad O(\lambda^5) + O(\lambda^3) + O(\lambda^3)\,.
\end{aligned}$$

We can see that the (db) triangle has the property that all the sides, which are related to b quark transitions, are of comparable magnitude. The opening

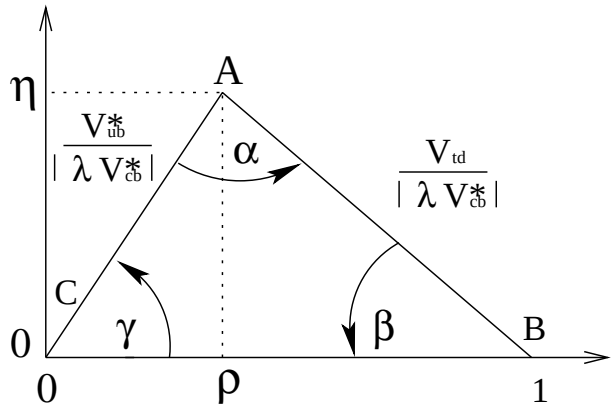

Figure 1.1: The normalized Unitarity Triangle

of this triangle has important implications for the phenomenology of *CP*-violation in decays of B mesons. Indeed, the internal angles α, β, γ:

$$\begin{aligned} \alpha &= Arg\left(-\frac{V_{td}V^*_{tb}}{V_{ud}V^*_{ub}}\right) \\ \beta &= Arg\left(-\frac{V_{cd}V^*_{cb}}{V_{td}V^*_{tb}}\right) \\ \gamma &= Arg\left(-\frac{V_{ud}V^*_{ub}}{V_{cd}V^*_{cb}}\right) \end{aligned} \tag{1.22}$$

are physically meaningful quantities that govern the strength of the *CP*-asymmetry in B decays, and in some cases they can be measured quite directly from data (see Section 1.3.1). For its importance the (db) triangle is known as the Unitarity Triangle.

From the Wolfenstein parameterization, and neglecting terms of $O(\lambda^4)$, the Unitarity Triangle is defined by the following equation:

$$V^*_{ub} + \lambda V^*_{cb} + V_{td} \sim 0\,, \tag{1.23}$$

and, after the normalization of the sides by $|\lambda V^*_{cb}|$, it is represented by the triangle in Fig. 1.1, which is completely determined by the position of the upper vertex A of coordinates (ρ, η). If $\eta = 0$ (no complex phase in the CKM matrix, and therefore no *CP*-violation) the triangle collapses on the real axis. In fact, it can demonstrated [10] that all the triangles in Equations 1.16 - 1.21 have the same area, independent of the parameterization of the CKM matrix,

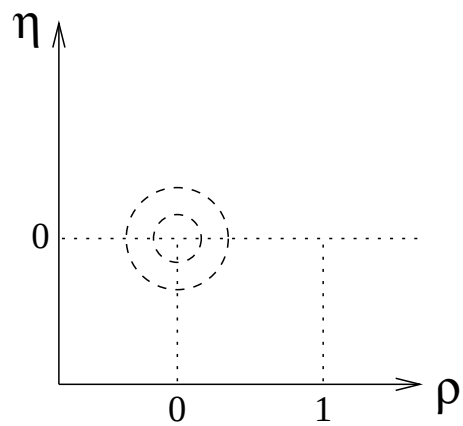

Figure 1.2: Annular constraint from $|V_{cb}|$ and $|V_{ub}|$ measurements. The dashed curves represent the boundaries of the allowed region for the vertex A of the Unitarity Triangle.

and their non-degeneration represents a general condition for *CP*-violation in the SM.

1.1.3 Constraints on the Unitarity Triangle

Experimental results can be used to constrain the position of the vertex A of the Unitarity Triangle. Because of experimental and theoretical uncertainties, each constraint is equivalent to an allowed region for A in the (ρ, η) plane. The intersection of all these regions represents the SM prediction for the Unitarity Triangle.

Measurements of $|V_{cb}|$ and $|V_{ub}|$ provide the constraint:

$$\frac{|V_{ub}|}{\lambda |V_{cb}|} = \sqrt{\rho^2 + \eta^2}\,. \tag{1.24}$$

It is represented, when errors are taken into account, by an annulus in the (ρ, η) plane centered at $(0, 0)$ (see Fig. 1.2).

Determinations of the B_d-$\overline{B}_d$ oscillation frequency (given by Δm_{B_d}, the mass difference between the heavy and the light B_d states) are sensitive to $|V_{td}V_{tb}^*|$ because of the dominance of the box diagram with an intermediate $t\bar{t}$ state (shown in Fig. 1.3). The following constraint is obtained:

$$|V_{td}V_{tb}^*| = A\lambda^3 \sqrt{(1-\rho)^2 + \eta^2}\,, \tag{1.25}$$

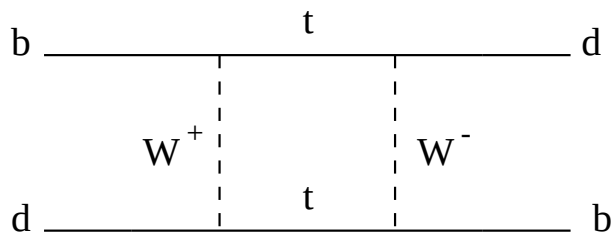

Figure 1.3: The dominant box diagram for the B_d-$\overline{B}_d$ mixing

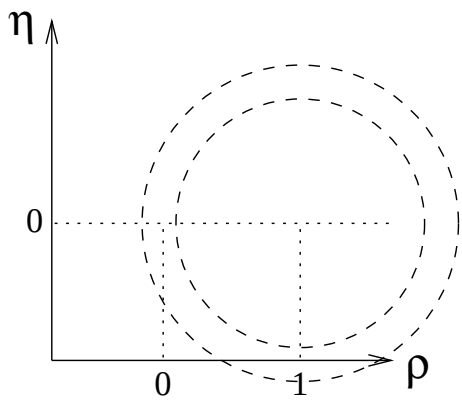

Figure 1.4: Annular constraint from Δm_{B_d} measurements. The dashed curves represent the boundaries of the allowed region for the vertex A of the Unitarity Triangle.

represented by an annulus in the (ρ, η) plane centered at $(1, 0)$ (see Fig. 1.4).

It is useful to consider also determinations of B_s-$\overline{B}_s$ oscillation frequency, sensitive to $|V_{ts}V_{tb}^*|$. Indeed, from the quantity $\Delta m_{B_d}/\Delta m_{B_s}$ the ratio:

$$\frac{|V_{td}|}{|V_{ts}|} = \lambda\sqrt{(1-\rho)^2 + \eta^2} \tag{1.26}$$

can be extracted with reduced theoretical uncertainties, improving the constraint from Δm_{B_d}.

Measurements of CP-violation in neutral kaon decays are sensitive to the phenomenological parameter ε_K, describing the amount of CP-violation in the mass matrix of the K^0-$\overline{K}^0$ system. To a good approximation:

$$\epsilon_K = \frac{e^{i\pi/4}}{\sqrt{2}\Delta M_K}\, Im[M_{12}]\,, \tag{1.27}$$

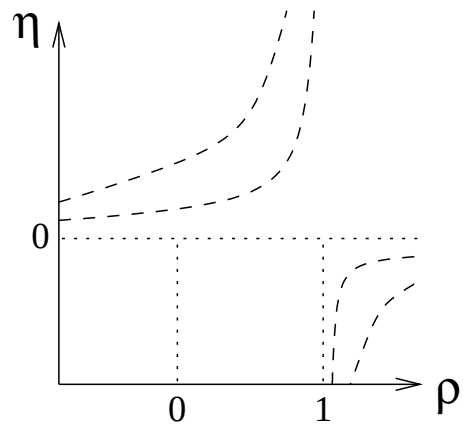

Figure 1.5: Hyperbolic constraint from $|\varepsilon_K|$ determinations. The dashed curves represent the boundaries of the allowed regions for the vertex A of the Unitarity Triangle.

where M_{12} is the off-diagonal element of the mass matrix and ΔM_K is the mass difference of the two neutral kaon states. Writing M_{12} in terms of the parameters of the CKM matrix and using the experimental value for ΔM_K it can be shown [11] that $|\varepsilon_K|$ provides a hyperbolic constraint in the (ρ, η) plane (see Fig. 1.5).

Several procedures have been developed to derive the prediction for the vertex A starting from experimental data. They differ primarily for the treatment of theoretical uncertainties, whose statistical nature is not Gaussian. Figure 1.6 summarizes the status of the constraints on the Unitarity Triangle, as reported by the 2000 Particle Data Group [12]. More conservative methods based on the "scanning" of the theoretical parameters within their allowed range [13], predict for $\sin 2\beta$ a value approximately between 0.4 and 0.8 at the 95% Confidence Level. We remark that these expectations are not based on CP-violation studies in B decays, and therefore the comparison with the measurements performed at *BABAR* will provide a test of the SM.

1.2 Phenomenology of CP-violation in B decays

In this section we describe the three model-independent mechanisms, and the corresponding conditions, leading to CP-violation effects in the phenomenology of B mesons decays.

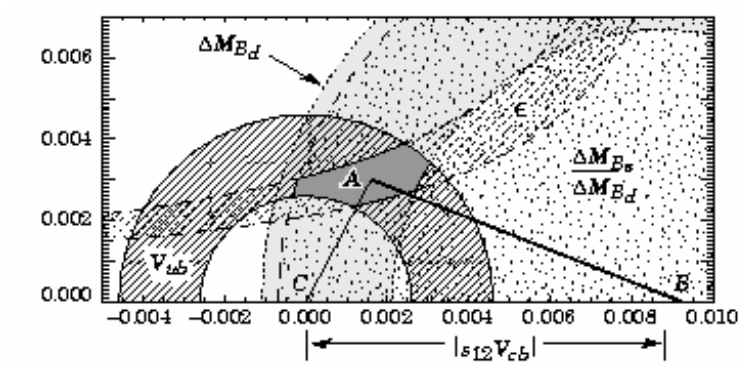

Figure 1.6: Summary of the constraints on the *Unitarity Triangle* from $|\frac{V_{ub}}{V_{cb}}|$, $|\varepsilon_K|$, Δm_{B_d} and Δm_{B_s} measurements. The shaded region represents the SM prediction for the A vertex.

1.2.1 *CP*-violation in decay

If A is the amplitude of a generic decay $B \to f$, described by the hamiltonian H:

$$A \equiv < f|H|B > ,$$

the hypothesis of *CP*-conservation (equivalent to $(CP)^\dagger H(CP) = H$) implies:

$$\begin{aligned} A &= < f|(CP)^\dagger(CP)H(CP)^\dagger(CP)|B >= \\ &= < f|(CP)^\dagger H(CP)|B >=< \bar{f}|H|\bar{B} > e^{2i(\theta_B-\theta_f)} , \end{aligned}$$

where the phases $\theta_{B,f}$, parameterizing the chosen *CP*-phase convention, are defined through:

$$CP|B > = e^{2i\theta_B}|\overline{B} > \tag{1.28}$$

$$CP|f > = e^{2i\theta_f}|\bar{f} > . \tag{1.29}$$

Therefore *CP*-conservation implies the following relation between the amplitude A and the amplitude $\bar{A}$ of the *CP*-conjugate decay $\overline{B} \to \overline{f}$:

$$A = \bar{A}e^{2i(\theta_B-\theta_f)} , \tag{1.30}$$

and considering the magnitudes of the amplitudes we obtain:

$$\left|\frac{\bar{A}}{A}\right| = 1 , \tag{1.31}$$

which is independent of the phase convention and implies a physically meaningful condition for CP-violation:

$$\left|\frac{\bar{A}}{A}\right| \neq 1 \Rightarrow \textit{ CP-violation in decay.} \tag{1.32}$$

In general, several contributions will determine the amplitude A:

$$A = \sum_k a_k e^{i\phi_k} e^{i\delta_k} \ , \tag{1.33}$$

where the phases ϕ_k and δ_k have different origins. The phases ϕ_k are due to the elements of the CMK matrix (*weak phases*) and, since $\overline{B} \to \overline{f}$ involves complex-conjugate CMK elements, they change sign under CP. The phases shifts δ_k are due to hadronic final-state interactions (*strong phases*) and therefore they are CP-invariant. Writing explicitly the amplitude $\bar{A}$:

$$\bar{A} = e^{-2i(\theta_B - \theta_f)} \sum_k a_k e^{-i\phi_k} e^{i\delta_k} \tag{1.34}$$

we obtain:

$$|\bar{A}|^2 - |A|^2 = 2 \sum_{k,j} |a_k||a_j| \sin(\phi_k - \phi_j) \sin(\delta_k - \delta_j) \ , \tag{1.35}$$

which means that CP-violation in decay can occur only if there are at least two contributions to the amplitude A with different weak and strong phases.

CP-violation in decay (also called direct CP-violation) implies $\Gamma(B \to f) \neq \Gamma(\overline{B} \to \overline{f})$ or, in terms of the asymmetry $\mathcal{A}$:

$$\mathcal{A} \equiv \frac{\Gamma(B \to f) - \Gamma(\overline{B} \to \overline{f})}{\Gamma(B \to f) + \Gamma(\overline{B} \to \overline{f})} \neq 0 \ . \tag{1.36}$$

This type of CP-violation can be studied in decays of charged B mesons, in which effects due to B-$\overline{B}$ mixing are absent and the charge of the final state provides directly the flavor of the B (*self-tagging*). Unfortunately, measurements cannot be easily related to fundamental CKM parameters since large theoretical uncertainties affect the knowledge of the contributions to the amplitude.

While direct CP-violation in B decays has not yet been observed, experimental results have finally established the existence of this phenomenon in decays of neutral K mesons [14].

1.2.2 CP-violation in mixing

Weak interactions are responsible for the oscillation of neutral mesons like K^0, D^0 and B^0 into the corresponding antiparticle state. This phenomenon can be described with the simple quantum-mechanics formalism for a two-level system characterized by the Hamiltonian $H = H_0 + H_W$, where H_0 is due to strong and electromagnetic interactions and H_W is due to weak interactions. In the following we will consider the B^0-$\overline{B}^0$ system, but the formalism we will develop is quite general and can be extended to other systems as well.

The term H_0 is flavor-conserving and determines the production of the system. The term H_W violates the flavor quantum number and determines the evolution of the system and the decay of the particles. Thus the two-by-two matrix H is in general not diagonal in the flavor eigenstates basis $(|B>, |\overline{B}>)$ and mixing can occur. Furthermore, since $|B>$ and $|\overline{B}>$ are not stable states the matrix H is not hermitean. However, it can be written as the combination of two hermitean matrices, M (the mass matrix) and Γ (the decay matrix):

$$H = M - \frac{i}{2}\Gamma \,. \tag{1.37}$$

The CPT theorem [15] implies the following form for these matrices:

$$\begin{pmatrix} H_{11} & H_{12} \\ H_{21} & H_{22} \end{pmatrix} = \begin{pmatrix} M & M_{12} \\ M_{12}^* & M \end{pmatrix} - \frac{i}{2}\begin{pmatrix} \Gamma & \Gamma_{12} \\ \Gamma_{12}^* & \Gamma \end{pmatrix} \,. \tag{1.38}$$

Using perturbations theory it is possible to show [16] that:

$$\begin{aligned} M_{ij} &= m_0\delta_{ij} + < i|H_{W,\Delta B=2}|j > + \mathcal{P}\sum_n \frac{< i|H_{W,\Delta B=1}|n >< n|H_{W,\Delta B=1}|j >}{M_B - E_n} \\ \Gamma_{ij} &= 2\pi \sum_n < i|H_{W,\Delta B=1}|n >< n|H_{W,\Delta B=1}|j > \delta(m_0 - E_n) \,, \end{aligned}$$

that establish the following properties of the mass and decay matrices:

1. The diagonal elements M of the mass matrix are dominated by the eigenvalue m_0 of the unperturbed Hamiltonian H_0.

2. Since $\Delta B = 2$ transitions are forbidden at the first order in the SM, the off-diagonal elements of the mass matrix can only be due to second order B^0-$\overline{B}^0$ transitions via off-shell intermediate states.

3. The diagonal elements Γ of the decay matrix receive contribution from all the allowed decay channels of B^0 and $\overline{B}^0$.

4. The off-diagonal elements of the decay matrix are due to to second order B^0-$\overline{B}^0$ transitions via on-shell intermediate states.

The eigenvectors $|B_+>$ and $|B_->$ of the Hamiltonian H, that we can write as a linear combination of the flavor eigenstates:

$$|B_\pm >\equiv \frac{1}{\sqrt{|p|^2+|q|^2}}\left(p|B>\pm q|\overline{B}>\right) \ ,$$

are found solving the secular equation:

$$H|B_\pm >= \mu_\pm |B_\pm > \ . \tag{1.39}$$

The solutions satisfy:

$$\frac{q}{p}=\left(\frac{H_{21}}{H_{12}}\right)^{1/2}=\sqrt{\frac{M_{12}^*-\frac{i}{2}\Gamma_{12}^*}{M_{12}-\frac{i}{2}\Gamma_{12}}} \ , \tag{1.40}$$

and the corresponding eigenvalues are:

$$\mu_\pm = H_{11}\pm (H_{12}H_{21})^{1/2}\equiv M_\pm - \frac{i}{2}\Gamma_\pm \ , \tag{1.41}$$

where we have defined:

$$M_\pm = M\pm Re[(H_{12}H_{21})^{1/2}] \tag{1.42}$$

$$\Gamma_\pm = \Gamma\mp 2\,Im[(H_{12}H_{21})^{1/2}] \ . \tag{1.43}$$

The mass and width differences $\Delta M\equiv M_- - M_+$ and $\Delta\Gamma\equiv\Gamma_- - \Gamma_+$ are thus given by:

$$\Delta M = -2\,Re[(H_{12}H_{21})^{1/2}] \tag{1.44}$$

$$\Delta\Gamma = 4\,Im[(H_{12}H_{21})^{1/2}] \ . \tag{1.45}$$

If CP is conserved, we expect that the eigenstates of the Hamiltonian concide with the CP-eigenstates. In addition, with an argument similar to the one used to derive Eq. 1.30, it is possible to show that CP-conservation implies:

$$e^{4i\theta_B}(M_{12}-\frac{i}{2}\Gamma_{12})=M_{12}^*-\frac{i}{2}\Gamma_{12}^* \ , \tag{1.46}$$

where θ_B is the arbitrary phase defined in Eq. 1.29. Consequently:

$$\frac{q}{p} = \sqrt{\frac{M_{12}^* - \frac{i}{2}\Gamma_{12}^*}{M_{12} - \frac{i}{2}\Gamma_{12}}} = e^{i(2\theta_B + n\pi)} \quad n = 0, 1, 2, \ldots \quad , \tag{1.47}$$

and the phase convention independent quantity $|q/p|$ represents an observable sensitive to CP-violation:

$$\left|\frac{q}{p}\right| \neq 1 \Rightarrow \textit{ CP-violation in mixing} \; . \tag{1.48}$$

If CP is violated in mixing, the probability of the transition $B^0 \to \overline{B}^0$ will differ from the probability of the transition $\overline{B}^0 \to B^0$.

This type of CP-violation is suppressed for a B-$\overline{B}$ system. Indeed, since the mixing amplitude is dominated by the (off-shell) $t\bar{t}$ intermediate state, we can write to a good approximation:

$$H_{12} \sim M_{12} \Rightarrow H_{12}H_{21} \sim |M_{12}|^2 \tag{1.49}$$

that implies:

$$\frac{\Delta\Gamma}{\Gamma} \ll 1 \tag{1.50}$$

and:

$$\frac{q}{p} \sim \sqrt{\frac{M_{12}^*}{M_{12}}} \Rightarrow \left|\frac{q}{p}\right| \sim 1 \; . \tag{1.51}$$

We conclude this discussion noting that Eq. 1.50 and Eq. 1.51 are not necessarily satisfied for other neutral mesons systems. For instance, the long-lived eigenstate of the K^0-$\overline{K}^0$ system (K_L^0) is characterized by a width which is two orders of magnitude smaller than the short-lived eigenstate (K_S^0), and the CP-violation in mixing (described by the parameter ε_K already introduced in Section 1.1.3) is a well established phenomenon [17].

1.2.3 *CP*-violation in interference between mixing and decay

The time evolution $B(t)$ of an initially pure B^0 state is obtained solving the time-dependent Schröedinger equation:

$$i\frac{d}{dt}\begin{pmatrix} a \\ b \end{pmatrix} = H \begin{pmatrix} a \\ b \end{pmatrix} \tag{1.52}$$

with the initial conditions $a(0) = 1$, $b(0) = 0$, if the equation is projected onto the $(|B>,|\overline{B}>)$ basis. We obtain:

$$B(t) = f_+(t)\,|B> + \frac{q}{p}\,f_-(t)\,|\overline{B}>\,, \tag{1.53}$$

where:

$$f_\pm(t) = \frac{1}{2}(e^{-i\mu_+ t} \pm e^{-i\mu_- t})\,. \tag{1.54}$$

Similarly, the time evolution $\overline{B}(t)$ of an initially pure $\overline{B}^0$ state is:

$$\overline{B}(t) = \frac{p}{q}\,f_-(t)\,|B> + f_+(t)\,|\overline{B}>\ . \tag{1.55}$$

From Eq. 1.50 we have: $\Gamma_+ \approx \Gamma_- \equiv \Gamma$. Defining $M \equiv (M_+ + M_-)/2$, we can write:

$$f_+(t) = e^{-\frac{\Gamma}{2}t}\,e^{-iMt}\,\cos\frac{\Delta M t}{2} \tag{1.56}$$

$$f_-(t) = ie^{-\frac{\Gamma}{2}t}\,e^{-iMt}\,\sin\frac{\Delta M t}{2}\,, \tag{1.57}$$

which, substituted in Eq. 1.53 and Eq. 1.55, gives for the two evolutions:

$$B(t) = e^{-\frac{\Gamma}{2}t}\,e^{-iMt}\left(\cos\frac{\Delta M t}{2}\,|B> + i\frac{q}{p}\,\sin\frac{\Delta M t}{2}\,|\overline{B}>\right) \tag{1.58}$$

$$\overline{B}(t) = e^{-\frac{\Gamma}{2}t}\,e^{-iMt}\left(i\,\frac{p}{q}\,\sin\frac{\Delta M t}{2}\,|B> + \cos\frac{\Delta M t}{2}\,|\overline{B}>\right)\,. \tag{1.59}$$

If we consider the decays $B \to f$ and $\overline{B} \to f$, in which f is a CP-eigenstate with eigenvalue η_{CP}:

$$CP|f>= \eta_{CP}|f> \qquad \eta_{CP} = \pm 1\quad, \tag{1.60}$$

the time-dependent decay amplitudes will be:

$$\begin{aligned} <f|H|B(t)> &= e^{-\frac{\Gamma}{2}t}\,e^{-iMt}\,A_f\ \times \\ &\times\ \left(\cos\frac{\Delta M t}{2} + i\,\frac{q}{p}\frac{\bar{A}_f}{A_f}\,\sin\frac{\Delta M t}{2}\right) \end{aligned} \tag{1.61}$$

$$\begin{aligned} <f|H|\overline{B}(t)> &= e^{-\frac{\Gamma}{2}t}\,e^{-iMt}\,iA_f\,\frac{p}{q}\,\times \\ &\times\ \left(\sin\frac{\Delta M t}{2} - i\,\frac{q}{p}\frac{\bar{A}_f}{A_f}\,\cos\frac{\Delta M t}{2}\right)\,, \end{aligned} \tag{1.62}$$

where $A_f \equiv < f|H|B >$ and $\bar{A}_f \equiv < f|H|\overline{B} >$.

Thus, the time-dependent probability for a state initially B^0 to decay to f is given by:

$$| < f|H|B(t) > |^2 = e^{-\Gamma t}\, |A_f|^2 \, [\, \frac{1}{2}\,(1+|\lambda|^2) \; + \\ + \frac{1}{2}\,(1-|\lambda|^2)\, \cos\Delta M t - \; Im\lambda \, \sin\Delta M t \,] \,, \tag{1.63}$$

where we have defined:

$$\lambda \equiv \frac{q}{p} \cdot \frac{\bar{A}_f}{A_f} \,, \tag{1.64}$$

and the analogue probability for a state initially $\overline{B}^0$ is:

$$| < f|H|\overline{B}(t) > |^2 = e^{-\Gamma t}\, |A_f|^2 \, |\frac{p}{q}|^2 \, [\, \frac{1}{2}\,(1+|\lambda|^2) \; - \\ - \frac{1}{2}\,(1-|\lambda|^2)\, \cos\Delta M t + \; Im\lambda \, \sin\Delta M t \,] \,. \tag{1.65}$$

Equation 1.63 and Eq. 1.65 can be combined in a time-dependent CP-asymmetry observable:

$$\mathcal{A}(t) \equiv \frac{\Gamma(B(t) \to f) - \Gamma(\overline{B}(t) \to f)}{\Gamma(B(t) \to f) + \Gamma(\overline{B}(t) \to f)} \tag{1.66}$$

obtaining:

$$\mathcal{A}(t) = \frac{(1-|\lambda|^2)\cos\Delta M t - 2\, Im\lambda \, \sin\Delta M t}{1+|\lambda|^2} \,, \tag{1.67}$$

where we have used the suppression of the CP-violation in mixing for the B^0-$\overline{B}^0$ system:

$$\left|\frac{q}{p}\right| = 1 \,. \tag{1.68}$$

It is evident that the parameter λ is a physically meaningful quantity that defines, through the condition:

$$\lambda \neq \pm 1 \tag{1.69}$$

another type of manifestation of CP-violation, the *CP-violation in the interference between mixing and decay.*

If the mode $B \to f$ is characterized by only one weak phase (no direct CP-violation) we have also:

$$\left|\frac{\bar{A}_f}{A_f}\right| = 1 \tag{1.70}$$

and:

$$|\lambda| = 1\,, \tag{1.71}$$

with the time-dependent CP-asymmetry becoming simply:

$$\mathcal{A}(t) = -Im\lambda\ \sin\Delta M t\,. \tag{1.72}$$

We remark the distinctive feature of this situation: when the decay is characterized by a unique weak phase, in the ratio $\bar{A}_f/A_f$ the dependence on the strong phases (source of theoretical uncertainties) cancel out, and λ becomes related only to the difference between the weak phases from mixing and decay, which is a function of the parameters of the CKM matrix.

1.3 CP-asymmetry measurement at a B-factory

B mesons are produced in decays of the $\Upsilon(4S)$ resonance: $\Upsilon(4S) \to B^0\overline{B}^0$ and $\Upsilon(4S) \to B^+B^-$. The $\Upsilon(4S)$ is a $b\overline{b}$ bound state of mass $M_{\Upsilon(4S)} = 10.58\,\mathrm{GeV}/c^2$, slightly above the threshold for decaying into a B mesons pair. C-conservation implies that the pair is produced in a $C = -1$ state, which constrains the time-dependent wave function of the system to the following form:

$$|\psi(t_1,t_2)> \propto \frac{1}{\sqrt{2}}\left(\,|B(t_1),\vec{p}>|\overline{B}(t_2),-\vec{p}> - |\overline{B}(t_1),\vec{p}>|B(t_2),-\vec{p}>\,\right)\,.$$

In this equation $\vec{p}$ is the momentum of a meson in the center-of-mass frame, and $t_{1,2}$ are approximately equal to the proper times of the B mesons, produced almost at rest in this frame. Writing explicitly the time dependent evolutions $B(t)$ and $\overline{B}(t)$ (Eq. 1.58 and 1.59), we obtain:

$$\begin{aligned}
|\psi(t_1,t_2)> \;&\propto\; \cos\left[\frac{\Delta M}{2}(t_1-t_2)\right]\times \\
&\times\; \left[\,|B,\vec{p}>|\overline{B},-\vec{p}> - |\overline{B},\vec{p}>|B,-\vec{p}>\,\right] - \\
&-\; i\,sin\left[\frac{\Delta\Gamma}{2}(t_1-t_2)\right]\times \\
&\times\; \left[\frac{p}{q}|B,\vec{p}>|B,-\vec{p}> - \frac{q}{p}|\overline{B},\vec{p}>|\overline{B},-\vec{p}>\right].
\end{aligned} \tag{1.73}$$

Until one of the two mesons decays, $t_1 = t_2$ and the sin term vanishes: at each time there is always a $B\overline{B}$ state and the other possibilities (a BB or a $\overline{B}\overline{B}$ state) are exluded (*coherent evolution of the $B\overline{B}$ state*).

As an useful example, let us suppose that at time $t_2 = t_{tag}$ one B decays into a final state f_{tag} which determines univocally its flavor as a $\overline{B}^0$. Thus, at the same time t_{tag} the flavor of the other B is a B^0 and it will continue to evolve according to the evolution function $B(t)$, with $t = t_1 - t_{tag}$, until it decays. Let us suppose that this other B decays into a CP-eigenstate f_{CP} at time $t_1 = t_{CP}$. We can use Eq. 1.73 to write the decay amplitude of the overall process:

$$< f_{CP}(t_{CP})\ f_{tag}(t_{tag})_{\overline{B}^0}\,|H|\,\psi(t_1,t_2) >\propto A_{CP}\bar{A}_{tag}\times \\ \times\left(\cos\frac{\Delta M t}{2}(t_{CP}-t_{tag}) +\ i\,\frac{q}{p}\frac{\bar{A}_{CP}}{A_{CP}}\ \sin\frac{\Delta M t}{2}(t_{CP}-t_{tag})\right), \quad (1.74)$$

where A_{CP} and $\bar{A}_{tag}$ are the matrix elements $< f_{CP}|H|B >$ and $< f_{tag}|H|\overline{B} >$ respectively. We remark that Eq. 1.74 is the same of Eq. 1.61, but with $t = t_{CP} - t_{tag}$ and the flavor tagging decay included.

In conclusion, if the asymmetry observable $\mathcal{A}$ is studied at a B-factory, realized with an e^+e^- collider working at the $\Upsilon(4S)$ resonance (see Section 2.1), we can still use Eq. 1.67 but the time t has to be interpreted as the relative time between the tagging and the CP decays ($t = t_{CP} - t_{tag}$), which can be either positive or negative according to the succession of the decays. For this reason the measurement must be performed as a function of time, otherwise the asymmetry for $t > 0$ would cancel the contribution for $t < 0$ and no asymmetry will be observed.

1.3.1 The golden mode

The condition of no direct CP-violation is satisfied by the class of modes with a $b \to c\bar{c}s$ transitions and a charmonium resonance in the final state, like the *golden mode* $B^0 \to J/\psi\, K^0_S$ [18]. The calculation of the parameter λ for this decay has to take into account that the K^0_S is a mixing of K^0 and $\overline{K}^0$ states:

$$|K^0_S >= p_K|K > +q_K|\overline{K} >\,, \quad (1.75)$$

and the amplitude of the decay will be:

$$A_{J/\psi\, K^0_S} =< J/\psi\, K^0_S|H|B >= p^*_K < J/\psi\, K|H|B > +q^*_K < J/\psi\, \overline{K}|H|B > \ .$$

Since the only possible processes are $B^0 \to J/\psi\, K^0$ and $\overline{B}^0 \to J/\psi\, \overline{K}^0$, we have:

$$A_{J/\psi\, K^0_S} = p^*_K < J/\psi\, K|H|B > \equiv p^*_K A_0 \,. \tag{1.76}$$

Similarly, the amplitude of the CP-conjugate decay $\overline{B}^0 \to J/\psi\, K^0_S$ will be given by:

$$\bar{A}_{J/\psi\, K^0_S} = q^*_K < J/\psi\, \overline{K}|H|\overline{B} > \equiv q^*_K \bar{A}_0 \,. \tag{1.77}$$

From the definition of λ we have:

$$\lambda_{J/\psi\, K^0_S} = \left(\frac{q}{p}\right)_B \cdot \frac{\bar{A}_{J/\psi\, K^0_S}}{A_{J/\psi\, K^0_S}} = \left(\frac{q}{p}\right)_B \cdot \left(\frac{q^*}{p^*}\right)_K \frac{\bar{A}_0}{A_0} \,, \tag{1.78}$$

that in the SM leads to:

$$\lambda_{J/\psi\, K^0_S} = \eta_{CP}\, e^{-2i\beta} \,, \tag{1.79}$$

where the CP-eigenvalue of the final state $J/\psi\, K^0_S$ is $\eta_{CP}(J/\psi\, K^0_S) = -1$.

Thus the measurement of the time-dependent CP-asymmetry for the $B^0 \to J/\psi\, K^0_S$ channel (and for a class of similar decays) provides a clean determination of $Im\lambda = \sin 2\beta$. For other classes of decays the parameter λ can be related to the angles α or γ of the Unitarity Triangle [18] but the condition of a unique weak phase in the decay amplitude is not well satisfied, and therefore the extraction of these angles from the observed asymmetry is not simple and is affected by larger theoretical uncertainties.

From the analysis of a data sample of 32 million $B\overline{B}$ pairs collected in 1999-2001, the *BABAR* collaboration has determined for $\sin 2\beta$ a value of [19]:

$$\sin 2\beta = 0.59 \pm 0.14(stat.) \pm 0.03(syst.) \,, \tag{1.80}$$

that establishes CP-violation in the B^0 meson system at the 4.1σ level. No evidence of direct CP-violation for the examined modes has been found. The measured value of $\sin 2\beta$ can be compared with the existing constraints on the Unitarity Triangle (see Section 1.1.3) and it is found to be consistent with the SM predictions.

Chapter 2

The *BABAR* experiment

The *BABAR* experiment is currently collecting data at the Stanford Linear Accelerator Center (SLAC). The small branching fractions of the relevant modes to be studied (10^{-4} or less) and the *CP*-asymmetry measurement pose stringent requirements both on the accelerator machine for the production of the B mesons and on the particles detector, which are described in the present chapter.

2.1 The PEP-II B Factory

The PEP-II B Factory [20] is a high luminosity ($\mathcal{L} = 3 \times 10^{33}\, cm^{-2} s^{-1}$) e^+e^- collider operating at the $\Upsilon(4S)$ resonance, which decays almost exclusively in a $B^0\overline{B}^0$ or a B^+B^- pair with equal probabilities. This results in a clean environment, characterized by a high signal-to-noise ratio ($\sigma_{b\bar{b}}/\sigma_{TOT} \approx 0.28$) and low track multiplicity per event (≈ 11). In addition, events reconstruction and background rejection benefit by the kinematic constraint on the momentum and energy of each B in the center-of-mass frame.

At PEP-II the energy of the electron beam ($E_{e^-} = 9.0\,\text{GeV}$) is different from the energy of the positron beam ($E_{e^-} = 3.1\,\text{GeV}$), with a consequent boost of the $\Upsilon(4S)$ in the laboratory frame. The asymmetry of the machine is motivated by the need of separating the decay vertices of the two B mesons, a feature which is crucial for the *CP*-asymmetry determination. Indeed, the relative time $t_{CP} - t_{tag}$ between the decays of the two B mesons (see Section 1.3) can be derived in principle from their relative decay length $(\Delta z)_{CM}$ measured in the center-of-mass frame. Unfortunately, on the average $(\Delta z)_{CM} \approx 30\,\mu m$,

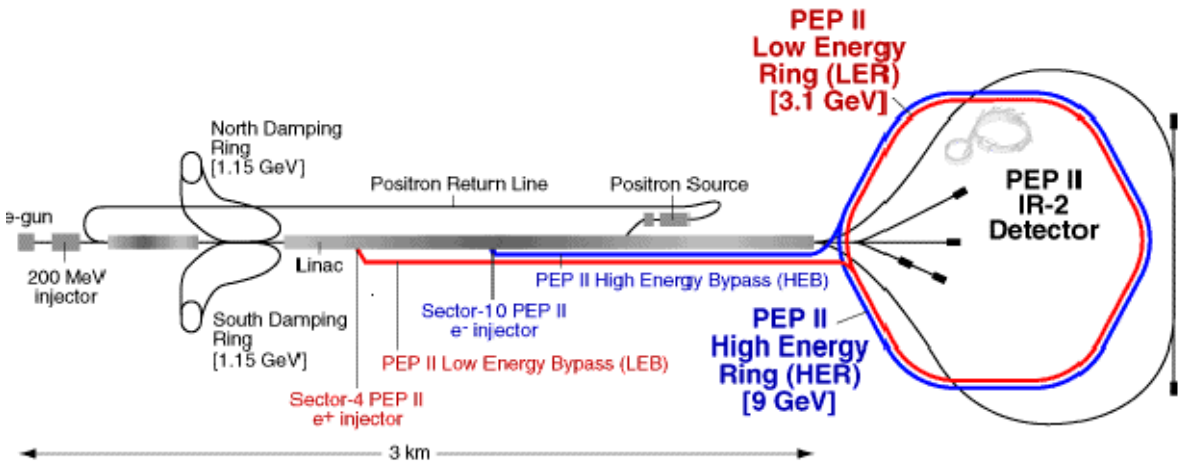

Figure 2.1: A drawing of the PEP-II B Factory, along with the SLAC Linac.

which is below the limit set by the spatial resolution of present vertex detectors technology. On the contrary, if the machine is asymmetric the relative decay time in the laboratory frame receives a relativistic enhancement:

$$(\Delta t)_{lab} = \gamma(t_{CP} - t_{tag}) \,, \tag{2.1}$$

that increases the separation of the decay vertices. The boost of PEP-II ($\beta\gamma = 0.56$) provides a mean vertex separation $(\Delta z)_{lab} \approx 260\,\mu m$, that is measurable with state-of-the-art vertex detectors.

The electrons and positrons beams are produced at the SLAC Linac, a linear accelerator $3\,km$-long, and are injected into separate storage rings: the e^- in the High Energy Ring (HER) and the e^+ in the Low Energy Ring (LER), which are installed on top of each other in a tunnel $2.2\,km$-long (see Fig. 2.1). The e^- and e^+ bunches collide head on in a single Interaction Point (IP) and are separated in the horizontal plane, after the collision, by permanent dipole magnets (B1), located at $\pm 21\,cm$ on either side of the IP (see Fig. 2.2). Permanent quadrupole magnets (Q1), installed at $\pm 90\,cm$ from the IP, provide strong focalization of the beams.

The interaction region is enclosed by a beam pipe of $27.9\,mm$ outer radius. It is composed of two layers of beryllium, with a cooling water channel between them. The inner surface of the pipe is coated with a $4\,\mu m$ layer of gold for attenuation of the strong synchrotron radiation due to the B1 deflecting dipoles. In addition, the beam pipe is wrapped with $150\,\mu m$ of tantalum

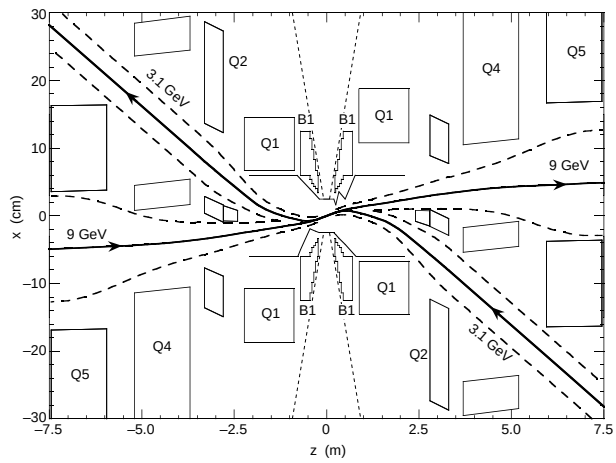

Figure 2.2: A schematic view of the interaction region in the horizontal plane of the accelerator. The deflection of the beams due to the B1 dipoles and the focalization due to the Q1 quadrupoles are also shown.

foil on either side of the IP, beyond $z = +10.1\,cm$ and $z = -7.9\,cm$. The beam pipe, the permanent magnets and the vertex detector (the innermost component of the *BABAR* detector) are enclosed in a $4.5\,m$-long carbon fiber support tube (inner diameter $= 21.7\,cm$) surrounding the IP.

2.1.1 Performances

The luminosity $\mathcal{L}$ of the machine depends on the careful tuning of several parameters. This dependence can be expressed with the following equation:

$$\mathcal{L} = \frac{n f N_1 N_2}{A}\,, \tag{2.2}$$

where n is the number of bunches in a ring, f is the frequency of the bunch crossing, $N_{1,2}$ are the number of particles in each bunch, and A is their overlap section.

Table 2.1 reports the design values of these parameters and the reached performances. The machine has surpassed the design performances, reaching a peak luminosity of $\mathcal{L} = 3 \times 10^{33}\,cm^{-2}s^{-1}$ with a significantly lower number of bunches. Figure 2.3 shows the integrated luminosity provided by PEP-II from May 1999 to September 2001, along with the integrated luminosity recorded by the *BABAR* detector.

Table 2.1: PEP-II beam parameters. Design values and typical performances are reported.

Parameters	Units	Design	Typical
Energy HER/LER	GeV	9.0/3.1	9.0/3.1
Current HER/LER	A	0.75/2.15	0.7/1.3
# of bunches		1658	553-829
Bunch spacing	ns	4.2	6.3-10.5
Beam spot x-size	μm	220	190
Beam spot y-size	μm	6.7	6.0
Peak luminosity	$10^{33}\,cm^{-2}s^{-1}$	3	2.5

2.1.2 Machine background

Machine-generated background causes high single counting rates, data acquisition dead times, high currents, and radiation damages both of the detector components and of the electronics. This results in lower data quality and may limit the lifetime of the apparatus. For this reason, the background generated by PEP-II has been studied in detail and the interaction region has been carefully designed. Furthermore, background rates are continously monitored during data acquisition to prevent critical operating conditions of the detector.

The primary sources of machine-generated background are: synchrotron radiation in the proximity of the interaction region, interactions between beam particles and residual gas in either ring, and electromagnetic showers generated by beam-beam collisions.

Synchrotron radiation is a strong source of background (many KW of power), and it is due to the beam deflections in the interaction region. The impact of this background on the detector is limited by channelling the radiation out of the *BABAR* acceptance with a proper design of the interaction region and the beam orbits, and placing absorbing masks before the detector components.

Interactions between beam particles and residual gas molecules in the rings are of two types: beam-gas bremsstrahlung and Coulomb scattering. In both cases, the interaction causes the beam particles to escape from their orbit. The B1 dipoles bend these particles in two opposite directions (depending on their charge) in the horizontal plane of the machine. As a consequence,

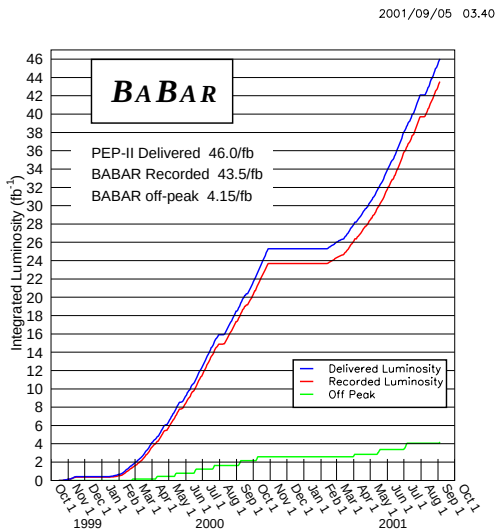

Figure 2.3: Integrated luminosity provided by the PEP-II *B* Factory in 1999-2001. The total integrated luminosity, and the off-peak only, recorded by the *BABAR* detector is also shown.

two occupancy peaks are clearly revealed in the *BABAR* detector system. This background represents the primary source of radiation damage for the inner vertex detector and the principal background for the other detector components.

Radiative Bhabha scattering can produce energy degradated e^+ or e^- hitting the beam pipe within a few meters of the IP with the consequent generation of electromagnetic showers that may reach the *BABAR* detector. This background is proportional to the luminosity of the machine. In the actual operating conditions this source of background is under control, but it is expected to increase its relevance if the machine will operate at higher values of the luminosity.

2.2 The *BABAR* detector

The *CP*-asymmetry measurement and the properties of the decay channels to be studied at *BABAR* determine the general features of the detector surrounding the PEP-II interaction region [21, 22].

For a CP-asymmetry measurement full reconstruction of the decay of one B is needed, while the flavor of the other B has to be determined from its charged decay products. Typical events are characterized by small branching fractions ($\leq 10^{-4}$), two to six charged particles and one or more π^0 in the final state. In addition, the asymmetry of the machine causes the decay products to be emitted at small polar angles relative to the e^- high energy beam direction (which is assumed as the forward direction). An efficient events reconstruction requires therefore a detector with large and uniform acceptance down to these angles.

Figure 2.4 shows a longitudinal view of the detector, while an end view is shown in Fig. 2.5. A conventional right-handed coordinate system is defined: the z-axis coincides with the principal axis of the DCH, while the y-axis points upward. The polar angle coverage extends down to $0.35\,rad$ in the forward direction and to $0.4\,rad$ in the backward direction. These limits are determined by the B1 and Q1 magnets of PEP-II. In order to improve the coverage of the forward region, the whole detector is offset relative to the IP by $370\,mm$ in the forward direction. The distance of the beam pipe from the floor ($3.5\,m$) poses a constraint on the transversal dimension of the detector, that has to be of compact design.

Starting from the innermost components, the detector consists of a silicon vertex tracker (SVT) and a drift chamber (DCH) for charged particles track reconstruction, a detector of internally reflected Cherenkov light (DIRC) for charged hadrons identification, a CsI calorimeter (EMC) for identification of electromagnetic showers from electrons and photons; these components are embedded in a 1.5T magnetic field generated by a superconducting solenoid. The steel of the flux return of the magnet (IFR) is the outermost part of the detector and is instrumented with resistive plate chambers for muons and neutral hadrons identification.

2.2.1 The tracking system

The SVT and the DCH constitute the tracking system of the detector, for the efficient detection of charged particles and the determination of the track parameters with high precision. These high precision measurements allow for the reconstruction of exclusive B and D mesons decays with high resolution and thus minimal background. In particular, angles and positions measured by the SVT are used for determining the decay vertices of the B mesons, and

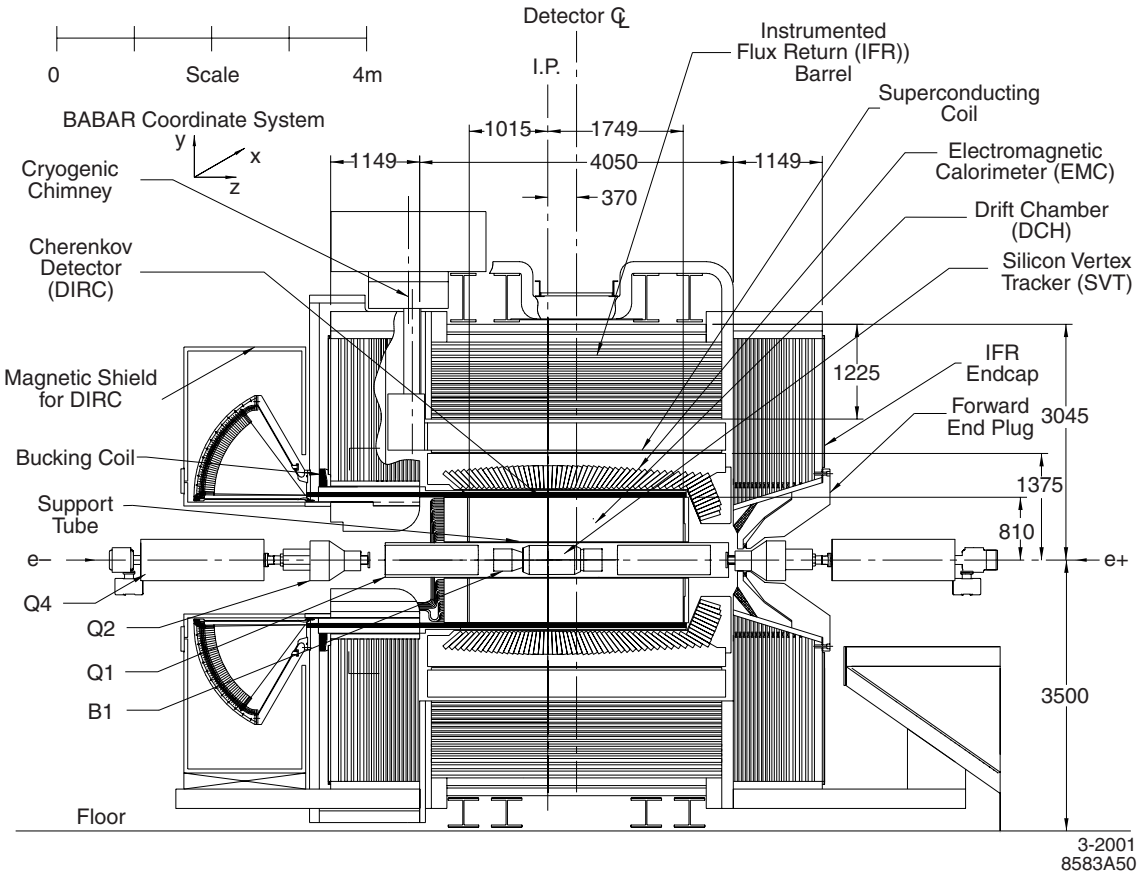

Figure 2.4: Longitudinal section of the *BABAR* detector.

the curvature of the track in the DCH measures the momentum of the charged particle. Tracks reconstructed in the SVT and DCH are also extrapolated to the other components (DIRC, EMC, and IFR). Since the average momentum of charged particles from B decays is less than 1 GeV/c, the precision of the measured track parameters is mostly affected by multiple Coulomb scattering in the detector material. Thus, the design of the components required a special attention in limiting the overall amount of material in the active region.

The silicon vertex tracker

The main purpose of the SVT is the measurement of the angles and positions of charged particles immediately outside the beam pipe. The SVT is located

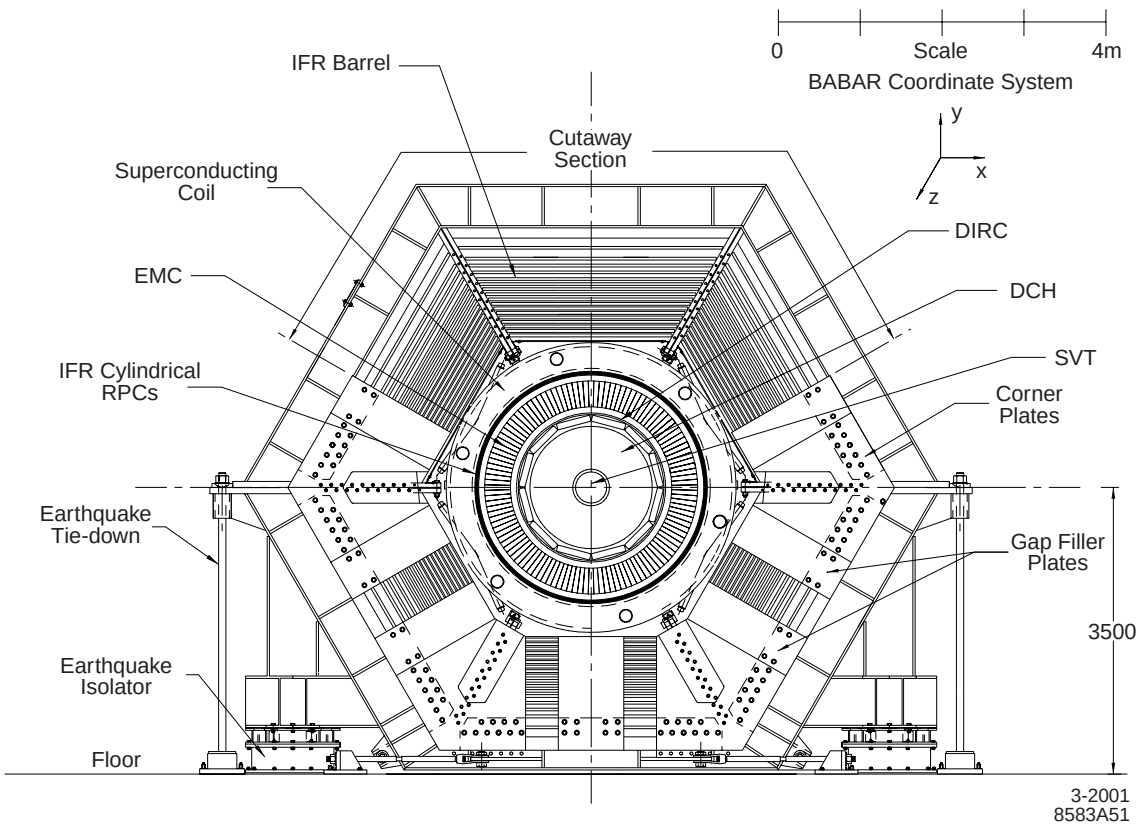

Figure 2.5: End view of the *BABAR* detector.

inside the support tube along with the machine components, which limit the angular acceptance of the detector to 350 $mrad$ in the forward direction and 520 $mrad$ in the backward direction.

Figure 2.6 shows a longitudinal view of the detector: it is composed of five concentric layers of 300 μm double-sided silicon strip detectors, organized in 6, 6, 6, 16, and 18 modules (see Fig. 2.7). The modules of the inner three layers are straight, while the modules of layers 4 and 5 are *arch*-shaped in order to minimize both the amount of silicon required to cover the solid angle and the material traversed by the particle at small or large polar angles. The inner modules are tilted in ϕ by 5°, allowing an overlap region between adjacent modules. The outer modules cannot be tilted, because of the arch geometry, but are divided into two sub-layers (layers 4a, 4b, 5a, 5b) placed at slightly different radii. The radius of the innermost layer (layer 1) is 32 mm while the radius of the outermost layer (layer 5b) is 144 mm. The strips on

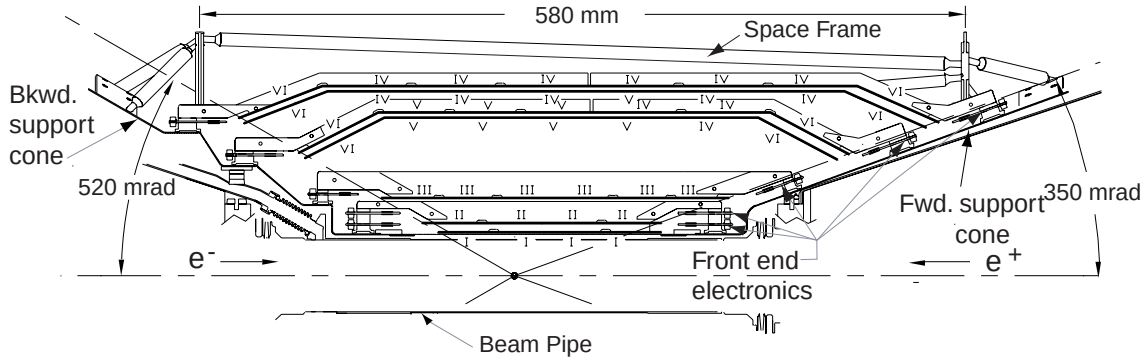

Figure 2.6: Longitudinal view of the SVT.

the opposite sides of each silicon sensor measure different coordinates: we have z-strips, oriented perpendicularly to the beam axis, and longitudinal ϕ-strips. The total active silicon area is $0.96\,m^2$.

The angles and positions measured in the innermost three layers are used for B vertex determination. They have been mounted very close to the beam pipe in order to minimize the impact of multiple scattering in the vertex resolution. The angles and positions measured in the last two layers are used, together with the DCH measurements, for track reconstruction. Charged particles with transverse momentum less than $120\,\mathrm{MeV}/c$ are not reliably reconstructed in the DCH. In order to improve tracking efficiency for these particles (such as slow pions from D^* decays), the SVT is able to provide standalone tracking.

For perpendicular tracks a position resolution of about $15\,\mu m$ in the three inner layers and $40\,\mu m$ in the outer layers is achieved. Furthermore, the mean resolution on the separation between the two B vertices is less than $100\,\mu m$.

In addition to the position measurement, the double-sided silicon devices provide measurements of the $\mathrm{d}E/\mathrm{d}x$ ionization loss of the track, useful for particle identification. Indeed, the time interval during which the signal from a strip is above a certain threshold ("time over threshold") is logarithmically related to the charge induced on the sensor.

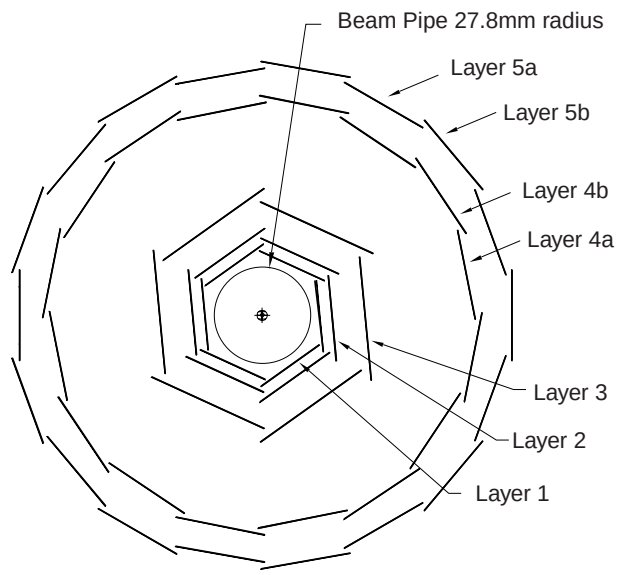

Figure 2.7: Transverse view of the SVT.

The drift chamber

The main purpose of the DCH is the efficient detection of charged particles and the measurement of their momenta and angles with high precision. Furthermore, in order to reconstruct decay vertices outside the SVT volume (for instance the $K_S^0 \to \pi^+\pi^-$ vertex), the drift chamber is required to measure both the transverse and the longitudinal position of the tracks.

The DCH is a $280\,cm$-long cylinder with an inner radius of $23.6\,cm$ and an outer radius of $80.9\,cm$ (see Fig. 2.8). The forward and rear aluminium endplates are $12\,mm$-thick and $24\,mm$-thick respectively, and all the electronics is mounted on the rear endplate. This choice prevents degradation of performances for the successive *BABAR* detector components in the most critical (because of the boost) forward region.

The DCH consists of 7104 hexagonal drift cells arranged in 40 concentric layers. An exagonal cell has dimensions $\sim 12\,mm$ along the radial direction and $\sim 19.0\,mm$ along the azimuthal direction. It consists of one sense wire surrounded by six field-shaping wires such that an approximate circular symmetry of the electric field is reached over a large portion of the cell. The field wires are at ground potential while a positive high voltage is applied to the sense wires. Wires parallel to the z-axis (type A wires) provide position

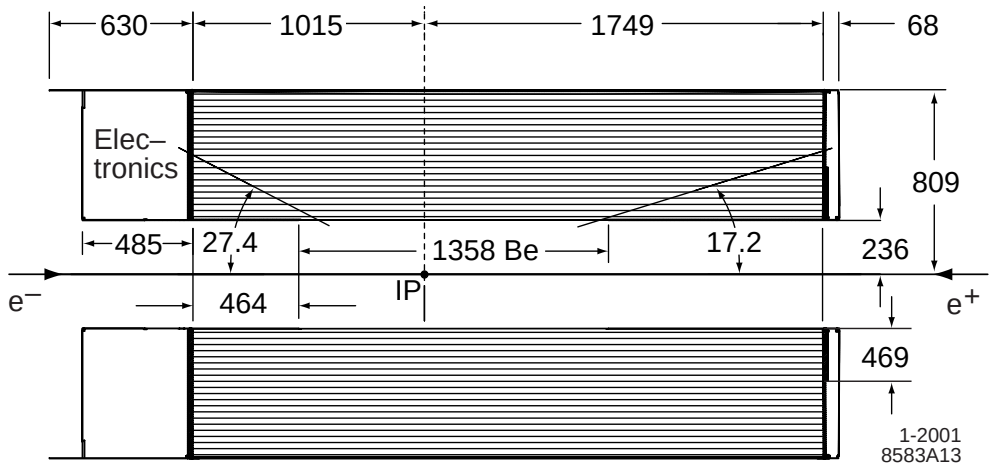

Figure 2.8: Longitudinal section of the DCH.

measurements in the x-y plane, while longitudinal position information is obtained with wires placed at small angles with respect to the z-axis (type U or V wires). In order to minimize multiple scattering inside the active volume, low-mass aluminum field wires and a helium-based gas mixture (with a radiation length five times larger than commonly used argon-based gases) are employed. At a typical operating voltage of 1960 V and with an 80:20 helium:isobutane gas mixture, the avalanche gain is approximately 5×10^4.

The layers are grouped by four into superlayers, each characterized by a definite orientation of the wires. There is a total of ten superlayers, which alternate between axial (A) and stereo (U,V) pairs, according to the sequence AUVAUVAUVA, as shown in Fig. 2.9.

The drift time in a cell, measured by detecting the leading edge of the signal on the sense wire, is digitized and a time-to-distance relation, calibrated on data (e^+e^- and $\mu^+\mu^-$ events), connects this time with the drift distance needed for the position measurement. The position resolution depends on the drift distance; typical values in the range $0.1 - 0.15\,mm$ are achieved.

For low momentum particles the DCH provides also particle identification by measurements of the $\mathrm{d}E/\mathrm{d}x$ ionization loss in the cells. This requires the integration of the signals from the cells traversed by the particle in order to obtain the total charge collected by the wires.

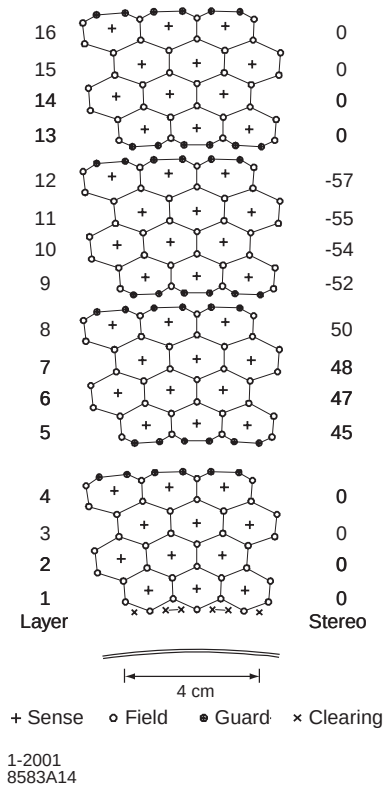

Figure 2.9: Layout of the four innermost superlayers. Imaginary lines between the field wires visualize the cells boundaries. The numbers on the right side are the stereo angles of the sense wires in each layer. The 1 mm-thick beryllium inner wall before the first layer is also shown.

Performances of the tracking system

The performances of charged particle reconstruction at *BABAR* have been extensively studied, both in data and with Monte Carlo simulations.

Track reconstruction can be performed indipendently in the SVT and the DCH. This gives the possibility to determine the efficiency of the track reconstruction in the DCH as:

$$\varepsilon(\mathrm{DCH}) = \frac{N_{trk}(\mathrm{DCH})}{N_{trk}(\mathrm{SVT})}, \tag{2.3}$$

where $N_{trk}(\mathrm{DCH})$ is the number of reconstructed tracks in the DCH and $N_{trk}(\mathrm{SVT})$ is the number of tracks detected in the SVT and falling within the DCH acceptance. At the design voltage of 1960 V, the average efficiency

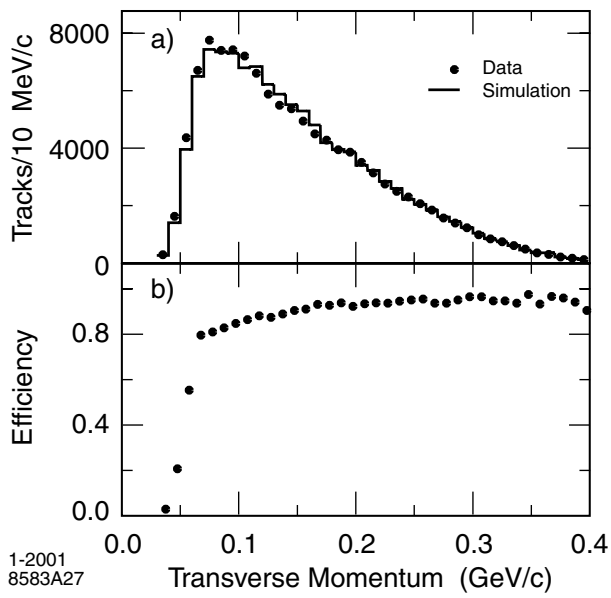

Figure 2.10: (a): Transverse momentum spectrum of pions from $D^{*+} \to D^0\pi^+$ decays as obtained in data and from Monte Carlo simulations. (b): Efficiency for slow pion detection as obtained from Monte Carlo simulations.

per track, with transverse momentum above $200\,\mathrm{MeV}/c$ and polar angle $\theta > 500\,mrad$, is $(98 \pm 1)\%$.

The SVT standalone tracking is extremely important for the detection of soft pions from $D^{*+} \to D^0\pi^+$ decays. Figure 2.10-(a) shows the transverse momentum spectrum for these pions, as measured in data and from Monte Carlo simulations. The detection efficiency is shown in Fig. 2.10-(b) where it is evident that charged particle detection extends down to transverse momenta of $\sim$50 MeV/c.

The parameters of a track are measured at the point of closest approach to the z-axis. In particular, the parameter d_0 and z_0 are defined as the distances of this point from the origin of the coordinate system in the x-y plane and along the z-axis, respectively. The measured resolution in d_0 and z_0, as a function of the transverse momentum p_t, is shown in Fig. 2.11. At $p_t = 3\,\mathrm{GeV}/c$ the d_0 and z_0 resolutions are about $25\,\mu m$ and $40\,\mu m$ respectively.

Figure 2.12 shows the resolution in the transverse momentum as derived from cosmic rays muons. The data are well represented by a linear function:

$$\sigma_{p_t}/p_t = (0.13 \pm 0.01)\% \cdot p_t + (0.45 \pm 0.03)\%, \tag{2.4}$$

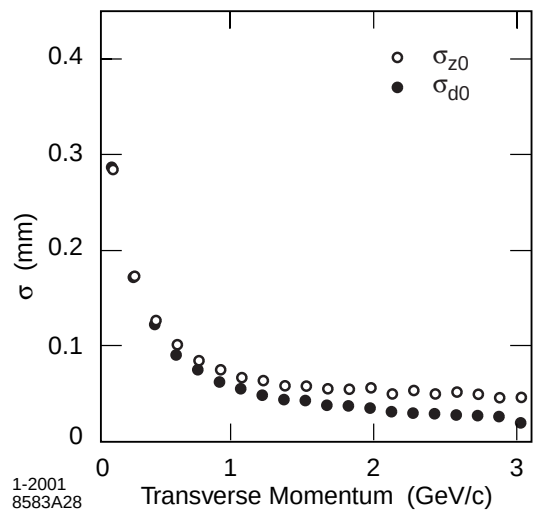

Figure 2.11: Resolution in the parameters d_0 and z_0, as a function of the transverse momentum p_t, determined from tracks in multi-hadron events.

where the transverse momentum p_t is measured in GeV/c.

2.2.2 The DIRC

Particle identification of charged hadrons is extremely important for flavor tagging of the B via the cascade decay $b \to c \to s$. The momenta of the kaons used for tagging extend up to about 2 GeV/c. Furthermore, charged hadrons discrimination is very useful for the separation of rare decay modes, like $B^0 \to \pi^+\pi^-$ and $B^0 \to K^+\pi^-$ (where kaons and pions have momenta between 1.7 and 4.2 GeV/c). While particle identification at momenta below 700 MeV/c relies primarily on the dE/dx measurements in the DCH and SVT, at higher momenta this task is performed by a Cherenkov detector, the DIRC.

The phenomenon of Cherenkov light emission is widely used in particle detectors technology. A charged particle traversing a medium with a velocity β greater than the speed of light in that medium (that is $\beta > 1/n$, where n is the index of refraction of the medium) emits directional electromagnetic radiation (called Cherenkov light). The angle of emission θ_C of the photons with respect to the track direction is called Cherenkov angle and is determined by the velocity of the particle: $\theta_C = 1/n\beta$. Thus, the measurement of θ_C determines β and, given the momentum of the particle (measured in the

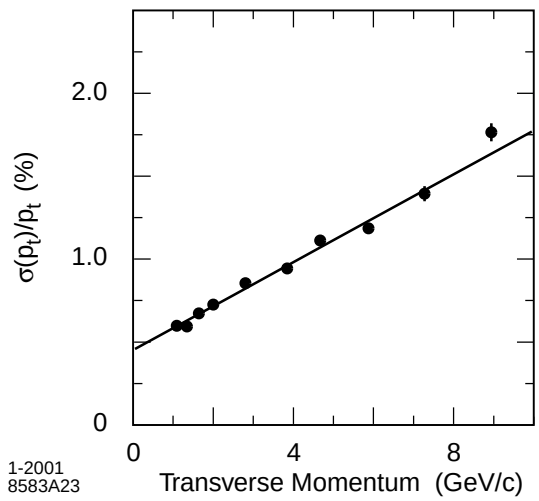

Figure 2.12: Resolution in the transverse momentum p_t, determined from cosmic rays muons.

DCH), the mass of the particle can be obtained.

The DIRC is composed of 144 thin quartz bars of rectangular cross section, disposed longitudinally to form a 12-sided polygonal barrel. Each bar is $17\,mm$-thick, $35\,mm$-wide, and $4.9\,m$-long, and acts both as radiator material (index of refraction $n = 1.473$) and light pipe. Photons are transmitted in the bar via total internal reflections at the flat surface, a mechanism preserving the angular information (see Fig. 2.13).

In order to minimize interference with other detector systems in the most critical forward region, only the backward end is instrumented with photons detectors. However, photons moving forward are not lost because mirrors placed at the forward end of each bar reflect them to the backward end. Here a small piece of quartz with a trapezoidal profile allowes for significant reduction in the area requiring instrumentation because it folds one half of the Cherenkov image into the other half. The photons emerge into a toroidal tank (the *standoff box*) filled with purified water, where the Cherenkov angle is allowed to expand. The choice of water has been dictated by its refractive index, matching quite well with that of the bars, thus minimizing the total internal reflection at the quartz-water interface. The Cherenkov photons are finally detected, in the visible and near-UV range, by an array of photomultiplier tubes (PMT), placed on the surface of the tank (at a distance of about $1.2\,m$ from the bar end).

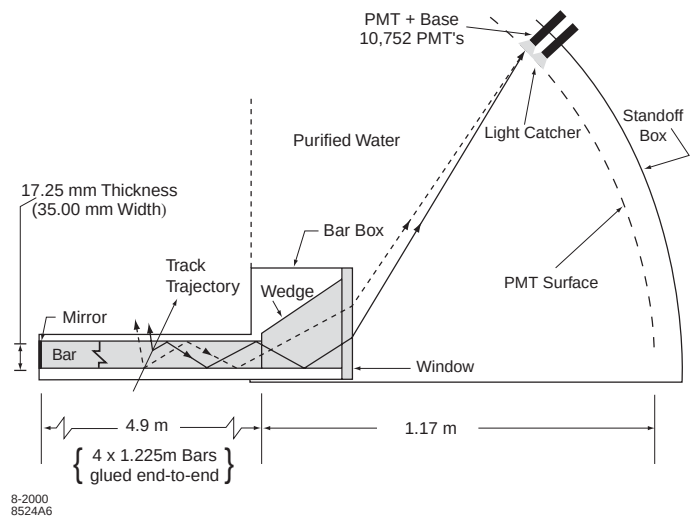

Figure 2.13: Light generation, transmission and detection in the DIRC.

The informations used for the reconstruction of the Cherenkov angle are the position and arrival time of the PMT signal, along with the known spatial position of the quartz bar traversed by the track. The three-dimensional vector pointing from the center of the bar end to the center of the PMT is computed, and then is extrapolated (using Snell's law) into the radiator bar in order to extract, given the direction of the charged particle, the Cherenkov angle. Timing information is used to suppress background hits and to correctly identify the track emitting the photons.

The number of detected photons N_{pe} varies between 20 for tracks at normal incidence and 65 for tracks at small or large polar angles, because of the different pathlengths in the radiator. The Cherenkov angle resolution scales as $1/\sqrt{N_{pe}}$ and has been measured in $\mu^+\mu^-$ events: typical values of about $2.5\,mrad$ are reached. This results in a separation power between pions and kaons at $3\,\mathrm{GeV}/c$ of about 4.2σ.

Selection algorithms for charged kaons have been developed. They use particle identification informations from the SVT, the DCH and the DIRC, and differ for the level of purity of the selection. The efficiency for correctly identifying a charged kaon and the probability to wrongly identify a pion as a kaon are illustrated, as a function of the track momentum, in Fig. 2.14 (for a particular selection algorithm). The average kaon selection efficiency and pion misidentification are $\sim 96\%$ and $\sim 2.1\%$, respectively.

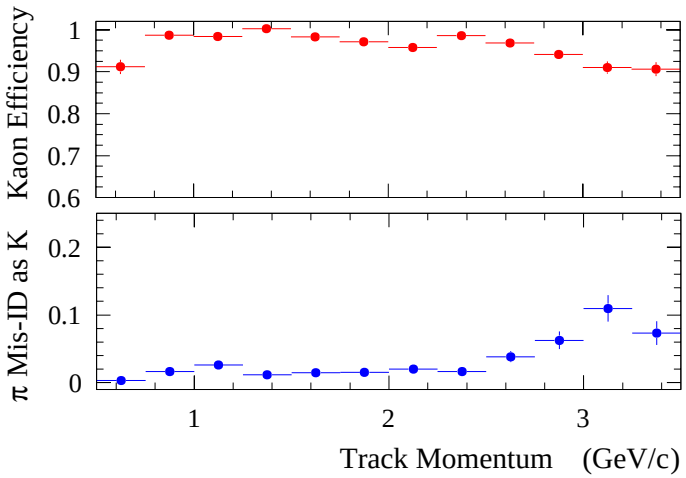

Figure 2.14: Efficiency and misidentification probability for the selection of charged kaons, derived from kaons and pions in $D^0 \to K^-\pi^+$ decays, selected kinematically from inclusive D^* production.

2.2.3 The electromagnetic calorimeter

The purpose of the electromagnetic calorimeter is the detection of electromagnetic showers with very high efficiency, and the measurement of the energy and direction of the primary photon or electron. The energy range to be covered at *BABAR* goes from about 20 MeV (for photons from decays of slow π^0 or η^0) to about 4 GeV (for photons and electrons from QED processes).

An efficient π^0 reconstruction is critical for the measurement of extremely rare decays, such as $B^0 \to \pi^0\pi^0$. An efficient and pure selection of electrons is useful for B flavor tagging via semileptonic decays, for the reconstruction of vector mesons like J/ψ, or for the reconstruction of several exclusive final states of B and D mesons. Furthermore QED processes like $e^+e^- \to e^+e^-(\gamma)$ and $e^+e^- \to \gamma\gamma$, need to be efficiently detected because they are useful for calibration and luminosity determination.

The EMC is constituted by a finely segmented array of thallium-doped cesium iodide (CsI(Tl)) crystals. It extends in polar angle from 15.8° to 141.8° (see Fig. 2.15). The crystals are disposed according to a projective geometry and are arranged in modules. We distinguish two sectors of the EMC: a cylindrical barrel and a conical forward endcap. The barrel has an inner radius of 92 cm and an outer radius of 136 cm, with a longitudinal dimension of about 3 m. It contains 5760 crystals arranged in 48 distinct

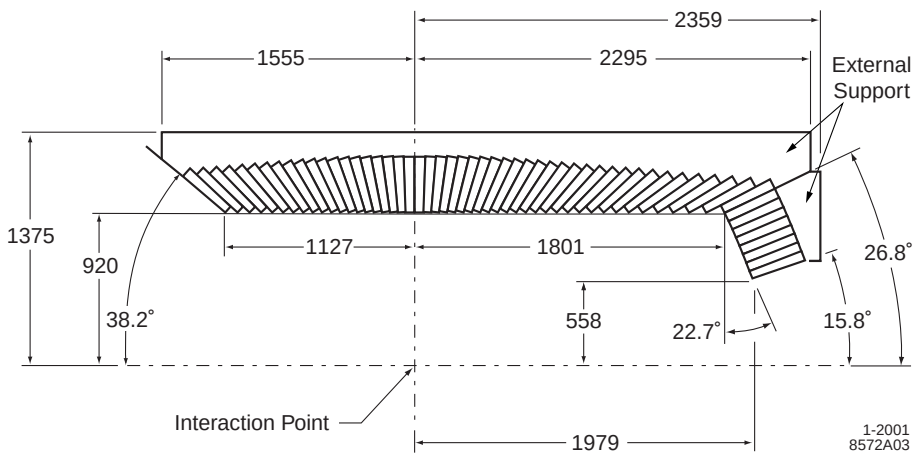

Figure 2.15: Longitudinal section of the EMC (top-half only).

rings. The conical endcap contains 6580 crystals arranged in eight rings.

The CsI(Tl) crystals are characterized by high light yield ($5 \times 10^4 \gamma/\,\mathrm{MeV}$) and small Molière radius ($3.8\,cm$), for excellent energy and angular resolution, and a short radiation length ($1.85\,cm$) for shower containement. They have a tapered trapezoidal cross section: the typical area of the front face is $4.7 \times 4.7\,cm^2$, while the back face area is typically $6.1 \times 6.0\,cm^2$. The length of the crystals has been chosen to limit possible shower leakages from higher energy particles: it goes from $29.6\,cm$ (for crystals in the backward region) to $32.4\,cm$ (for crystals in the forward direction).

The EMC crystals act not only as a total-absorption scintillating medium, but also as a light guide. The light is collected by silicon photodiodes that are mounted on the rear surface. A periodical calibration procedure is needed to extract the energy of the incident photon or electron. Furthermore, the energy deposited over several adjacent crystals needs to be corrected for energy losses (due to shower leakages, absorption in the material between and in front of the crystals, and photomultiplier signals not associated with the shower).

A typical electromagnetic shower spreads over many adjacent crystals, forming a cluster of energy deposits. Clusters are identified and associated to a charged or a neutral particle by pattern recognition algorithms. Two kinds of clusters are reconstructed: single clusters with one energy maximum, and merged clusters characterized by several local energy maxima (*bumps*).

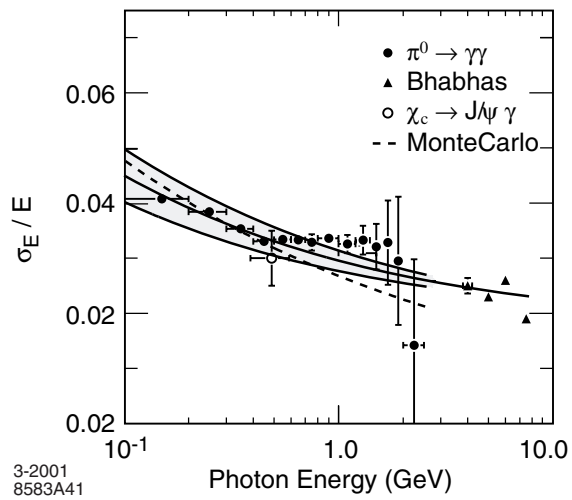

Figure 2.16: The energy resolution for the EMC as a function of the shower energy. It has been measured with photons from several processes. The fit leading to Eq. 2.5 is also shown; the shaded region represents the rms error of the fit. The dashed curve represents the prediction obtained from Monte Carlo simulations.

Figure 2.16 shows the energy resolution as a function of the shower energy. It is described empirically as a quadratic sum of two terms:

$$\frac{\sigma_E}{E} = \frac{(2.32 \pm 0.30)\%}{\sqrt[4]{E(\,\mathrm{GeV})}} \oplus (1.85 \pm 0.12)\% \,. \tag{2.5}$$

Figure 2.17 shows the angular resolution as a function of the shower energy. It can be empirically parameterized as a sum of two terms:

$$\sigma_\theta = \sigma_\phi = \left[\frac{(3.87 \pm 0.07)}{\sqrt{E(\,\mathrm{GeV})}} + (0.00 \pm 0.04)\right] \; mrad \,. \tag{2.6}$$

The EMC is the primary detector for electron identification through quantities like the ratio of the shower energy to the track momentum, or variables related to the shape of the cluster. Electrons identification algorithms have been developed, which use these variables along with the $\mathrm{d}E/\mathrm{d}x$ energy loss in the DCH and the DIRC Cherenkov angle. The efficiency for correctly identifying an electron, and the pion misidentification probability for a particular selection algorithm are shown, as a function of the momentum and polar angle of the particle, in Fig. 2.18. The efficiency in the momentum range $0.5 < p < 2\,\mathrm{GeV}/c$ is $\sim 88\%$, while the average misidentification probability is $\sim 0.15\%$.

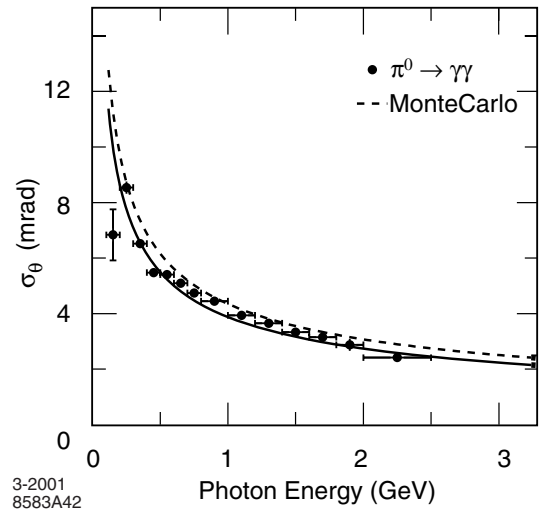

Figure 2.17: The angular resolution of the EMC as a function of the shower energy. It has been derived with photons from π^0 decays. A comparison with the resolution extracted from Monte Carlo events is also shown. The solid curve is the fit leading to Eq. 2.6.

2.2.4 The instrumented flux return

The instrumented flux return (IFR) identifies muons with high efficiency and good purity, and detects neutral hadrons (primarily K_L^0) over a wide range of momenta and angles. Muons identification with good efficiency and high background rejection down to momenta below 1 GeV/c is important for B flavor tagging via semi-leptonic decays, for the reconstruction of vector mesons like the J/ψ, and the study of many exclusive decays of B and D mesons. K_L^0 detection is used for the study of exclusive B decays, like the CP-mode $B \to J/\psi\, K_L^0$ (useful for sin2β determination as the golden mode $B \to J/\psi\, K_S^0$).

The IFR consists of three sectors (see Fig. 2.19): the Barrel concentric to the z-axis (inner radius = 182 cm, outer radius = 304 cm), and the two end doors of the flux return (Forward and Backward End Caps), which extend the polar angle coverage down to 300 $mrad$ in the forward direction and 400 $mrad$ in the backward direction. The steel of the flux return acts as muon filter and hadron absorber. It is segmented into 18 plates of variable thickness (from the 2 cm of the inner nine plates to the 10 cm of the outermost plate) for a total of 65 cm in the Barrel and 60 cm in each End Cap. The gaps between the plates ($\sim$ 3.2 cm) are instrumented with single gap resistive plate chambers

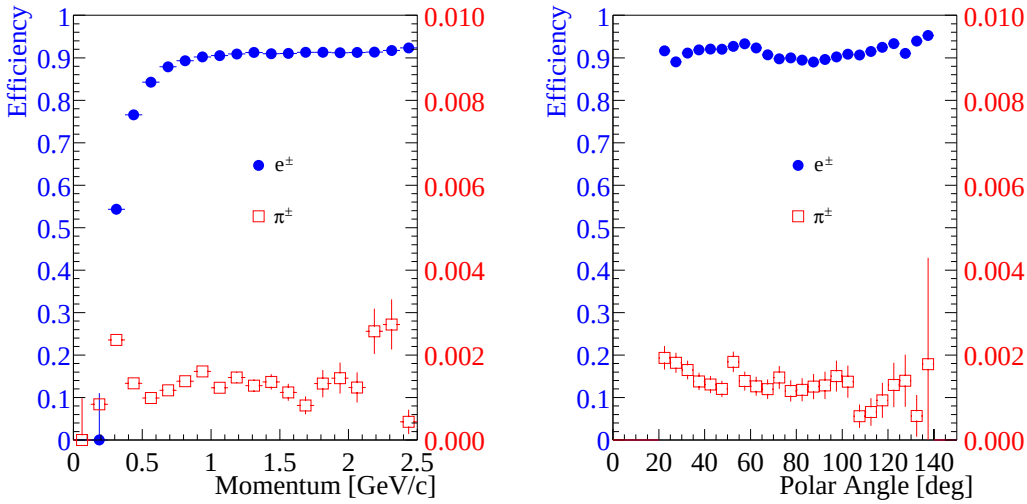

Figure 2.18: The electron efficiency and pion misidentification probability as a function of: (left plot) momentum of the particle in the laboratory frame; (right plot) polar angle of the particle in the laboratory frame. The electron efficiency is measured using electrons from radiative Bhabhas and $e^+e^- \to e^+e^-e^+e^-$ events. The pion misidentification probability is measured using charged pions from K_S^0 decays and three-prongs τ decays.

(RPC) for particles detection. There are 19 RPC layers in the barrel and 18 in each endcap. In addition, two layers of cylindrical RPCs are installed between the EMC and the magnet cryostat to detect neutral hadrons that start to interact in the EMC.

A cross section of an RPC is shown schematically in Fig. 2.20. Two $2\,mm$-thick sheets of bakelite are separated by a $2\,mm$ gap enclosed at the edge by a $7\,mm$-wide frame. The gap width is kept uniform by polycarbonate spacers ($0.8\,cm^2$), that are glued to the bakelite and spaced at distances of about $10\,cm$. The external surfaces of the bakelite sheets are coated with graphite, connected to high voltage (typically 7.6 KV) and ground, and are insulated by a mylar film. The inner surfaces of the bakelite sheets are treated with linseed oil for noise reduction. A non-flammable gas mixture (approximately 56.7% Argon, 38.8% Freon 134a, and 4.5% Isobutane) fills the gap.

An ionizing particle traversing the gap produces a local streamer. Since the bakelite has a resistivity of $\sim 10^{11}$–$10^{12}\,\Omega\,cm$, the streamer induces a signal on aluminium electrodes in the shape of strips, which are mounted

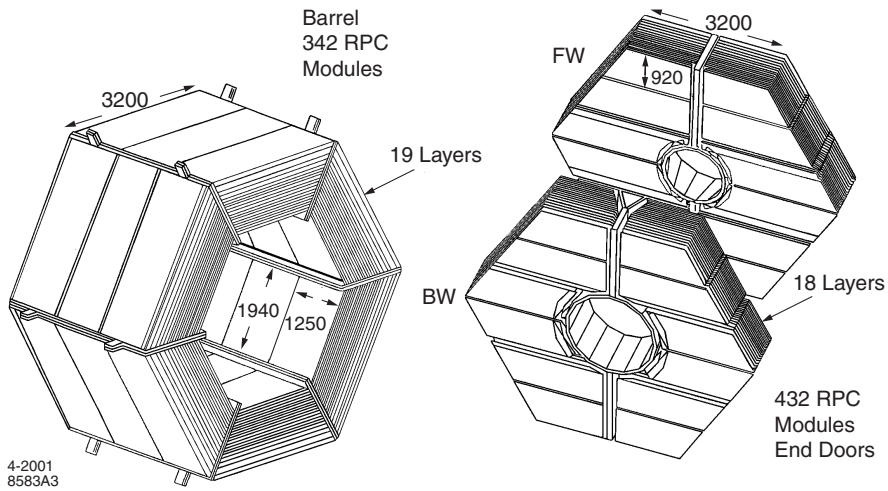

Figure 2.19: The three sectors of the IFR: Barrel, Forward End Cap and Backward End Cap.

externally on the mylar film. There are strips on both sides of the gap, running in perpendicular directions in order to obtain a two-dimensional measurement of the position of the particle. The read out strips are separated from a ground aluminium plane (for electric shielding) by a $4\,mm$-thick foam sheet; this configuration makes the strips equivalent to transmission lines of 33Ω impedance. Thus, the signal induced on a strip moves towards the readout electronics connected at one end.

Each layer in the Barrel extends $375\,cm$ in the z-direction and varies in width from $194\,cm$ to $320\,cm$. Three RPC modules are needed to cover the surface of a layer. Each module has 32 strips running perpendicularly to the beam axis (z-strips) and 96 strips in the orthogonal direction extending over three modules (ϕ-strips). A layer in a half end door is divided into three sections by steel spacers that are needed for mechanical support. The surface of a section is covered by two RPC modules provided with horizontal and vertical readout strips (y and x-strips). The cylindrical RPCs are provided with orthogonal readout strips: the inner layer has helical strips which run parallel to the diagonals of the chambers, while the outer layer has axial and azimuthal strips. On the whole, there are 806 RPC modules of different shapes and sizes in the IFR, covering an area of about $2000\,m^2$.

Hits from different layers in coincidence with an event are grouped into a charged cluster if they can be associated to a track detected in the SVT

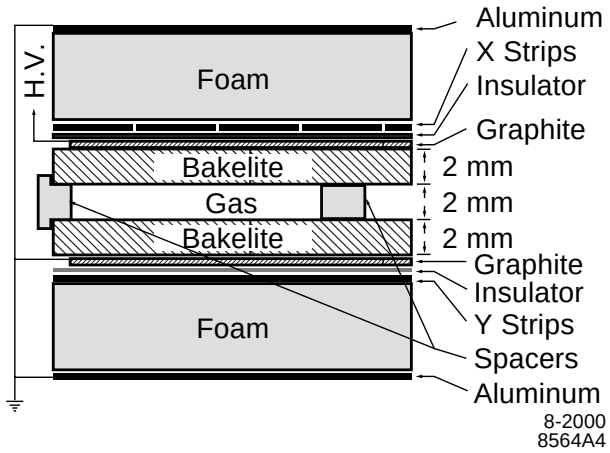

Figure 2.20: Transversal section of a resistive plate chamber.

and the DCH. The track is extrapolated to the IFR taking into account the non-uniform magnetic field, the multiple scattering, and the average energy loss. Then the projected intersections with the RPC planes are computed, and finally all the hits within a predefined distance from the predicted intersection are associated to the track.

The IFR is the primary detector for muons identification through several variables computed for the charged cluster, such as the total number of interaction lengths traversed by the track in the detector; the difference between the above number of interaction lengths and the number of interaction lengths predicted for a muon of the same momentum and angle; the average number and the RMS of the distribution of RPC hit strips per layer; the χ^2 of the geometric match between the projected track and the centroids of clusters in different RPC layers. Muons identification algorithms have been developed, which use the above variables along with the energy released in the EMC. The efficiency for correctly identifying a muon and the pion misidentification probability for a particular selection algorithm are shown, as a function of the momentum and polar angle of the particle, in Fig. 2.21. The muon efficiency in the momentum range $1.5 < p < 3.0\,\mathrm{GeV}/c$ is $\sim 87\%$, with a pion misidentification of $\sim 7\%$. Tighter selection criteria reduce the pion misidentification to $\sim 2.7\%$, with a muon detection efficiency at the 76% level.

K_L^0 and other neutral hadrons that interact in the steel of the IFR are

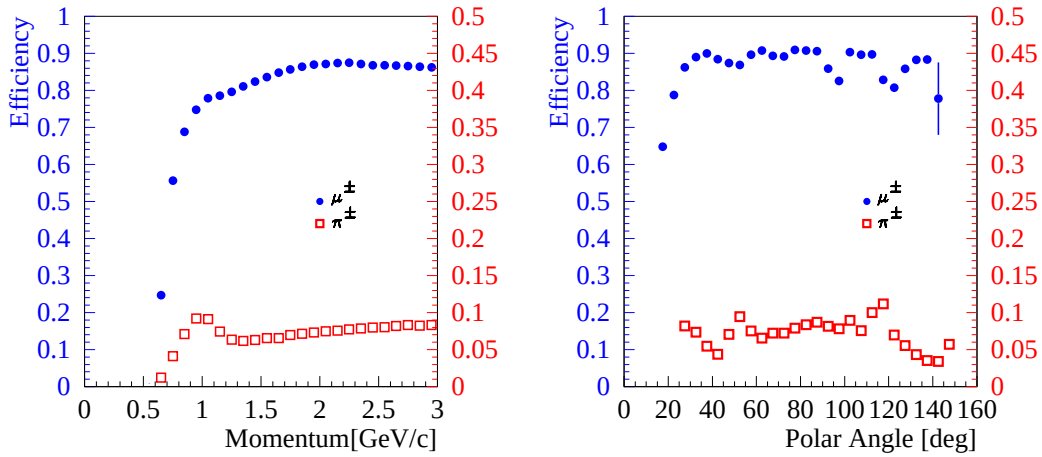

Figure 2.21: The muon efficiency and pion misidentification probability as a function of: (left plot) momentum of the particle in the laboratory frame; (right plot) polar angle of the particle in the laboratory frame. The muon efficiency is measured using muons from $e^+e^- \to \mu^+\mu^-\gamma$ and $e^+e^- \to \mu^+\mu^-e^+e^-$ events. The pion misidentification probability is measured using charged pions from K_S^0 decays and three-prongs τ decays.

identified as clusters of hits not associated to a charged track. According to Monte Carlo simulations, about 64% of the K_L^0s with momentum greater than 1 GeV/c is reconstructed as a cluster of hits in the IFR. The direction of the neutral hadron is determined from the event vertex and the centroid of the neutral cluster. If the K_L^0 starts to interact in the EMC, the cluster in the IFR is associated to a neutral shower in the calorimeter if there is a match in the corresponding directions.

Performances of K_L^0 reconstruction are derived using samples of K_L^0 selected from $e^+e^- \to \phi\gamma \to K_L^0 K_S^0 \gamma$ events. The K_L^0 detection efficiency increases roughly linearly with momentum. It varies from 20% to 40% in the momentum range from 1 GeV/c to 4 GeV/c. An angular resolution of the order of 60 $mrad$ is achieved.

2.2.5 The trigger system

The trigger system consists of a sequence of two independent stages: the Level 1 (L1) trigger, implemented in hardware, and the Level 3 (L3) trigger, implemented in software. The L1 trigger interpretes incoming detector signals,

and recognizes and removes beam-induced background to a level acceptable for the subsequent stage. The software of the L3 trigger runs on a farm of commercial processors.

Level 1 trigger

The L1 trigger is designed to provide an output trigger rate < 2 KHz, and has a latency of $11 - 12\ \mu s$ after the beam crossing. It is based on data from DCH, EMC, and IFR. The DCH trigger identifies long and short tracks down to $p_T = 120\,\text{MeV}$. The EMC trigger identifies energy deposits above a certain threshold, chosen to be as small as 100 MeV in order to efficiently recognize minimum ionizing particles. The IFR trigger identifies $\mu^+\mu^-$ and cosmic rays for diagnostic purposes. At a luminosity of $2.2 \cdot 10^{33}\, cm^{-2}s^{-1}$ the L1 trigger efficiency for $B\overline{B}$ events is $> 99.9\%$, and the typical L1 rate is 970 Hz, stable to within 20% for the same machine configuration.

Level 3 trigger

The L3 software algorithms select events of interest that are then stored for processing. It receives the output from L1, performs a second stage reduction for the main physics sources, and identifies and flags the special categories of events needed for luminosity determination, diagnostic and calibration purposes. The L3 trigger retains events in which the track candidates point back to the beam interaction region (L3 DCH trigger), or there are EMC cluster candidates with energy greater than a minimum ionizing particle, and correlated in time with the rest of the event (L3 EMC trigger). At the design luminosity, the L3 acceptance rate for physics is ~ 90 Hz, and the efficiency for $B\overline{B}$ events is $> 99.9\%$.

Chapter 3

Introduction to the study of the $B^{\pm} \to J/\psi\,\pi^{\pm}$ mode

Studies of non-leptonic decays of B mesons are very useful to gain a better understanding of the dynamics of strong interactions, which are responsible for the bounding of quarks and gluons into hadrons. The complexity of the processes involved in non-leptonic decays is illustrated in Fig. 3.1, where it is shown how strong interactions of quarks can affect a simple $b \to c\overline{u}d$ tree diagram. Several approaches have been developed by theorists in order to obtain reliable predictions for these decays. In particular, a factorization prescription allows us to write the decay amplitude in terms of a product of hadronic current matrix elements.

This chapter represents a brief theoretical introduction to the study of the $B^{\pm} \to J/\psi\,\pi^{\pm}$ decay mode. The principles and the limits of the factorization-based approach, widely used for the treatment of non-leptonic decays, are described, and the properties of the $B^{\pm} \to J/\psi\,\pi^{\pm}$ channel are then discussed.

3.1 The effective Hamiltonian

Let us consider, as an example of two-body non-leptonic decay, the mode $\overline{B}^0 \to D^+\pi^-$. The basic diagram for this process is shown in Fig. 3.2, in which we can distinguish a tree diagram $b \to c\overline{u}d$ and a spectator quark $\overline{d}$. Strong interactions affect this simple W-exchange in different ways, according to the energy of the exchanged gluons. Short-range interactions, characterized by energy scales $> \Lambda_{QCD}$, can be described by perturbative QCD, while long-

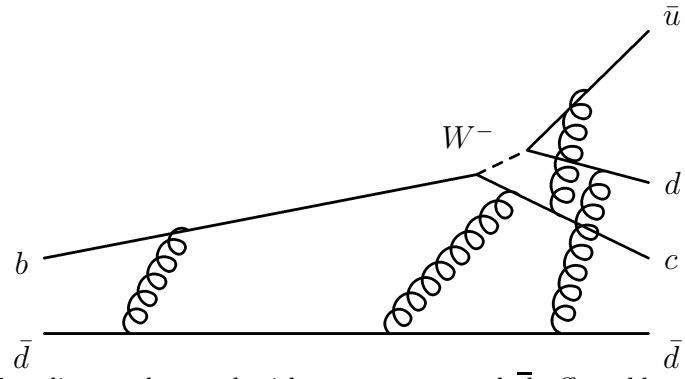

Figure 3.1: Tree diagram $b \to c\overline{u}d$, with a spectator quark $\overline{d}$, affected by gluon exchanges.

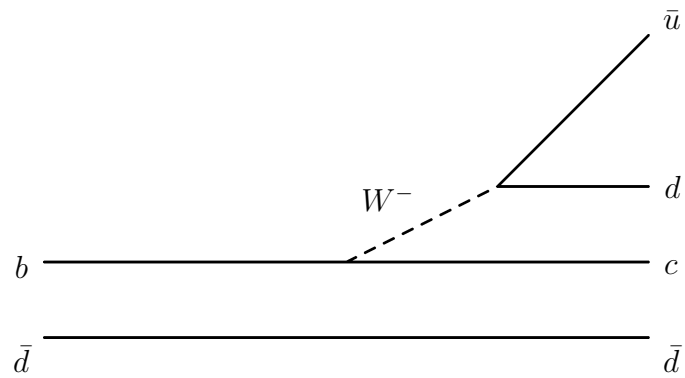

Figure 3.2: The tree diagram for the decay $\overline{B}^0 \to D^+\pi^-$.

range interactions, characterized by energy scales $\leq \Lambda_{QCD}$, cannot be treated perturbatively.

In order to manage these complicate effects, the technique known as the *Operator Product Expansion* [23] is used to write the amplitude of a generic decay $B \to f$ as:

$$A = -\frac{G_F}{\sqrt{2}} V_{CKM} \sum_j C_j \cdot \langle f|O_j|B\rangle \left[1 + O\left(\frac{m_b^2}{M_W^2}\right)\right], \tag{3.1}$$

where the *Wilson coefficients* C_j are independent of the final state f, the O_j are local four-quarks operators and V_{CKM} represents the product of the CKM matrix elements for the decay considered. The coefficients C_j can be interpreted as the "universal" coupling constants of the following effective Hamiltonian:

$$H_{\text{eff}} = \frac{G_F}{\sqrt{2}} V_{CKM} \sum_j C_j(\mu) O_j(\mu) + h.c. \quad , \tag{3.2}$$

where we have shown explicitly that the operators O_j are renormalized at the energy scale μ. The μ-dependence of the Wilson coefficients assures that the physics is independent of the renormalization scale. However, an appropriate choice of μ permits to disentangle the physics of hard QCD interactions from the physics of soft gluon exchanges. Indeed, the effects of the heavy degrees of freedom, which have been integrated out of the theory, are included in the coefficients C_j. They therefore need to be evaluated at a scale μ where a perturbative expansion is possible. The effects of long-distance interactions, instead, are included in the hadronic matrix elements $< f|O_j|B >$ and cannot be evaluated by perturbative methods.

The structure of the relevant operators O_j depends on the particular process. For $b \to c\overline{u}d$ transitions the effective hamiltonian is:

$$H_{\text{eff}} = \frac{4G_F}{\sqrt{2}} V_{cb} V_{ud}^* [C_1(\mu) O_1(\mu) + C_2(\mu) O_2(\mu)], \tag{3.3}$$

with:

$$O_1 = \left(\overline{c}_i \gamma_\mu \frac{1-\gamma_5}{2} b_i\right) \left(\overline{d}_j \gamma^\mu \frac{1-\gamma_5}{2} u_j\right) \tag{3.4}$$

$$O_2 = \left(\overline{c}_i \gamma_\mu \frac{1-\gamma_5}{2} b_j\right) \left(\overline{d}_j \gamma^\mu \frac{1-\gamma_5}{2} u_j\right), \tag{3.5}$$

where the Roman indices give the explicit color structure of the quarks. For B mesons decays, a reasonable choice of the scale is $\mu \sim m_b$. The coefficients $C_{1,2}$ evaluated at this scale have values $C_1 \approx 1.13$, $C_2 \approx -0.29$ (while in the limit of no QCD corrections: $C_1 = 1$, $C_2 = 0$).

3.2 The factorization prescription

From Eq. 3.1 we see that the amplitude for a non-leptonic decay depends on complicate hadronic matrix elements $< f|O_j|B >$, whose evaluation is not trivial. The factorization hypothesis overcomes these difficulties by replacing the hadronic matrix elements with more manageable products of current matrix elements. In the following we illustrate how factorization works considering three types of decays.

3.2.1 Type-I decays

In the decay $\overline{B}^0 \to D^+\pi^-$ the $(\overline{u}d)$ quark pair is produced as a point-like, color-singlet state. Since the energy released to the pair is quite high, it

can escape from the quark-gluon cloud before it reaches the size of a meson and the corresponding color dipole becomes relevant. This *color transparency* argument [24] allows us to neglect the interactions of the light meson with the rest of the quark-gluon system and to factorize the hadronic matrix elements:

$$< D\pi|O_{1,2}|B >=< D|\overline{c}\gamma_\mu \frac{1-\gamma_5}{2} b|B >< \pi|\overline{d}\gamma_\mu \frac{1-\gamma_5}{2} u|0 > , \tag{3.6}$$

where the color structures of $O_{1,2}$ have been omitted. Considering also the color structures, we can expect a suppression factor of $1/N_c$ for the O_2 amplitude, where $N_c = 3$ is the number of colors. Therefore we can write the amplitude of the decay as:

$$A = -i\,\frac{4G_F}{\sqrt{2}}\,V_{cb}V_{ud}^{*}\,a_1 < D|\overline{c}\gamma_\mu \frac{1-\gamma_5}{2} b|B >< \pi|\overline{d}\gamma_\mu \frac{1-\gamma_5}{2} u|0 >, \tag{3.7}$$

where:

$$a_1 = C_1 + \frac{1}{N_c} C_2 \sim 1. \tag{3.8}$$

The current matrix elements are parameterized with the use of form factors and decay constants:

$$< \pi|\overline{d}\gamma_\mu \frac{1-\gamma_5}{2} u|0 > \;=\; i f_\pi q_\mu \tag{3.9}$$

$$\begin{aligned} < D|\overline{c}\gamma_\mu \frac{1-\gamma_5}{2} b|B > \;&=\; F_1(q^2)\left[(p_B+p_D)_\mu - \frac{M_B^2 - M_D^2}{q^2}\,q_\mu\right] + \\ &+\; F_0(q^2)\frac{M_B^2 - M_D^2}{q^2}\,q_\mu, \end{aligned} \tag{3.10}$$

where q_μ is the four-momentum transferred to the pion ($q^2 = m_\pi^2$). The pion decay constant $f_\pi \approx 131\,\mathrm{MeV}$ is obtained from the leptonic decay $\pi^+ \to \mu^+\nu_\mu$ and it is known with good accuracy. The form factors of the heavy-to-heavy transition $B \to D$ come from the covariant decomposition of the current matrix element. In general, there are two form factors (F_0, F_1) if the daughter meson is pseudoscalar, while four form factors (V, A_0, A_1, A_2) are defined for a vector meson. Large theoretical uncertainties and model dependencies can affect the knowledge of these form factors.

For heavy-to-heavy transitions, heavy-quark symmetry [25] implies constraints on the form factors. For instance, in the case of a pseudoscalar daugh-

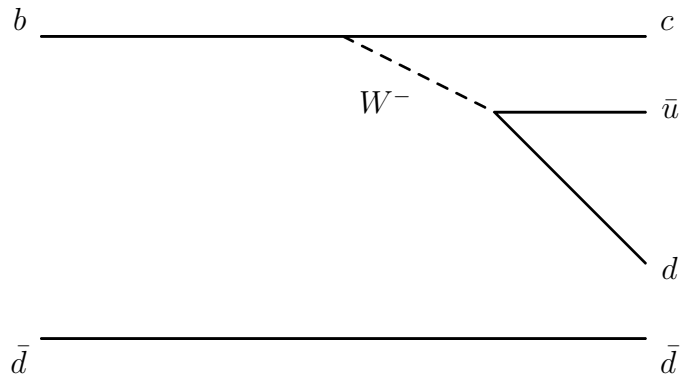

Figure 3.3: The tree diagram for the decay $\overline{B}^0 \to D^0\pi^0$.

ter meson:

$$F_1(q^2) = \frac{m_B + m_D}{2\sqrt{m_B m_D}} \cdot \xi(\omega) \tag{3.11}$$

$$F_0(q^2) = \frac{2\sqrt{m_B m_D}}{m_B + m_D} \cdot \frac{\omega + 1}{2} \cdot \xi(\omega), \tag{3.12}$$

where $\omega = v_B \cdot v_D$ is the product of the four-velocities of the two mesons, and $\xi(\omega)$ is the Isgur-Wise function [26, 27]. The deviations due to the finite masses of the heavy quarks can be analized in detail with the use of the *Heavy Quark Effective Theory* [25]. Finally, from the study of semileptonic decays it is possible to extract reliable predictions for these form factors.

Decays that are described by a tree diagram as in Fig. 3.2 are denoted as Type-I (or color-allowed) transitions. For energetic decays, color transparency suggests that factorization works properly and they are well described by a "universal" coefficient $a_1 \sim 1$.

3.2.2 Type-II decays

The decay $\overline{B}^0 \to D^0\pi^0$, described by the tree diagram in Fig. 3.3, is allowed if the quark pair $(\overline{u}c)$ has the right color structure to form a meson. This is equivalent, as the color structure of the operators $O_{1,2}$ suggests, to a suppression factor of $1/N_c$ for the O_1 amplitude. Therefore we can write the decay amplitude as:

$$A = -i\,\frac{4G_F}{\sqrt{2}}\,V_{cb}V_{ud}^*\,a_2 < \pi|\overline{d}\gamma_\mu\frac{1-\gamma_5}{2}b|B >< D|\overline{u}\gamma_\mu\frac{1-\gamma_5}{2}c|0 >, \tag{3.13}$$

where:

$$a_2 = C_2 + \frac{1}{N_c} C_1 \sim 0.1 \quad . \tag{3.14}$$

The current matrix elements are again parameterized with the use of form factors and decay constants as in Eq. 3.9 and Eq. 3.10, with q_μ that now represents the four-momentum transferred to the D meson ($q^2 = m_D^2$). For heavy-to-light transitions like $B \to \pi$ the constraints from heavy-quark symmetry cannot be exploited. Usually, phenomenological models based on several assumptions are used to evaluate these form factors, and factorization-based predictions are therefore affected by large theoretical uncertainties and model dependencies.

Decays described by a tree diagram as in Fig. 3.3 are denoted as Type-II (or color-suppressed) transitions. Two-body decays with a charmonium resonance in the final state, like $B^{\pm} \to J/\psi\,\pi^{\pm}$ or $B^{\pm} \to J/\psi\,K^{\pm}$, belong to this category. We point out that in this case there are no color transparency arguments justifying factorization of the hadronic matrix elements: non-factorizable contributions can become dominant and change relevantly the predictions obtained with the factorized amplitudes. There are also experimental results that suggest departure from simple factorization. For instance, measurements of the decay amplitudes in the $B \to J/\psi\,K^*(892)$ mode [28, 29] show discrepancies with the expectations based on the absence of final state interactions (as it is supposed in the simple factorization scheme).

3.2.3 Type-III decays

Decays like $B^- \to D^0\pi^-$ are described by both color-allowed and color-suppressed diagrams and therefore are sensitive to interference terms between them. In the limit of validity of factorization, the relative sign of a_1 and a_2 suggests that for decays of B mesons the interference is constructive.

3.3 Deviations from factorization

Using Fierz identities, it is possible to write the effective Hamiltonian in Eq. 3.3 as the sum of a color-singlet operator O_1 and a color-octet operator $O^{(8)}$. This implies also a transformation of the Wilson coefficients; in particular: $C_1 \to C_1 + (C_2/N_c)$. We obtain the following transformed decay

amplitude for a type-I decay:

$$A = -i\,\frac{4G_F}{\sqrt{2}}\,V_{cb}V_{ud}^{*}\,\{\,[C_1 + (1/N_c)C_2]\,\mathcal{M}_1 + 2\,C_2\mathcal{M}_8\,\}, \tag{3.15}$$

where:

$$\mathcal{M}_1 = <\pi D|O_1|B> \tag{3.16}$$
$$\mathcal{M}_8 = <\pi D|O^{(8)}|B>\,. \tag{3.17}$$

The simple factorization approach described in the previous section is therefore based on the following assumptions:

1. Negligible contribution from the color-octet operator:

$$\mathcal{M}_8 \approx 0.$$

2. Assumption of factorization for the color-singlet matrix element:

$$\mathcal{M}_1 =< D|(\overline{c}b)_{V-A}|B >< \pi|(\overline{d}u)_{V-A}|0 >\,,$$

where $(\overline{c}b)_{V-A}$ is a simplified notation for $\overline{c}\gamma_\mu[(1-\gamma_5)/2]b$.

In order to describe deviations from factorization, the following parameters are introduced:

$$\epsilon_1 = \frac{\mathcal{M}_1}{< D|(\overline{c}b)_{V-A}|B >< \pi|(\overline{d}u)_{V-A}|0 >} - 1 \tag{3.18}$$
$$\epsilon_8 = \frac{\mathcal{M}_8}{< D|(\overline{c}b)_{V-A}|B >< \pi|(\overline{d}u)_{V-A}|0 >}. \tag{3.19}$$

The parameter ϵ_1 measures the deviation of $\mathcal{M}_1$ from the factorized form, while ϵ_8 measures the contribution from the octet-operator. Thus, the decay amplitude can be written in the general form:

$$A = -i\,\frac{4G_F}{\sqrt{2}}\,V_{cb}V_{ud}^{*}\,a_1^{\rm eff} < D|\overline{c}\gamma_\mu\frac{1-\gamma_5}{2}b|B >< \pi|\overline{d}\gamma_\mu\frac{1-\gamma_5}{2}u|0 >, \tag{3.20}$$

where:

$$a_1^{\rm eff} = [C_1 + (C_2/N_c)](1+\epsilon_1) + 2C_2\epsilon_8. \tag{3.21}$$

Also for class-II decays it is possible to define a coefficient $a_2^{\rm eff}$:

$$a_2^{\rm eff} = [C_2 + (C_1/N_c)](1+\tilde{\epsilon_1}) + 2C_1\tilde{\epsilon_8}\,. \tag{3.22}$$

We can see that, also assuming that factorization of $\mathcal{M}_1$ is well satisfied ($\tilde{\epsilon_1} \approx 1$), $a_2^{\rm eff}$ can be sensitive to octet operator admixture, due to the smallness of the term $C_2 + (C_1/N_c)$. In other words, while the simple factorization approach with $a_1^{\rm eff} \approx 1$ represents a reliable scheme for class-I decays, sizeble deviations from the predicted decay rates are not surprising for class-II decays.

3.4 Generalized factorization

It is still possible to preserve the factorization-based approach for the treatment of non-leptonic decays, despite significant non-factorizable contributions, if the coefficients $a_{1,2}^{\rm eff}$ are interpreted as phenomenological parameters to be fitted on data [30, 31]. Sets of theoretically and experimentally clean modes are used to extract $a_{1,2}^{\rm eff}$. These fitted values are then employed to obtain predictions for other decays [32]. The underlying assumption is, of course, a weak dependence of the parameters $a_{1,2}^{\rm eff}$ on the particular process, which is not supported by strong theoretical arguments and needs therefore to be tested on data.

In an equivalent approach, deviations from factorizations are described introducing additional parameters in the factorized amplitude [33]; again, the values of the parameters are derived from data.

For class-I decays, the comparison between the values of $a_1^{\rm eff}$ extracted from quite different channels supports the validity of simple factorization with $a_1^{\rm eff} \approx 1$. For class-II decays, data seem to agree with the assumption of weak dependence of $a_2^{\rm eff}$ on the particular process. However, the reliability of this conclusion is limited by the not well understood theoretical uncertainties affecting the heavy-to-light form factors used for these channels. It is therefore extremely important that predictions rely on well tested phenomenological models for the form factors.

3.5 Properties of the $B^{\pm} \to J/\psi\,\pi^{\pm}$ channel

The $B^{\pm} \to J/\psi\,\pi^{\pm}$ channel is a class-II decay, described at the leading order by the tree diagram $b \to c\bar{c}d$ in Fig. 3.4 [1]. According to the scheme outlined

[1] Actually the $b \to c\bar{c}d$ diagram describes the decay $B^- \to J/\psi\,\pi^-$. However, in the present chapter, and unless stated explicitly, with this notation we will denote also the

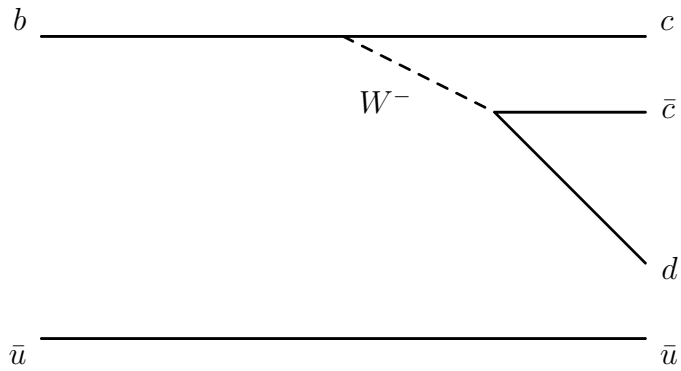

Figure 3.4: The tree diagram for the decay $B^- \to J/\psi\,\pi^-$.

in the previous sections, the factorized amplitude is given by:

$$A_{\rm tree}(B^\pm \to J/\psi\,\pi^\pm) \sim a_2^{\rm eff}\, V_{cb}^* V_{cd}\, f_{J/\psi}\; F_{B\to\pi}(q^2 = m_{J/\psi}^2)\,, \tag{3.23}$$

where $f_{J/\psi}$ is the decay constant of the J/ψ, and $F_{B\to\pi}$ denotes the form factors contribution. Similarly, the Cabibbo-allowed decay $B^\pm \to J/\psi\,K^\pm$ is described by the tree diagram $b \to c\bar{c}s$ and the factorized amplitude is:

$$A_{\rm tree}(B^\pm \to J/\psi\,K^\pm) \sim a_2^{\rm eff}\, V_{cb}^* V_{cs}\, f_{J/\psi}\; F_{B\to K}(q^2 = m_{J/\psi}^2)\,. \tag{3.24}$$

If the tree diagram is the dominant contribution for both decays ($A = A_{\rm tree}$), the ratio of the branching fractions is an interesting quantity because it does not depend on the particular value of $a_2^{\rm eff}$ (sensitive to non-factorizable contributions):

$$\frac{\mathcal{B}(B^\pm \to J/\psi\,\pi^\pm)}{\mathcal{B}(B^\pm \to J/\psi\,K^\pm)} = \frac{|V_{cd}|^2}{|V_{cs}|^2}\cdot\frac{|F_{B\to\pi}|^2}{|F_{B\to K}|^2} \sim \tan\theta_C{}^2\,\frac{|F_{B\to\pi}|^2}{|F_{B\to K}|^2}\,, \tag{3.25}$$

where θ_C is the Cabibbo angle. Therefore we expect for the $B^\pm \to J/\psi\,\pi^\pm$ mode a branching fraction of the order of 5% of $\mathcal{B}(B^\pm \to J/\psi\,K^\pm)$. In addition, the ratio of the branching fractions is sensitive to the quality of the phenomenological models employed to compute the heavy-to-light form factors in $F_{B\to\pi}$ and $F_{B\to K}$. A calculation of the above amplitudes gives [32]:

$$\mathcal{B}(B^\pm \to J/\psi\,\pi^\pm) = 0.038\,(a_2^{\rm eff})^2 \tag{3.26}$$

$$\mathcal{B}(B^\pm \to J/\psi\,K^\pm) = 0.852\,(a_2^{\rm eff})^2\,, \tag{3.27}$$

CP-conjugate decay $B^+ \to J/\psi\,\pi^+$.

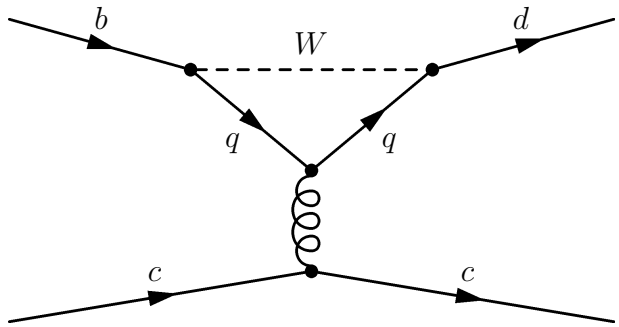

Figure 3.5: The gluonic penguin diagram ($q = u, c, t$).

and thus:

$$\frac{\mathcal{B}(B^{\pm} \to J/\psi\,\pi^{\pm})}{\mathcal{B}(B^{\pm} \to J/\psi\,K^{\pm})} = 0.045\,. \tag{3.28}$$

Because of the simplicity of the phenomenological model used for the determination of the form factors, the theoretical expectation in Eq. 3.28 has to be considered no more than a rough estimate of the ratio, and therefore no uncertainties are provided with the prediction.

While the tree diagram dominance is a reliable hypothesis for the $B^{\pm} \to J/\psi\,K^{\pm}$ channel, the Cabibbo-suppressed $B^{\pm} \to J/\psi\,\pi^{\pm}$ mode may be sensitive to higher order contributions from additional operators in the effective Hamiltonian. They correspond to 1-loop diagrams known as "penguin diagrams". Figure 3.5 shows a gluonic (or QCD) penguin; we distinguish three possible diagrams, characterized by the identity of the quark in the loop. Electroweak penguins are also possible, characterized by the emission of a photon or a Z^0 (see Fig. 3.6).

Penguin diagrams lead to deviations from the simple expectation stated in Eq. 3.25. Furthermore, they weaken the reliability of the theoretical prediction because uncertainties on penguin diagrams calculations sum up with the uncertainties on the form factors. Finally, the interference between the tree diagram and penguin diagrams with different weak and strong phases can produce significant direct CP-violation in $B^{\pm} \to J/\psi\,\pi^{\pm}$ decays.

3.5.1 Direct CP-violation in $B^{\pm} \to J/\psi\,\pi^{\pm}$ decays

Denoting with T the contribution from the tree diagram and with P^q the contribution from the penguin diagram with the quark q in the loop ($q =$

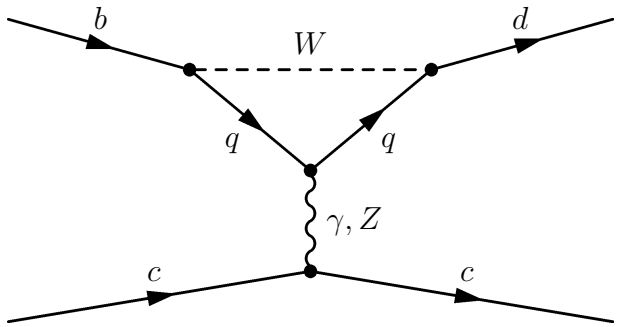

Figure 3.6: The electroweak penguin diagram ($q = u, c, t$).

u, c, t), the total amplitude for the $B^- \to J/\psi\,\pi^-$ mode can be written as:

$$A(B^- \to J/\psi\,\pi^-) = V_{tb}V_{td}^*\,P^t + V_{cb}V_{cd}^*\,(T + P^c) + V_{ub}V_{ud}^*\,P^u\,, \tag{3.29}$$

where we have shown explicitly the CKM matrix coefficients. From the unitarity of the CKM matrix we have:

$$V_{tb}V_{td}^* = -V_{cb}V_{cd}^* - V_{ub}V_{ud}^*\,, \tag{3.30}$$

that, substituded in Eq. 3.29, yields:

$$A(B^- \to J/\psi\,\pi^-) = V_{cb}V_{cd}^*\,(T + P^c - P^t) + V_{ub}V_{ud}^*\,(P^u - P^t)\,. \tag{3.31}$$

We note that in the above expression only differences of penguin contributions appear, in which the ultraviolet divergences associated to the quark loop cancel out.

The calculation of the Wilson coefficients for the penguin operators suggests a suppression factor for penguin contributions of the order of 10^{-2}. Thus, neglecting $P^c - P^t$ we can write the amplitude in the following form:

$$A(B^- \to J/\psi\,\pi^-) \approx \xi_c\,a_2\,e^{i\Delta} + \xi_u\,b\,, \tag{3.32}$$

where $\xi_c \equiv V_{cb}V_{cd}^*$, $\xi_u \equiv V_{ub}V_{ud}^*$, a_2 and b are the magnitudes of T and $P^u - P^t$ respectively, and Δ is the strong phase difference between the two terms in the sum.

The weak structure of the two contributions to the amplitude can be examined from the Wolfenstein parameterization of the CKM matrix (Eq. 1.15):

$$\xi_c \sim A\lambda^3 \tag{3.33}$$

$$\xi_u \sim A\lambda^3\,(\rho - i\,\eta)\,. \tag{3.34}$$

Since the two contributions are characterized by different weak phases, the existence of direct *CP*-violation relies on the condition $\Delta \neq 0$. Considering also the amplitude for the $B^+ \to J/\psi\,\pi^+$ decay:

$$A(B^+ \to J/\psi\,\pi^+) \approx \xi_c^*\, a_2\, e^{i\Delta} + \xi_u^*\, b\,, \tag{3.35}$$

the *CP*-violation observable will be given by:

$$\begin{aligned} \mathcal{A}_\pi &= \frac{\Gamma(B^- \to J/\psi\,\pi^-) - \Gamma(B^+ \to J/\psi\,\pi^+)}{\Gamma(B^- \to J/\psi\,\pi^-) + \Gamma(B^+ \to J/\psi\,\pi^+)} = \\ &= \frac{2\, a_2\, b\, \sin\Delta\, \sin\gamma\, \left|\frac{\xi_u}{\xi_c}\right|}{a_2^2 + \left|\frac{\xi_u}{\xi_c}\right|^2 b^2 + 2\, a_2\, b\, \left|\frac{\xi_u}{\xi_c}\right| \cos\Delta\, cos\gamma}\,, \end{aligned} \tag{3.36}$$

where γ is one of the angles of the Unitarity Triangle:

$$\gamma = \mathrm{Arg}\left[-\frac{\xi_u^*}{\xi_c^*}\right]\,.$$

Exploiting the dominance of the a_2^2 term in the denominator, we have:

$$\mathcal{A}_\pi = 2\,\frac{b}{a_2}\,\sin\Delta\,\sin\gamma\,\left|\frac{V_{ub}\,V_{ud}}{V_{cb}\,V_{cd}}\right|\,. \tag{3.37}$$

It has been shown [34] that values of $b/a_2 \approx 0.05$ are possible; the calculation for strong penguins is affected by large theoretical uncertainties, but for electroweak penguins it is quite reliable. Furthermore, the strong phase difference Δ could be large. This results in a direct *CP*-violation for the $B^{\pm} \to J/\psi\,\pi^{\pm}$ mode that can be at the percent level. However, since the uncertainty on this prediction is large, the asymmetry could be significantly smaller.

We conclude this discussion showing that no direct *CP*-violation is expected in the SM for the $B^{\pm} \to J/\psi\,K^{\pm}$ channel. Indeed in this case, also including the penguin contributions, we have:

$$A(B^- \to J/\psi\,K^-) = V_{cb}V_{cs}^*\,(T + P^c - P^t) + V_{ub}V_{us}^*\,(P^u - P^t)\,, \tag{3.38}$$

and since the second term in the sum is both Cabibbo-suppressed and penguin coupling constants-suppressed, we have:

$$A(B^- \to J/\psi\,K^-) \approx V_{cb}V_{cs}^*\,(T + P^c - P^t)\,. \tag{3.39}$$

Therefore the decay is approximately characterized by a single weak phase and no *CP*-violating interference terms are possible.

Chapter 4

Measurement of $\mathcal{B}(B^\pm \to J/\psi\,\pi^\pm)/\mathcal{B}(B^\pm \to J/\psi\,K^\pm)$

In this chapter we describe a measurement of the ratio of branching fractions $\mathcal{B}(B^\pm \to J/\psi\,\pi^\pm)/\mathcal{B}(B^\pm \to J/\psi\,K^\pm)$. The data that we have analyzed were recorded in 1999-2000 and the integrated luminosity is $20.7\,\mathrm{fb}^{-1}$, corresponding to 22.7 million $B\overline{B}$ pairs. The world average value of this ratio is $(5.1 \pm 1.4)\%$ [8] and is based on the measurements performed by the CLEO [35] and CDF [36] collaborations.

The number of $B^\pm \to J/\psi\,\pi^\pm$ events produced at the $\Upsilon(4S)$ is 20 times smaller than the number of $B^\pm \to J/\psi\,K^\pm$ events, while the kinematics of the decays is quite similar (see Fig. 4.1). For this reason it is difficult, with a simple "cut-and-count" analysis, to observe a $B^\pm \to J/\psi\,\pi^\pm$ signal characterized by a good signal-to-background ratio. Therefore our study of the $B^\pm \to J/\psi\,\pi^\pm$ channel is based on an alternative approach. We fully reconstruct $B^\pm \to J/\psi\,h^\pm$ ($h = \pi, K$) decays, and determine at one time the signal yields N_π and N_K from an unbinned maximum likelihood fit that exploits the kinematics of the decay to identify the $J/\psi\,\pi^\pm$, $J/\psi\,K^\pm$ and background components in the sample.

4.1 Selection of the data sample

In order to reduce the amount of data as input to the analysis, we use only events that have passed a pre-selection which enhances the number of $B\overline{B}$ and B^+B^- events over the background from $q\overline{q}$ continuum and QED processes.

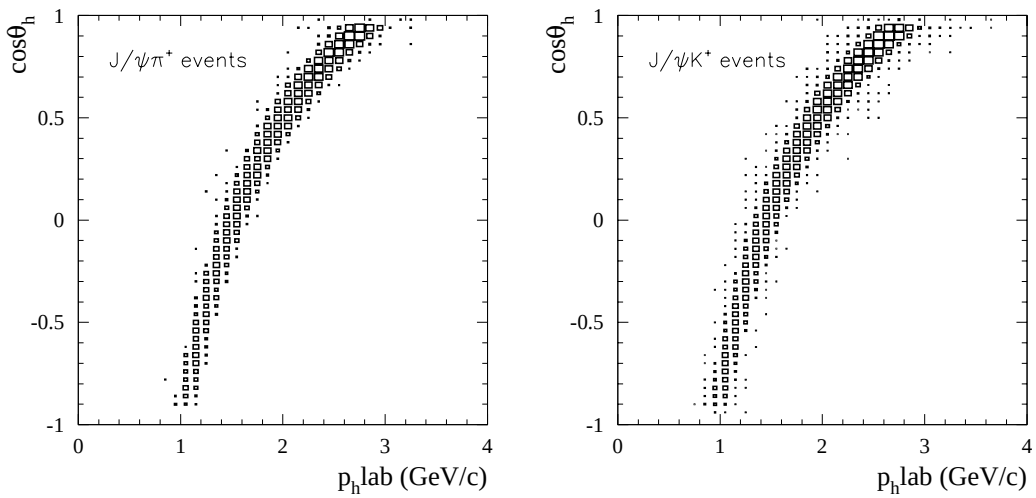

Figure 4.1: The $cos\theta$ vs. momentum distribution in the laboratory frame for the final state charged hadron in simulated $B^{\pm} \to J/\psi\,\pi^{\pm}$ (left plot) and $B^{\pm} \to J/\psi\,K^{\pm}$ (right plot) decays.

From these events we reconstruct a $B^{\pm}$ candidate as the combination of a J/ψ and a charged track in the SVT or the DCH. The J/ψ is reconstructed in the leptonic channel $J/\psi \to l^{+}l^{-}$ $(l = \mu, e)$ as the combination of two charged tracks that have been identified as leptons.

4.1.1 Pre-selection of the events

We define a fiducial volume of the detector as a region characterized by a well-measured reconstruction efficiency and an accurate modeling of the detector material in the Monte Carlo (MC) simulations. The fiducial volume for tracks is $0.41 < \theta_{lab} < 2.54\,rad$, while the fiducial volume for neutrals is $0.41 < \theta_{lab} < 2.409\,rad$. In addition, we consider only neutrals with an energy greater than 30 MeV.

The pre-selection is based on the following requirements:

1. The event must satisfy a physics trigger (L3 EMC or L3 DCH trigger).

2. At least three charged tracks must be in the fiducial volume. They must also include at least 12 DCH hits, to ensure that their momenta and $\mathrm{d}E/\mathrm{d}x$ are well measured. In addition they are required to have

$p_T > 100\,\mathrm{MeV}/c$, and to point back to the nominal interaction point within $1.5\,cm$ in the xy-plane and $3\,cm$ along the z-axis.

3. The ratio R_2 of the second to the zeroth Fox-Wolfram moment [37] tends to 0 for $b\overline{b}$ events. We require that R_2 for the tracks and neutrals in the fiducial volume must be less than 0.5.

4. The primary vertex constructed from the tracks in the fiducial volume must be within $0.5\,cm$ of the beam spot in the xy-plane and within $6\,cm$ on the z-axis.

5. The total energy in the fiducial volume must be greater than $4.5\,\mathrm{GeV}$.

The efficiency of this pre-selection is 95.6%, as estimated with Monte Carlo simulations of generic $b\overline{b}$ events.

4.1.2 Reconstruction of the J/ψ candidates

A J/ψ meson is reconstructed in the leptonic channel $J/\psi \to l^+l^-$ $(l = \mu, e)$ as the combination of two charged tracks with a common vertex. In order to reject the hadron-hadron or hadron-lepton combinatorial background, lepton identification criteria have been applied to each of the tracks ("legs" of the J/ψ).

A $J/\psi \to \mu^+\mu^-$ candidate is constructed from two identified muons in the fiducial volume $0.3 < \theta_{lab} < 2.7\,rad$, dictated by the IFR angular acceptance. The variables used for muon identification are:

1. the energy deposited in the EMC (E_{EMC});

2. the number of IFR layers with hits (N_{layers});

3. the number of nuclear interaction lengths traversed in the detector (N_λ);

4. the difference between the number of nuclear interaction lengths traversed in the detector and the expectation for a muon with the same momentum and polar angle as the track ($|N_\lambda - N_\lambda^{exp}|$);

5. the average number of hits per IFR layer ($\langle N_{hit} \rangle$);

6. the RMS of the distribution of the number of hits on each layer (RMS_{hit});

Table 4.1: Muon selection algorithms applied in $J/\psi \to \mu^+\mu^-$ reconstruction. We also report the efficiency for muons in inclusive J/ψ events, and the average misidentification probability for pions with momentum above 1 GeV/c.

	MIP	Loose
E_{EMC} (GeV)	< 0.5	< 0.5
N_{layers}	–	> 1
N_{λ}	–	> 2
$\lvert N_{\lambda} - N_{\lambda}^{exp}\rvert$	–	< 2.0
$\langle N_{hit} \rangle$	–	< 10
RMS_{hit}	–	< 6
c_{trk}	–	> 0.2
χ^2_{trk}/N_{layers}	–	< 7.0
χ^2_{IFR}/N_{layers}	–	< 4.0
Efficiency (%)	99.6	86.2
π misidentification (%)	57.9	7.0

7. the ratio of N_{layers} to the number of IFR layers spanned by the track (c_{trk});

8. the χ^2 of the match between the hits in the IFR and the extrapolated track (χ^2_{trk});

9. the χ^2 of a polynomial fit to the hits in the IFR (χ^2_{IFR}).

One "leg" must pass the loose muon selection algorithm and the other the MIP selection (see Table 4.1). We require the invariant mass of the pair, computed after a vertex constraint, to be: $3.06 < M_{\mu^+\mu^-} < 3.14\,\mathrm{GeV}/c^2$.

A $J/\psi \to e^+e^-$ candidate is constructed from two identified electrons in the fiducial volume $0.41 < \theta_{lab} < 2.409$. The variables used for electron identification are:

1. the energy loss in the DCH ($\mathrm{d}E/\mathrm{d}x$);

2. the ratio of the energy released in the EMC to the track momentum (E/p);

3. the number of crystals in the EMC cluster (N_{crys});

4. the lateral energy distribution [39] of the EMC cluster (LAT).

Table 4.2: Electron selection algorithms applied in $J/\psi \to e^+e^-$ reconstruction. We also report the efficiency for electrons in inclusive J/ψ events, and the average misidentification probability for pions with momentum above $1\,\mathrm{GeV}/c$.

	DCH-only	Loose	Tight
$\mathrm{d}E/\mathrm{d}x$ (meas.) $-$ $\mathrm{d}E/\mathrm{d}x$ (exp.)	-2 to $+4\sigma_{meas}$	-3 to $+7\sigma_{meas}$	-3 to $+7\sigma_{meas}$
E/p	–	$0.65 - 5.0$	$0.75 - 1.3$
N_{crys}	–	> 3	> 3
LAT	–	–	$0.0 - 0.6$
Efficiency (%)	94.9	97.2	95.4
π misidentification (%)	21.6	4.8	1.2

One "leg" must pass the tight electron selection algorithm and the other the loose selection or, if not associated to an EMC cluster, the DCH-only selection (see Table 4.2). To increase the efficiency of the event selection, electron candidates are combined with photon candidates in the event in order to recover some of the energy lost through bremsstrahlung. The photon candidates are required to have a Zernike moment A_{42} [38] (which measures the azimuthal asymmetry of the EMC cluster) below 0.25, to be within $35\,mrad$ in θ from the track, and to have a ϕ between the initial track direction and the centroid of the EMC cluster associated to the track. We require the invariant mass of the pair, computed after a vertex constraint, to be: $2.95 < M_{e^+e^-} < 3.14\,\mathrm{GeV}/c^2$. Figure 4.2 shows the invariant mass distribution of the J/ψ candidates in the data.

4.1.3 Reconstruction and selection of $B^\pm$ candidates

$B^\pm$ candidates are obtained from the combination of a reconstructed J/ψ, constrained to the world average mass [8], and a charged track $h^\pm$ in the momentum range $1 < p_h < 3\,\mathrm{GeV}/c^2$ (see fig. 4.3).

The helicity angle of the J/ψ decay is a useful variable to reject the background. Let us consider the generic decay $Y \to X \to a + b$, and denote with J_X the spin of X, and with λ_X its projection along the direction of Y in the X rest frame (assumed as the spin quantization axis). Since this axis is equivalent to the direction of X in the Y rest frame, λ_X coincides with the helicity of X. Furthermore, let us denote with λ_a and λ_b the helicities

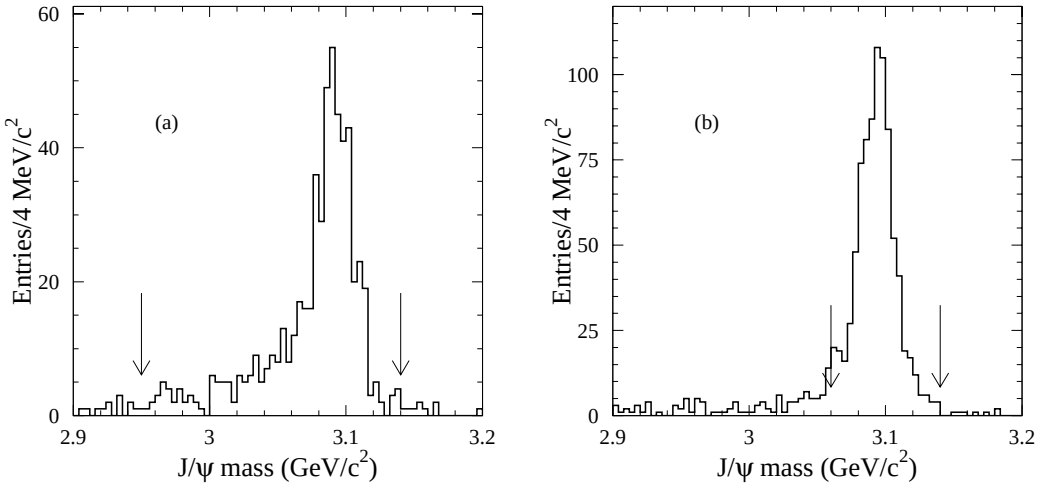

Figure 4.2: The invariant mass distribution for reconstructed $J/\psi \to e^+e^-$ (a) and $J/\psi \to \mu^+\mu^-$ (b) candidates. The requirements on the invariant mass are also displayed.

of a and b respectively. We define the helicity angle of the particle a as the angle θ_a, measured in the rest frame of X, between the direction of a and the direction of Y. The matrix element of the decay is proportional to the function $d^{J_X}_{\lambda_X,\lambda_a-\lambda_b}(\theta_a)$ [40].

The helicity angle θ_l for the decay $B^{\pm} \to J/\psi\,(\to l^+l^-)h^{\pm}$, with $h = \pi, K$, is shown in Fig. 4.4. The leptons in the $J/\psi \to l^+l^-$ decay are produced with opposite helicities:

$$\lambda_{l^+} - \lambda_{l^-} = \pm 1\,, \tag{4.1}$$

and, being $J_{J/\psi} = 1$, the θ_l distribution will be proportional to $|d^1_{\lambda_{J/\psi},\pm 1}|^2$. Since $h^{\pm}$ is a pseudoscalar meson, the J/ψ must be longitudinally polarized ($\lambda_{J/\psi} = 0$) and the resulting lepton angular distribution is proportional to $|d^1_{0,\pm 1}|^2 \sim sin^2\theta_l$. Figure 4.5 shows a typical $\cos\theta_l$ distribution for signal and background events: we observe that the background is highly peaked at ± 1. Indeed, in order to fake a $J/\psi \to l^+l^-$ decay, two random tracks are required to be back-to-back in separate jets. The $h^{\pm}$ track will lie in one of these jets, and thus will be close to one of the lepton candidates. We require $|cos\theta_l| < 0.9$ for $J/\psi \to \mu^+\mu^-$ events and $|cos\theta_l| < 0.8$ for $J/\psi \to e^+e^-$ events.

The J/ψ candidate and the charged track $h^{\pm}$ are constrained to a common vertex before computing the following kinematic quantities of the $B^{\pm}$

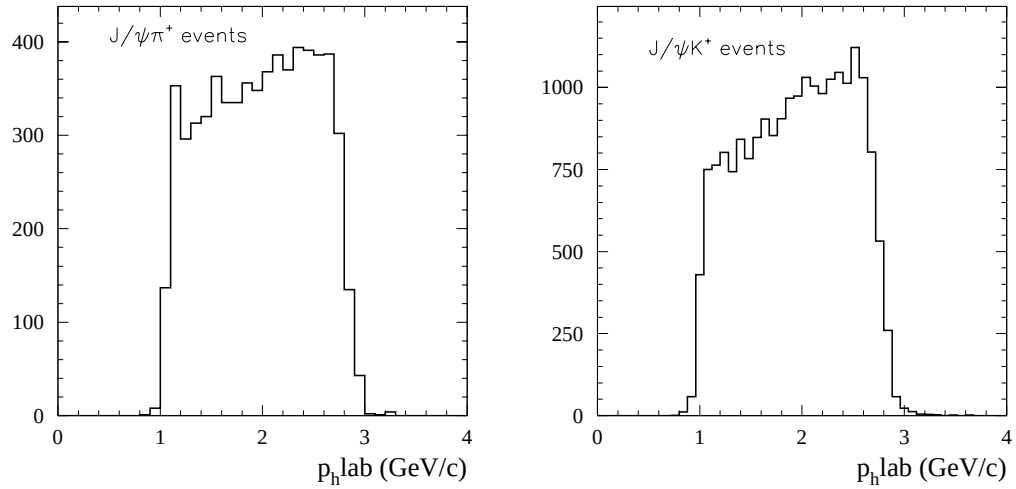

Figure 4.3: The momentum distribution in the laboratory frame for the final state charged hadron in simulated $B^{\pm} \to J/\psi\pi^{\pm}$ (left plot) and $B^{\pm} \to J/\psi K^{\pm}$ (right plot) decays.

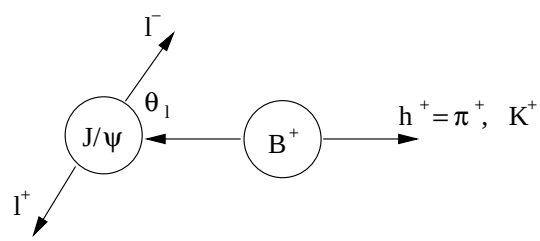

Figure 4.4: The helicity angle θ_l in the decay $B^{\pm} \to J/\psi(\to l^+l^-)h^{\pm}$.

candidate used to discriminate signal from background.

The ΔE variable

The ΔE variable is defined as:

$$\Delta E = E_B^{cm} - E_{beam}^{cm} \,, \tag{4.2}$$

where E_B^{cm} is the energy of the B candidate computed in the $\Upsilon(4S)$ rest frame, and E_{beam}^{cm} is the beam energy in the same frame. Because of the boost of the $\Upsilon(4S)$ in the laboratory, the computation of ΔE requires a Lorentz-transformation to the center-of-mass frame, which involves the mass

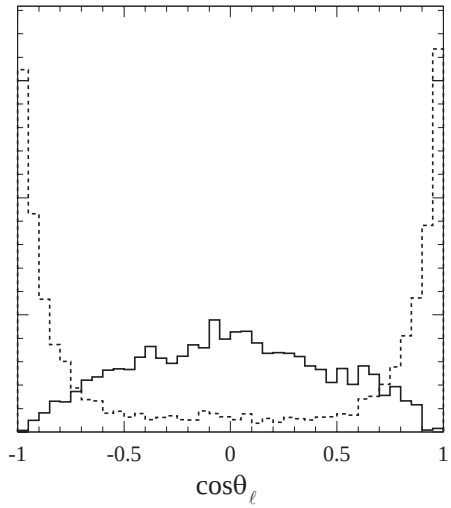

Figure 4.5: A typical distribution of $\cos\theta_l$ for $B^\pm \to J/\psi\,K^\pm$ (solid histogram) and background (dashed histogram) events.

hypothesis made on the track $h^\pm$. We denote as ΔE_π (ΔE_K) the ΔE variable computed with the pion (kaon) mass hypothesis. Signal events with the right mass hypothesis have ΔE close to 0 (see Fig. 4.6). In order to select both $B^\pm \to J/\psi\,\pi^\pm$ and $B^\pm \to J/\psi\,K^\pm$ events we require: $|\Delta E_\pi| < 120\,\mathrm{MeV}$ and $|\Delta E_K| < 120\,\mathrm{MeV}$.

The energy substituted mass m_{ES}

The energy substituted mass m_{ES} is defined as:

$$m_{ES} = \sqrt{[E^{cm}_{beam}]^2 - [p^{cm}_B]^2}\,, \tag{4.3}$$

where p^{cm}_B is the magnitude of the momentum of the B candidate in the $\Upsilon(4S)$ rest frame. According to the above definition, also the computation of this variable requires a Lorentz transformation involving the mass hypothesis made on $h^\pm$. However, m_{ES} can be computed indipendently of the mass hypothesis writing:

$$m_{ES} = \sqrt{[E^{lab}_B]^2 - [p^{lab}_B]^2}\,. \tag{4.4}$$

The quantity E^{lab}_B in Eq. 4.4 is obtained exploiting the relativistic invariance of the product $p_B \cdot p_{\Upsilon(4S)}$ (where p_B is the four-momentum of the B candidate

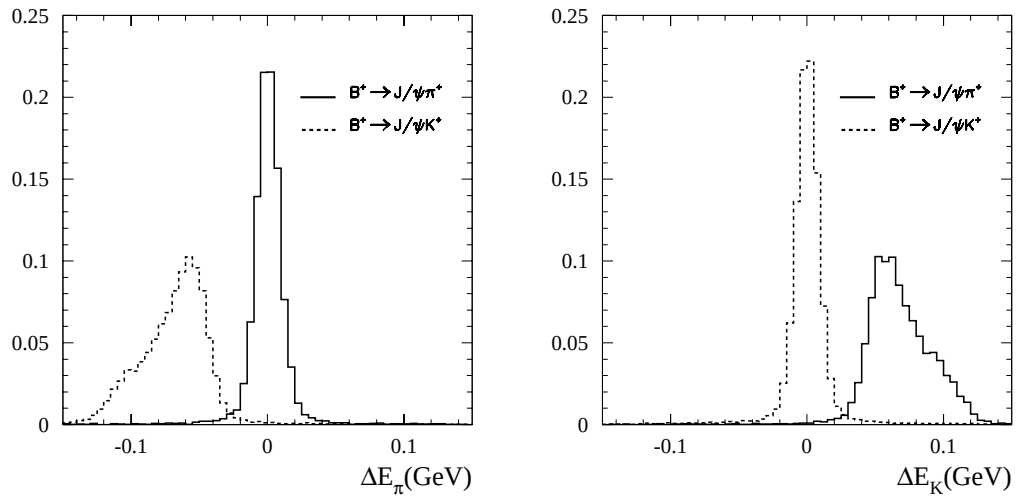

Figure 4.6: The distribution in ΔE_π (left plot) and ΔE_K (right plot) for simulated $B^\pm \to J/\psi\,\pi^\pm$ (solid histograms) and $B^\pm \to J/\psi\,K^\pm$ (dashed histograms) events.

and $p_{\Upsilon(4S)}$ is the four-momentum of the $\Upsilon(4S)$), and constraining $E_B^{cm} = E_{beam}^{cm}$:

$$\vec{p}_B^{\,lab} \cdot \vec{p}_{\Upsilon(4S)}^{\,lab} - E_B^{lab} E_{\Upsilon(4S)}^{lab} = -2[E_{beam}^{cm}]^2 \,. \tag{4.5}$$

Signal events have m_{ES} close to the $B^\pm$ meson mass, $5.279\,\mathrm{GeV}/c^2$ (see Fig. 4.7). The m_{ES} signal region is defined as $m_{ES} > 5.27\,\mathrm{GeV}/c^2$. We select events with $5.2 < m_{ES} < 5.3\,\mathrm{GeV}/c^2$.

4.2 The selected sample

The selected sample contains 1074 $B^\pm \to J/\psi\,(\to \mu^+\mu^-)h^\pm$ and 1081 $B^\pm \to J/\psi\,(\to e^+e^-)h^\pm$ candidates. Their distribution in the $(m_{ES}, \Delta E_K)$ plane is shown in fig. 4.8: the dominance of the $B^\pm \to J/\psi\,K^\pm$ component is evident.

The distribution in ΔE_K for events in the m_{ES} signal region is shown in Fig. 4.9. It has been fitted with the sum of a Gaussian and a polynomial function, modeling the $B^\pm \to J/\psi\,K^\pm$ signal and the background contribution respectively. The width of the Gaussian represents a measurement of the resolution in ΔE. Table 4.3 reports the resolutions estimated separately for $B^\pm \to J/\psi\,(\to \mu^+\mu^-)h^\pm$ and $B^\pm \to J/\psi\,(\to e^+e^-)h^\pm$ events.

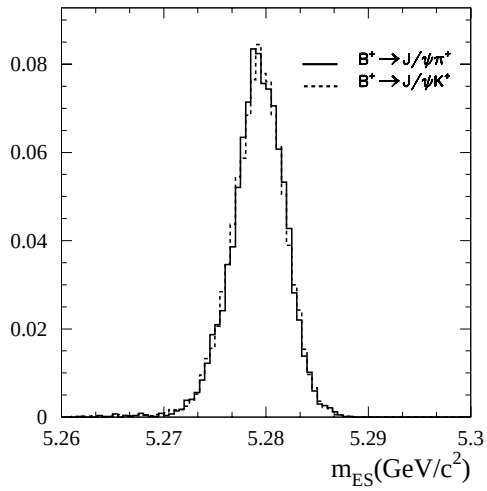

Figure 4.7: The distribution in m_{ES} for simulated $B^\pm \to J/\psi\,\pi^\pm$ (solid histograms) and $B^\pm \to J/\psi\,K^\pm$ (dashed histograms) events.

Table 4.3: Resolutions in ΔE and m_{ES} determined with a fit to data.

	$B^\pm \to J/\psi\,(\to \mu^+\mu^-)h^\pm$	$B^\pm \to J/\psi\,(\to e^+e^-)h^\pm$
$\sigma(\Delta E)$	$10.1 \pm 0.3\,\mathrm{MeV}$	$12.8 \pm 0.6\,\mathrm{MeV}$
$\sigma(m_{ES})$	$2.30 \pm 0.06\,\mathrm{MeV}/c^2$	$2.50 \pm 0.05\,\mathrm{MeV}/c^2$

The distribution in m_{ES} for events in the data sample is shown in Fig. 4.10. It has been fitted with the sum of a Gaussian and a phenomenological function, modeling the signal and the background contribution respectively. The phenomenological function is denoted as ARGUS function [41] and has the following form:

$$A(m_{ES}; m_0, c) \propto m_{ES}\sqrt{1-\left(\frac{m_{ES}}{m_0}\right)^2} \times \exp\left\{c \cdot \left[1-\left(\frac{m_{ES}}{m_0}\right)^2\right]\right\}, \quad (4.6)$$

where m_0 is set to the typical beam energy and c is a parameter to be fitted ("shape parameter"). The width of the Gaussian represents a measurement of the resolution in m_{ES}. Table 4.3 reports the resolutions estimated separately for $B^\pm \to J/\psi\,(\to \mu^+\mu^-)h^\pm$ and $B^\pm \to J/\psi\,(\to e^+e^-)h^\pm$ events.

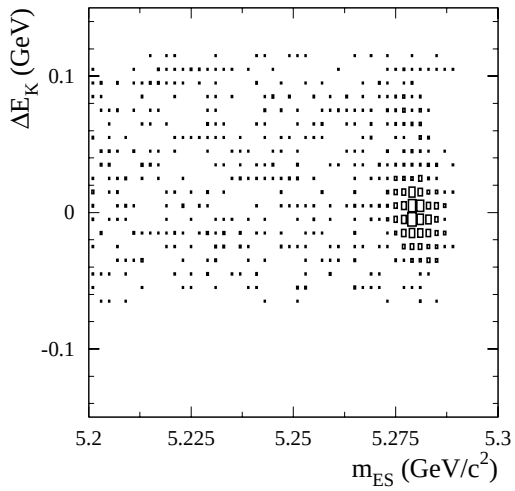

Figure 4.8: The ΔE_K vs. m_{ES} distributions for the selected data sample.

Table 4.4: Summary of the sidebands definitions.

	$B^\pm \to J/\psi(\to \mu^+\mu^-)h^\pm$	$B^\pm \to J/\psi(\to e^+e^-)h^\pm$
m_{ES} sideband	$m_{ES} < 5.27\,\mathrm{GeV}/c^2$	$m_{ES} < 5.27\,\mathrm{GeV}/c^2$
ΔE_K sideband	$\lvert\Delta E_K\rvert > 40.4\,\mathrm{MeV}$	$\lvert\Delta E_K\rvert > 51.2\,\mathrm{MeV}$
ΔE_π sideband	$\lvert\Delta E_\pi\rvert > 40.4\,\mathrm{MeV}$	$\lvert\Delta E_K\rvert > 51.2\,\mathrm{MeV}$

4.2.1 Background characterization

The background contaminating the sample is characterized with events in the data that are sufficiently removed from the typical signal regions (sidebands of the data sample).

We define m_{ES} sideband events by the requirement that $5.2 < m_{ES} < M_{B^\pm} - 4\sigma(m_{ES})$, where $M_{B^\pm}$ is the world average $B^\pm$ mass [8] and $\sigma(m_{ES})$ is the m_{ES} resolution. We define ΔE_π and ΔE_K sideband events by the requirements $|\Delta E_\pi| > 4\sigma(\Delta E)$ and $|\Delta E_K| > 4\sigma(\Delta E)$, where $\sigma(\Delta E)$ is the ΔE resolution. The sidebands definitions are summarized in Table 4.4.

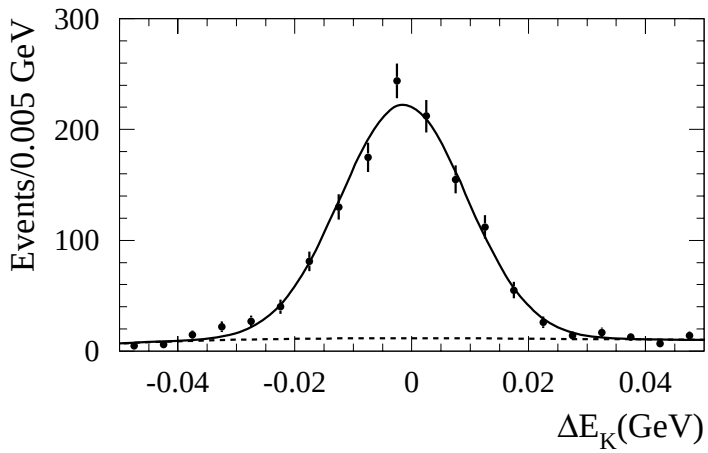

Figure 4.9: The distribution in ΔE_K and fit for events in the data sample with $m_{ES} > 5.27\,\mathrm{GeV}/c^2$. The dashed curve represents the background contribution.

4.2.2 Discriminating variables

We identify a set of three variables useful to discriminate between the $J/\psi\,\pi^\pm$, $J/\psi\,K^\pm$ and background components in the sample: $(\Delta E_\pi, \Delta E_K, m_{ES})$. Figure 4.11 shows the distributions of $B^\pm \to J/\psi\,\pi^\pm$, $B^\pm \to J/\psi\,K^\pm$, and background events in the $(\Delta E_\pi, \Delta E_K)$ plane. Since we choose both the ΔE_π and ΔE_K variables, we exploit all the information contained in Fig. 4.11. It is worthwhile to note that choosing $(\Delta E_\pi, \Delta E_K)$ is equivalent to choose the pair of variables $(\Delta E_\pi, p_h)$, where p_h is the momentum of the final state charged hadron $h^\pm$ in the laboratory frame. Indeed we have:

$$D \equiv \Delta E_K - \Delta E_\pi = \gamma \left(\sqrt{p_h^2 + m_K^2} - \sqrt{p_h^2 + m_\pi^2} \right) , \tag{4.7}$$

where γ is the Lorentz boost from the laboratory frame to the $\Upsilon(4S)$ rest frame, and m_π, m_K are the masses of the π and K mesons, respectively.

The separation provided by the above variables is sufficiently good, so that no explicit particle identification is required on the charged hadron $h^\pm$, thereby simplifying the analysis.

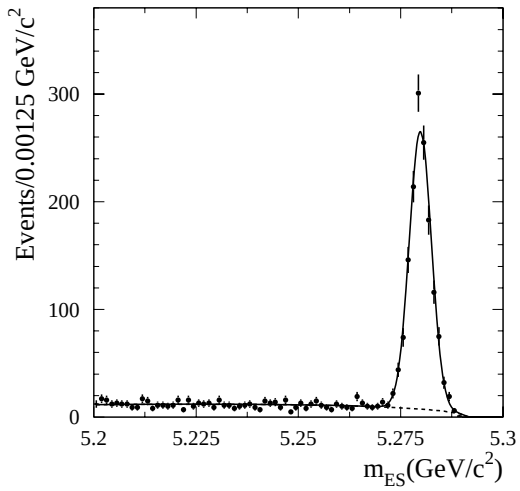

Figure 4.10: The distribution in m_{ES} and fit for events in the data sample.

4.3 The likelihood function

The yields N_i ($i = \pi, K, bkd$) for the $B^\pm \to J/\psi\,\pi^\pm$, $B^\pm \to J/\psi\,K^\pm$ and background events in the sample are determined maximizing a likelihood function that uses as arguments the variables identified in the previous section.

We denote with $P_i(\Delta E_\pi, \Delta E_K, m_{ES})$ the probability density functions (PDFs) in the $B^\pm \to J/\psi\,\pi^\pm$, $B^\pm \to J/\psi\,K^\pm$ and background event hypotheses. The probability to measure, in the j-th event of the data sample, the values $(\Delta E_\pi^j, \Delta E_K^j, {m_{ES}}^j)$ is given by:

$$\sum_i P_i(\Delta E_\pi^j, \Delta E_K^j, {m_{ES}}^j) \times \frac{N_i}{N}\,,$$

where N_i is the number of expected events for each hypothesis, and $N = \sum_i N_i$. Denoting with M the total number of observed events, the likelihood to obtaine the actual data sample is:

$$L = \mathcal{P}(M;N) \times \prod_{j=1}^{M} \sum_i P_i(\Delta E_\pi^j, \Delta E_K^j, {m_{ES}}^j) \times \frac{N_i}{N}\,, \tag{4.8}$$

where $\mathcal{P}(M;N)$ is the Poissonian probability to observe M events where N

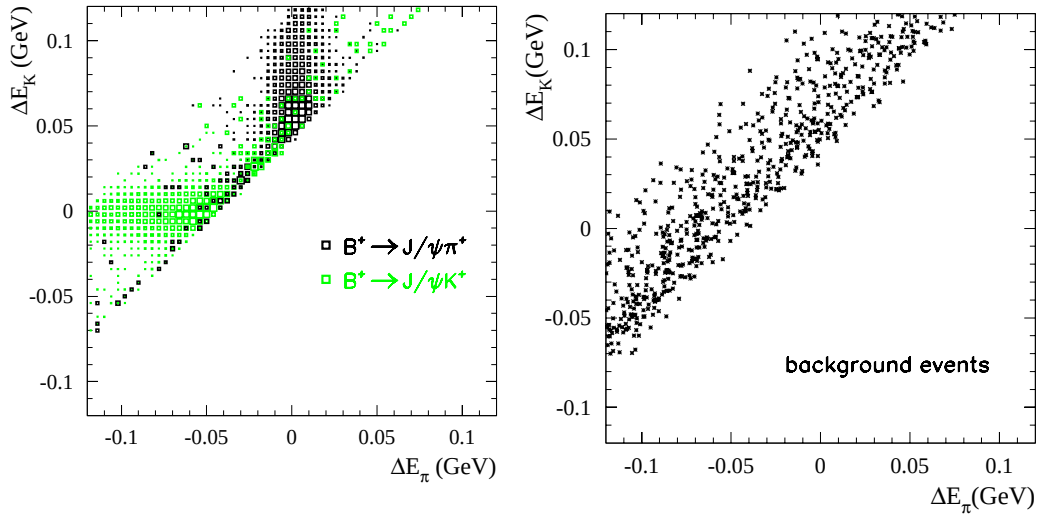

Figure 4.11: (left plot): Distribution of ΔE_K vs. ΔE_π for $B^\pm \to J/\psi\,K^\pm$ and $B^\pm \to J/\psi\,\pi^\pm$ events from Monte Carlo simulations. (right plot): Distribution of ΔE_K vs. ΔE_π for the events in the m_{ES} sideband of the data sample.

are expected:

$$\mathcal{P}(M;N) = N^M \times \frac{e^{-N}}{M!}\,. \tag{4.9}$$

Thus, apart from a constant factor $1/M!$, we obtain that the likelihood function [1] to maximize has the following form:

$$L(N_i) = e^{-N} \times \prod_{j=1}^{M} \sum_i P_i(\Delta E_\pi^j, \Delta E_K^j, m_{ES}{}^j)\, N_i\,. \tag{4.10}$$

4.3.1 Uncorrelated variables

Performing a likelihood fit to extract the yields N_i requires the characterization of the P_i PDFs. However, the study of multi-dimensional PDFs requires high statistics. Therefore it is preferable to express each P_i as the product of one-dimensional PDFs, which is a good approximation if the variables are weakly correlated. This is not the case for the $(\Delta E_\pi, \Delta E_K)$ variables, as evident from Fig. 4.11.

[1] Since the overall normalization N is allowed to vary, this likelihood function is also denoted as an "extended likelihood function".

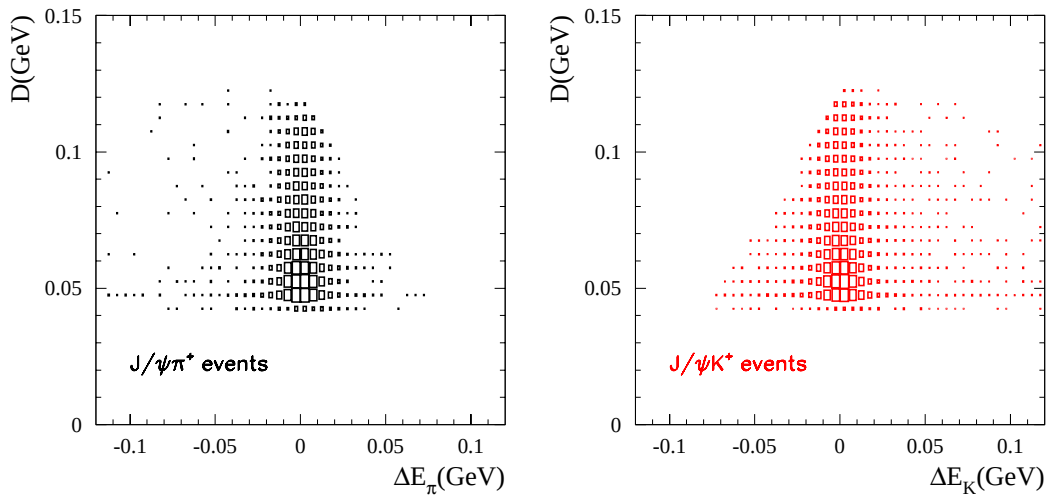

Figure 4.12: (left plot): The D vs. ΔE_π distribution for simulated $B^\pm \to J/\psi\,\pi^\pm$ events. (right plot): The D vs. ΔE_K distribution for simulated $B^\pm \to J/\psi\,K^\pm$ events.

Figure 4.12 shows that for $B^\pm \to J/\psi\,\pi^\pm$ events the variables $(\Delta E_\pi, D)$, where $D = \Delta E_K - \Delta E_\pi$, are less correlated than $(\Delta E_\pi, \Delta E_K)$. Similarly, for $B^\pm \to J/\psi\,K^\pm$ events the variables $(\Delta E_K, D)$ are less correlated than $(\Delta E_\pi, \Delta E_K)$. A quantitative estimate shows that the correlation of the new variables is at the 1% level.

Figure 4.13 shows that in the background case the variables (S, D), where $S \equiv \Delta E_K + \Delta E_\pi$, are less correlated than $(\Delta E_\pi, \Delta E_K)$. A quantitative estimate shows that the correlation of the new variables is at the 0.6% level.

For each hypothesis we perform a transformation to the weakly correlated variables. Thus, each $P_i(\Delta E_\pi, \Delta E_K, m_{ES})$ can be written as a product of one-dimensional PDFs:

$$P_\pi(\Delta E_\pi, \Delta E_K, m_{ES}) = f_\pi(\Delta E_\pi)\, g_\pi(D)\, h_\pi(m_{ES}) \tag{4.11}$$

$$P_K(\Delta E_\pi, \Delta E_K, m_{ES}) = f_K(\Delta E_K)\, g_K(D)\, h_K(m_{ES}) \tag{4.12}$$

$$P_{bkd}(\Delta E_\pi, \Delta E_K, m_{ES}) = 2\, f_{bkd}(S)\, g_{bkd}(D)\, h_{bkd}(m_{ES})\,. \tag{4.13}$$

The factor 2 in Eq. 4.13 is the inverse of the Jacobian of the transformation $(\Delta E_\pi, \Delta E_K, m_{ES}) \to (S, D, m_{ES})$; for the other transformations the Jacobian is 1.

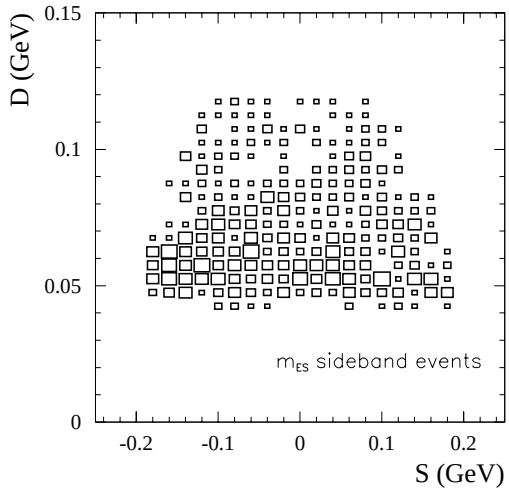

Figure 4.13: The D vs. S distribution for the events in the m_{ES} sideband of the data sample.

4.3.2 Characterization of the PDFs

The one-dimensional PDFs are mainly determined from data. Inputs from Monte Carlo simulations have been used only if a good agreement between data and simulations has been verified.

$f_{\pi}(\Delta E_{\pi})$ and $f_K(\Delta E_K)$ PDFs

The $f_{\pi}(\Delta E_{\pi})$ and $f_K(\Delta E_K)$ PDFs are the ΔE resolution functions for the signal components (see Fig. 4.6). They are parameterized with the sum of two Gaussians:

$$f_{\pi,K}(x) = \frac{r}{\sqrt{2\pi}\sigma_n}\, e^{-(x-m_n)^2/2(\sigma_n)^2} \;+\; \frac{1-r}{\sqrt{2\pi}\sigma_l}\, e^{-(x-m_l)^2/2(\sigma_l)^2}\;. \qquad (4.14)$$

The mean value m_n and the width σ_n of the core Gaussian are allowed to float as free parameters in the likelihood fit.

A fit to the distribution in ΔE_K for simulated $B^{\pm} \to J/\psi\,K^{\pm}$ events (see Fig. 4.14) has been used to estimate the following parameters:

1. the difference $m_l - m_n$ between the mean values of the core and tail Gaussians;

2. the ratio σ_l/σ_n between the widths of the core and tail Gaussians;

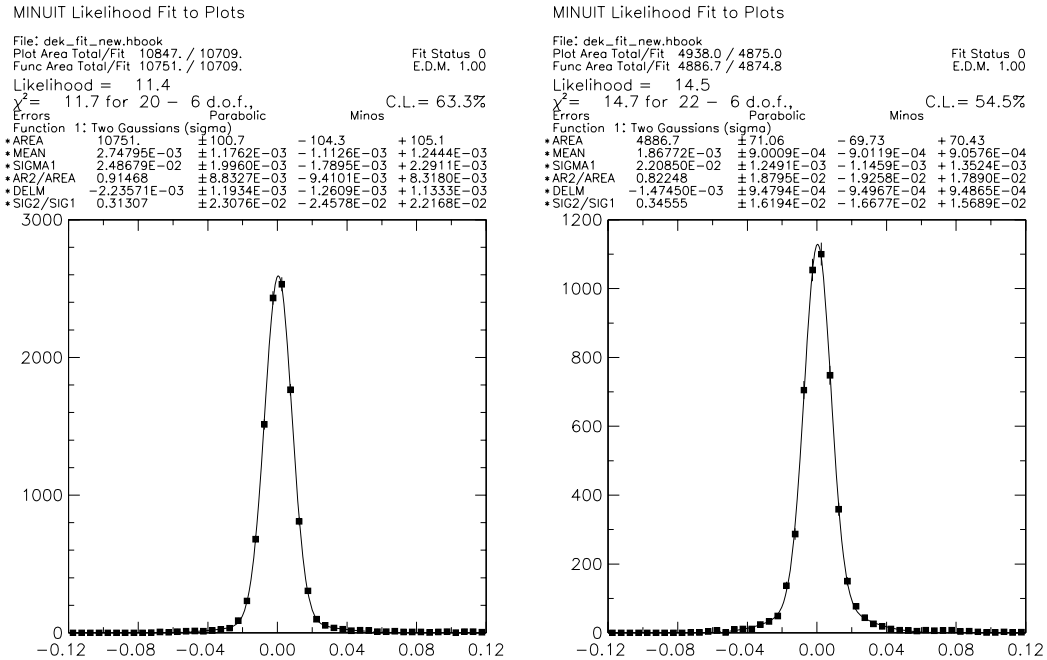

Figure 4.14: The fit to the distribution in ΔE_K for simulated $J/\psi(\to \mu^+\mu^-)K^\pm$ (left plot) and $J/\psi(\to e^+e^-)K^\pm$ (right plot) events.

3. the fraction r of the events under the core Gaussian.

We use different parameters for $J/\psi(\to \mu^+\mu^-)h^\pm$ and $J/\psi(\to e^+e^-)h^\pm$ events. Their values are reported in Table 4.5. Finally, we constrain $f_\pi = f_K$ in the fit.

$h_\pi(m_{ES})$ and $h_K(m_{ES})$ PDFs

The $h_\pi(m_{ES})$ and $h_K(m_{ES})$ PDFs are the m_{ES} resolution functions for the signals (see Fig. 4.7). They are parameterized with a single Gaussians:

$$h_{\pi,K}(x) = \frac{1}{\sqrt{2\pi}\sigma_M}\, e^{-(x-M)^2/2(\sigma_M)^2} \tag{4.15}$$

The mean value M and the width σ_M are allowed to float as free parameters in the likelihood fit. We allow for different parameters for $J/\psi(\to \mu^+\mu^-)h^\pm$ and $J/\psi(\to e^+e^-)h^\pm$ events. Furthermore,, we constrain $h_\pi = h_K$ in the fit.

Table 4.5: Values of the fixed parameters in the f_π and f_K PDFs.

	$m_l - m_n$ (MeV)	σ_l/σ_n	r
$J/\psi\,(\to \mu^+\mu^-)h^\pm$	2.2 ± 1.2	3.19 ± 0.24	0.915 ± 0.009
$J/\psi\,(\to e^+e^-)h^\pm$	1.47 ± 0.95	2.89 ± 0.14	0.822 ± 0.019

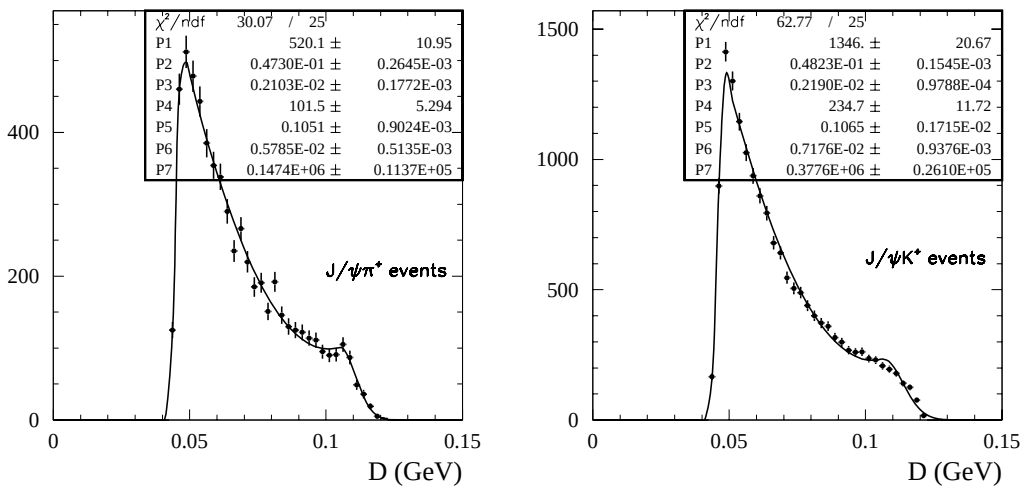

Figure 4.15: The D distributions and fit for simulated $B^\pm \to J/\psi\,\pi^\pm$ (left plot) and $B^\pm \to J/\psi\,K^\pm$ (right plot) events.

$g_\pi(D)$ and $g_K(D)$ PDFs

The $g_\pi(D)$ and $g_K(D)$ PDFs are each represented by a phenomenological function determined from the distributions of simulated $B^\pm \to J/\psi\,\pi^\pm$ and $B^\pm \to J/\psi\,K^\pm$ events. We fit each distribution with a second-order approximation to an exponential function, closed at each edge by half of a Gaussian function (see Fig. 4.15):

$$g_{\pi,K}(x) = \begin{cases} p_1\, e^{-(x-p_2)^2/2(p_3)^2} & \text{if } x < p_2 \\ p_1 + \frac{(p_4-p_1)(x-p_2)}{p_5-p_2} + (x-p_2)(x-p_5)p_7 & \text{if } p_2 < x < p_5 \\ p_4\, e^{-(x-p_5)^2/2(p_6)^2} & \text{if } x > p_5 \end{cases}$$

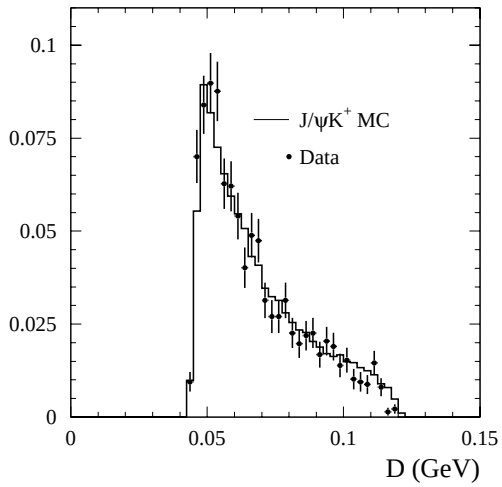

Figure 4.16: The D distribution for $B^{\pm} \to J/\psi K^{\pm}$ events in data and in Monte Carlo simulations. The $B^{\pm} \to J/\psi K^{\pm}$ events in the data sample have been selected applying tight requirements on ΔE_K and m_{ES}: $|\Delta E_K| < 50\,\mathrm{MeV}$, $m_{ES} > 5.27\,\mathrm{GeV}/c^2$. The distributions are normalized to one.

Figure 4.16 shows that the Monte Carlo simulation reproduces the data. Furthermore, there are no significant discrepancies between the distributions for $B^{\pm} \to J/\psi(\to \mu^+\mu^-)h^{\pm}$ and $B^{\pm} \to J/\psi(\to e^+e^-)h^{\pm}$ events (see Fig. 4.17), therefore a unique PDF is used in the two cases.

$f_{bkd}(S)$ and $g_{bkd}(D)$ PDFs

The $f_{bkd}(S)$ and $g_{bkd}(D)$ PDFs are each represented by a phenomenological function determined from the distribution of the events in the m_{ES} sideband. We fit the S distribution with a product of a Gaussian and a fifth-order polynomial function (see Fig. 4.18-left plot):

$$f_{bkd}(x) = e^{-(x-p_1)^2/2(p_2)^2}\left(p_3 + p_4 x + p_5 x^2 + p_6 x^3 + p_7 x^4 + p_8 x^5\right). \qquad (4.16)$$

We fit the D distribution with a phenomenological function of the same form as for the g_π and g_K PDFs (see Fig. 4.18-right plot).

There are no significant discrepancies between the distributions for $B^{\pm} \to J/\psi(\to \mu^+\mu^-)h^{\pm}$ and $B^{\pm} \to J/\psi(\to e^+e^-)h^{\pm}$ events (see Fig. 4.19), therefore a unique PDF is used in the two cases.

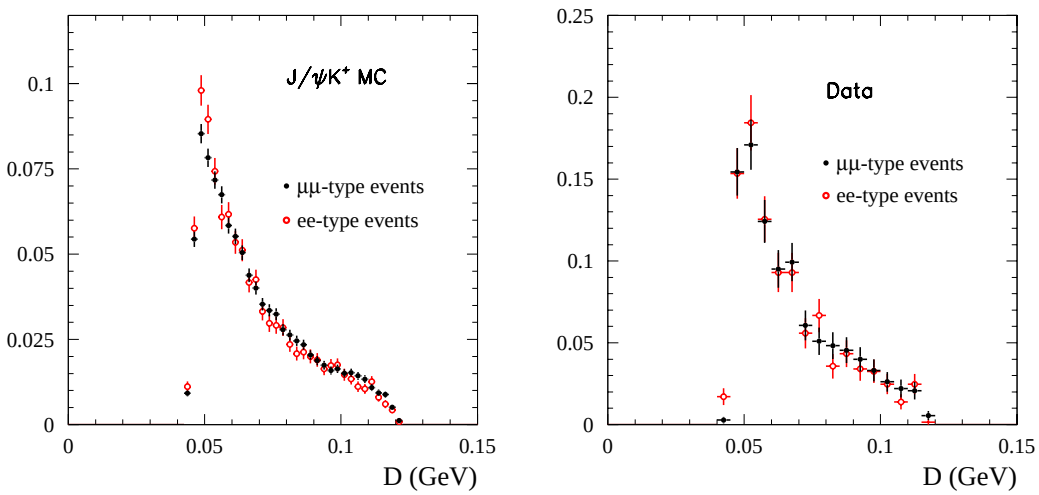

Figure 4.17: The D distributions for $J/\psi(\to \mu^+\mu^-)K^\pm$ and $J/\psi(\to e^+e^-)K^\pm$ events as obtained from Monte Carlo simulations (left plot) and from $B^\pm \to J/\psi\,K^\pm$ events in data (right plot). The $B^\pm \to J/\psi\,K^\pm$ events in the data sample have been selected applying tight requirements on ΔE_K and m_{ES}: $|\Delta E_K| < 50\,\mathrm{MeV}$, $m_{ES} > 5.27\,\mathrm{GeV}/c^2$. The distributions are normalized to one.

Table 4.6: Values of the parameters in the h_{bkd} PDF.

ζ_1	ζ_2	M_{pk} (GeV/c^2)	σ_{pk} (MeV/c^2)
3200 ± 1100	-35 ± 16	5.2801 ± 0.0013	3.86 ± 0.90

$h_{bkd}(m_{ES})$ PDF

The $h_{bkd}(m_{ES})$ PDF is determined from the distribution in m_{ES} of the events in the ΔE_π and ΔE_K sidebands. We fit the distribution with the sum of an ARGUS and a Gaussian function (see Fig. 4.20):

$$\begin{aligned} h_{bkd}(x) &= (1-R)\left[\zeta_1\, x\,\sqrt{1-(x/e_b)^2}\, e^{\zeta_2[1-(x/e_b)^2]}\right] + \\ &+ R\, e^{-(x-M_{pk})^2/2(\sigma_{pk})^2} \qquad (e_b = 5.29)\,. \end{aligned} \tag{4.17}$$

The values of the fitted parameters are reported in Table 4.6.

There are no significant discrepancies between the distributions for $B^\pm \to J/\psi(\to \mu^+\mu^-)h^\pm$ and $B^\pm \to J/\psi(\to e^+e^-)h^\pm$ events (see Fig. 4.21), therefore a unique PDF is used in the two cases.

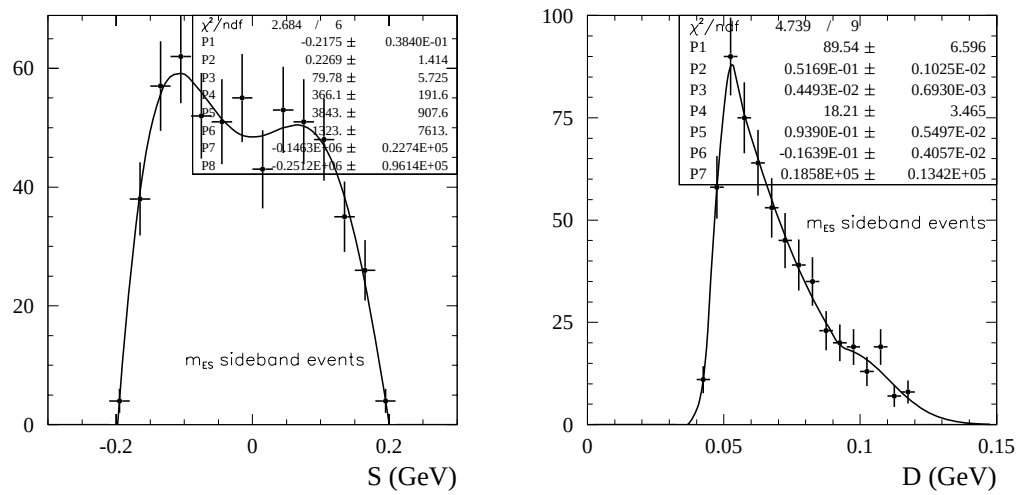

Figure 4.18: The S (left plot) and D (right plot) distributions and fit for the events in the m_{ES} sideband.

In order to estimate the number of events described by the Gaussian peak in the data sample, we have considered Monte Carlo simulations of the following events: continuum $q\overline{q}$ ($q = u, d, s, c$), generic $b\overline{b}$ (with the $B \to J/\psi X$ component subtracted), and inclusive J/ψ (with the $B^{\pm} \to J/\psi \pi^{\pm}$ and $B^{\pm} \to J/\psi K^{\pm}$ components subtracted). The events that pass the same selection of the data sample are distributed in m_{ES} as in Figures 4.22 - 4.23. Summarizing:

1. The h_{bkd} PDF is described by the sum of an ARGUS and a Gaussian function. The ARGUS function describes the background from generic $b\overline{b}$ and continuum events, and the not-peaking component of inclusive J/ψ background. The Gaussian function describes the peaking component of the inclusive J/ψ background.

2. The number N_{pk} of peaking background events in the data sample is estimated as the area of the Gaussian in Fig. 4.23, scaled to a luminosity of $20.7\,\mathrm{fb}^{-1}$. We obtain $N_{pk} = 10.3 \pm 3.9$.

3. The number N_{AR} of background events in the data sample described by the ARGUS function is estimated integrating the ARGUS function in the fit of Fig. 4.10. We obtain $N_{AR} = 753 \pm 27$; the number of events in the m_{ES} signal region ($m_{ES} > 5.27\,\mathrm{GeV}/c^2$) is $N'_{AR} = 107 \pm 10$.

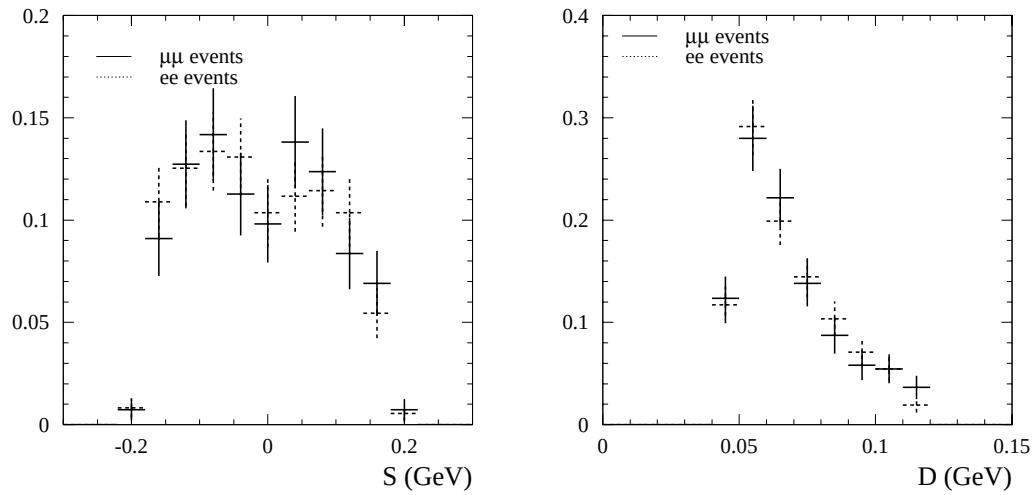

Figure 4.19: The S (left plot) and D (right plot) distributions for $J/\psi\,(\to \mu^+\mu^-)h^{\pm}$ and $J/\psi\,(\to e^+e^-)h^{\pm}$ events in the m_{ES} sideband. The distributions are normalized to one.

4. The parameter R in the h_{bkd} PDF is estimated as:

$$R = \frac{N_{pk}}{N_{AR} + N_{pk}}\,, \tag{4.18}$$

obtaining:

$$R = 0.0135 \pm 0.0052\,. \tag{4.19}$$

4.3.3 Summary of the fit strategy

Table 4.7 summarizes the parameters in the PDFs and whether their value has been fixed in the maximum likelihood fit. In this case we also indicate the sample used to estimate them.

In the maximum likelihood fit:

1. we constrain $f_{\pi} = f_K$ and $h_{\pi} = h_K$;

2. mean values and widths of $f_{\pi,K}$ and $h_{\pi,K}$ are left free;

3. $f_{\pi,K}$ and $h_{\pi,K}$ use different parameters for $J/\psi\,(\to \mu^+\mu^-)h^{\pm}$ and $J/\psi\,(\to e^+e^-)h^{\pm}$ events.

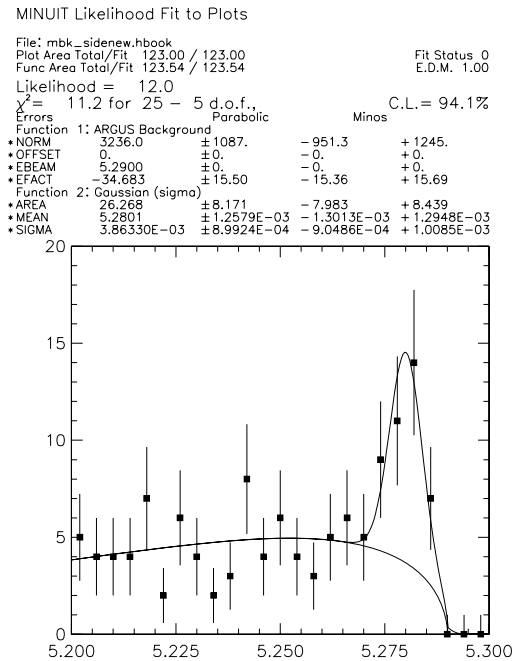

Figure 4.20: The m_{ES} distribution and fit for the events in the ΔE_π and ΔE_K sidebands.

The $B^\pm \to J/\psi(\to \mu^+\mu^-)h^\pm$ and $B^\pm \to J/\psi(\to e^+e^-)h^\pm$ samples are fitted separately. The parameters extracted from the likelihood fit are summarized in Table 4.8.

4.4 Fit results

Table 4.9 shows the yields and the values of the parameters extracted from the fit. The correlation coefficient $\rho_{\pi K}$ between N_π and N_K, the confidence level of the fit (C.L.), and the statistical significance of the $B^\pm \to J/\psi\pi^\pm$ signal are also reported.

In order to estimate the confidence level, we have performed the fit on 5000 simulated $J/\psi(\to \mu^+\mu^-)h^\pm$ and 5000 simulated $J/\psi(\to e^+e^-)h^\pm$ samples. The number of $J/\psi\pi^\pm$, $J/\psi K^\pm$, and background events in each sample is extracted from Poissonian distributions, having the measured yields as mean. The values of $(\Delta E_\pi, \Delta E_K, m_{ES})$ for each event are extracted from the PDFs used in the likelihood fit. For each sample we have evaluated $-\ln\max(L)$,

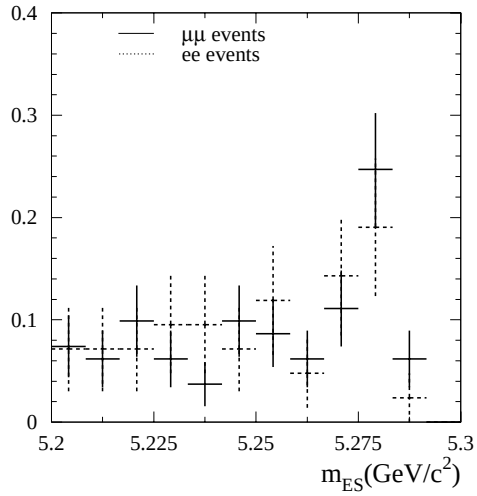

Figure 4.21: The m_{ES} distributions for $J/\psi\,(\to \mu^+\mu^-)h^\pm$ and $J/\psi\,(\to e^+e^-)h^\pm$ events in the ΔE_π and ΔE_K sidebands. The distributions are normalized to one.

which is distributed as in Fig. 4.24. We compute the confidence level as the fraction of events with $-\ln\max(L)$ greater than the value observed for the data sample.

The statistical significance of the $B^\pm \to J/\psi\,\pi^\pm$ signal is evaluated (with a Gaussian approximation for the likelihood) as the change in the maximum value of L when we constrain $N_\pi = 0$.

4.4.1 Tests of the fit

Possible biases in the fitting procedure are investigated by performing the fit on simulated samples of known composition. We have considered a mix of simulated $B^\pm \to J/\psi\,\pi^\pm$, $B^\pm \to J/\psi\,K^\pm$, and background events that have passed the same selection of the data sample. The yields determined with the likelihood fit are then compared with the composition of the sample.

Table 4.10 summarizes the results of the fit to a simulated sample in which the background component is selected from continuum $q\overline{q}$ ($q = u, d, s, c$), and generic $b\overline{b}$ (with the $B \to J/\psi\,X$ component subtracted) events. The extracted yields reproduce the sample composition.

Table 4.11 summarizes the results of the fit to three simulated samples in which the background component is selected from inclusive J/ψ events (with

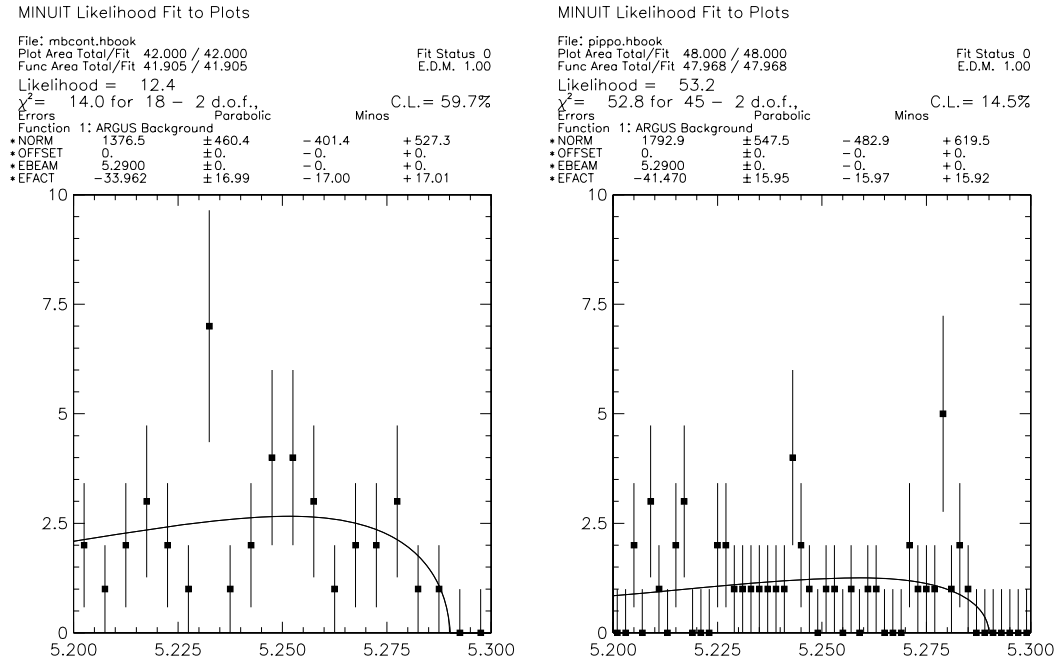

Figure 4.22: (left plot): The m_{ES} distribution for simulated continuum $q\overline{q}$ events (more than 3 million generated events) passing the same selection of the data sample; the distribution has been fitted with an ARGUS function. (right plot): The m_{ES} distribution for simulated generic $b\overline{b}$ events (more than 4.6 million generated events) passing the same selection of the data sample; the $B \to J/\psi X$ component has been subtracted. The distribution has been fitted with an ARGUS function.

the signal components removed). Each sample corresponds to an equivalent luminosity of $84.5\,\mathrm{fb}^{-1}$, and the ratio between the $J/\psi\,\pi^{\pm}$ and $J/\psi\,K^{\pm}$ components is about 5%. The average values of the extracted yields, and their differences Δ with the known compositions are also reported. These differences are consistent with 0 within the error.

4.4.2 Ratio of branching fractions

From the tests on simulated samples we have seen no evidence of bias in the fitting procedure. However, because of the limited statistics of the simulated samples, we correct the yields for the small observed deviations (scaled to 20.7 fb^{-1}) in Table 4.11. The original and the corrected yields (N_i^{eff}) are compared in Table 4.12.

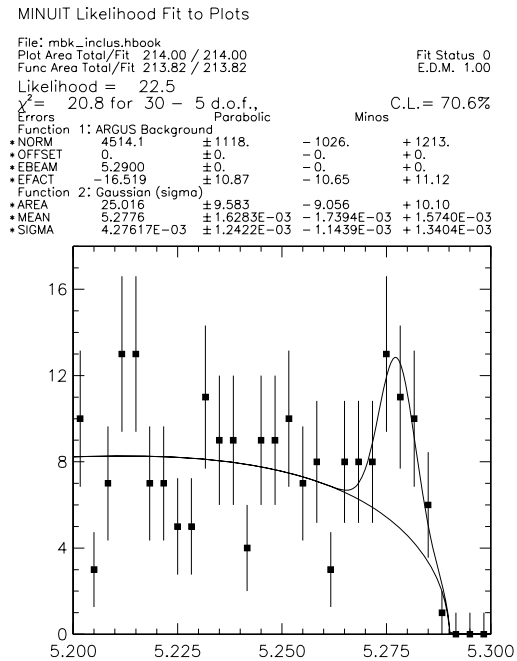

Figure 4.23: The m_{ES} distribution for simulated inclusive J/ψ events (for an equivalent luminosity of $50.46\,\mathrm{fb}^{-1}$) passing the same selection defining the data sample. The $B^\pm \to J/\psi\,\pi^\pm$ and $B^\pm \to J/\psi\,K^\pm$ components have been subtracted. The distribution has been fitted with the sum of an ARGUS and a Gaussian function.

The ratio of branching fractions has been determined as:

$$\frac{\mathcal{B}(B^\pm \to J/\psi\,\pi^\pm)}{\mathcal{B}(B^\pm \to J/\psi\,K^\pm)} = \frac{N_\pi^{eff}}{N_K^{eff}}\,, \tag{4.20}$$

obtaining, separately for the $J/\psi\,(\to \mu^+\mu^-)h^\pm$ and the $J/\psi\,(\to e^+e^-)h^\pm$ samples:

$$\left[\frac{\mathcal{B}(B^\pm \to J/\psi\,\pi^\pm)}{\mathcal{B}(B^\pm \to J/\psi\,K^\pm)}\right]_{J/\psi\to\mu^+\mu^-} = (4.2 \pm 1.0)\% \tag{4.21}$$

$$\left[\frac{\mathcal{B}(B^\pm \to J/\psi\,\pi^\pm)}{\mathcal{B}(B^\pm \to J/\psi\,K^\pm)}\right]_{J/\psi\to e^+e^-} = (3.5 \pm 1.2)\%\,. \tag{4.22}$$

Performing the fit to the entire data sample of 2155 events we obtain the

Table 4.7: Summary of the PDFs parameters.

PDF	# of param.	parameters	fixed/free	sample
$f_{\pi,K}$	5	m_n, σ_n	free	
		$m_l - m_n$, σ_l/σ_n	fixed	MC
		r	fixed	MC
$g_{\pi,K}$	7	$p_1 \dots p_7$	fixed	MC
$h_{\pi,K}$	2	M, σ_M	free	
f_{bkd}	8	$p_1 \dots p_8$	fixed	m_{ES} sideband
g_{bkd}	7	$p_1 \dots p_7$	fixed	m_{ES} sideband
h_{bkd}	5	ζ_1, ζ_2	fixed	ΔE_π & ΔE_K sidebands
		m_{pk}, σ_{pk}	fixed	ΔE_π & ΔE_K sidebands
		R	fixed	$J/\psi X$ MC

Table 4.8: Quantities extracted from the likelihood fit.

Parameters	#
N_i	3
m_n, σ_n	2
M, σ_M	2
TOT.	7

total yields:

$$\begin{aligned} N_\pi &= 52 \pm 10 \\ N_K &= 1284 \pm 37 \\ N_{bkd} &= 819 \pm 31\,. \end{aligned}$$

The distribution of $\ln(P_\pi/P_K)$ for the data sample, after subtraction of the background component in each bin, is shown in Fig. 4.25. The background distribution is obtained from the m_{ES} sideband and is normalized to the background yield. The distribution of $\ln(P_\pi/P_K)$ for simulated signal samples, normalized to the yields extracted from the likelihood fit, is also shown. The distribution in m_{ES} for the events in the data sample with $\ln(P_\pi/P_K) > 0$ can be seen in Fig. 4.26. The likelihood fit predictions for all components, and for $J/\psi\,\pi^\pm$ and $J/\psi\,K^\pm$ separately, are also shown. Fig. 4.27

Table 4.9: The results of the fit to the data sample.

	$J/\psi\,(\to \mu^+\mu^-)h^\pm$	$J/\psi\,(\to e^+e^-)h^\pm$
N_π	29.5 ± 6.9	21.9 ± 7.4
N_K	685 ± 27	601 ± 26
N_{bkd}	360 ± 20	458 ± 23
m_n (MeV)	-1.4 ± 0.4	-1.2 ± 0.6
σ_n (MeV)	9.8 ± 0.3	11.5 ± 0.5
M (GeV/c^2)	5.2798 ± 0.0001	5.2799 ± 0.0001
σ_M (MeV/c^2)	2.40 ± 0.07	2.75 ± 0.09
$\rho_{\pi K}$	-0.025	-0.070
C.L.	53.0%	59.5%
stat. signif.	6.3σ	3.7σ

Table 4.10: Test of the fit to a simulated sample of known composition. The background sample is selected from continuum and generic $b\overline{b}$ events.

		N_π	N_K	N_{bkd}
$J/\psi\,(\to \mu^+\mu^-)h^\pm$	expected	30	600	149
	fit	28.5 ± 5.9	589 ± 24	162 ± 13
$J/\psi\,(\to e^+e^-)h^\pm$	expected	30	600	115
	fit	32.1 ± 6.3	582 ± 24	131 ± 12

shows the likelihood fit results superimposed to the distribution in ΔE_π for the events in the m_{ES} signal region ($m_{ES} > 5.27\,\mathrm{GeV}/c^2$). The ΔE_π PDFs in the $J/\psi\,K^\pm$ and background hypotheses have been obtained with a numerical integration of the P_i PDFs:

$$p_K(\Delta E_\pi) = \int f_K(x) g_K(x - \Delta E_\pi)\,\mathrm{d}x \tag{4.23}$$

$$p_{bkd}(\Delta E_\pi) = \int f_{bkd}(x + \Delta E_\pi) g_{bkd}(x - \Delta E_\pi)\,\mathrm{d}x\,. \tag{4.24}$$

The ratio of branching fractions is determined from the total yields, corrected for the small deviations Δ_π and Δ_K estimated in section 4.4.1 and reported in Table 4.13. We finally obtain:

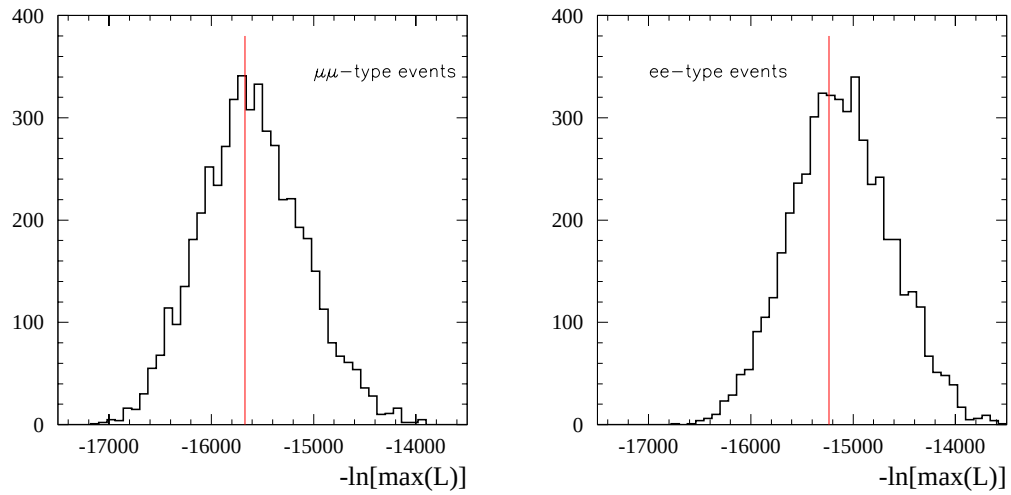

Figure 4.24: The distribution of the $-\ln\max(L)$ for 5000 simulated $J/\psi(\to \mu^+\mu^-)h^\pm$ (left plot) and $J/\psi(\to e^+e^-)h^\pm$ (right plot) simulated samples. The vertical line marks the value of the $-\ln\max(L)$ for the data sample.

$$\frac{\mathcal{B}(B^\pm \to J/\psi\,\pi^\pm)}{\mathcal{B}(B^\pm \to J/\psi\,K^\pm)} = (3.91 \pm 0.78)\%\,, \tag{4.25}$$

where the error is statistical only.

4.5 Use of particle identification

The use of particle identification for the charged hadron $h^\pm$ has been investigated by adding to the likelihood, as an additional argument, the Cherenkov angle θ_C measured in the DIRC for this track. Figure 4.28 shows the distribution of $B^\pm \to J/\psi\,h^\pm$ events ($h = \pi, K$) in the (θ_C, p_h) plane; the distribution of the difference between the measured and the expected Cherenkov angle for kaons from $B^\pm \to J/\psi\,K^\pm$ events is also shown.

The particle identification (PID) information allowes us to split the background events into background with a pion as a final state charged hadron, and background with a kaon as a final state charged hadron. The yields of these two components are denoted as $N_{bkd\pi}$ and N_{bkdK}.

Table 4.11: Test of the fit to simulated samples of known composition. The background component is selected from simulated inclusive J/ψ events.

		N_π	N_K
$J/\psi \to \mu^+\mu^-$	expected	133	2652
	fit sample 1	141 ± 13	2614 ± 52
	fit sample 2	129 ± 12	2633 ± 52
	fit sample 3	134 ± 13	2622 ± 52
	average	134.7 ± 7.5	2623 ± 30
	Δ (84.5 fb^{-1})	1.7 ± 7.5	-29 ± 30
	Δ (20.7 fb^{-1})	0.4 ± 1.8	-7.1 ± 7.3
$J/\psi \to e^+e^-$	expected	60	1207
	fit sample 1	56.3 ± 8.8	1195 ± 35
	fit sample 2	68.3 ± 9.4	1197 ± 35
	fit sample 3	63.2 ± 9.0	1177 ± 35
	average	62.9 ± 5.2	11900 ± 20
	Δ (84.5 fb^{-1})	2.9 ± 5.2	-17 ± 20
	Δ (20.7 fb^{-1})	0.7 ± 1.3	-4.2 ± 4.9

4.5.1 Likelihood function

The modified likelihood function including the PID information has the following form:

$$L'(N_i) = e^{-N} \times \prod_{j=1}^{M} \sum_{i} P'_i(\Delta E^j_\pi, \Delta E^j_K, {m_{ES}}^j, \theta^j_C)\, N_i \,, \tag{4.26}$$

where $i = \pi, K, bkd\pi, bkdK$. We factorize the P'_i PDFs as:

$$P'_i(\Delta E_\pi, \Delta E_K, m_{ES}, \theta_C) = P_i(\Delta E_\pi, \Delta E_K, m_{ES}) \cdot t_i(\theta_C) \,, \tag{4.27}$$

where $t_i(\theta_C)$ are the one-dimensional PDFs for the θ_C variable and the P_i are the kinematical PDFs used in the previous fit. We have assumed:

$$P_{bkd\pi} = P_{bkdK} = P_{bkd} \,, \tag{4.28}$$

which has been verified with the events in the sidebands. They are classified as "pion-like" and "kaon-like" events according to the θ_C of the final state

Table 4.12: Original (N_i) and corrected yields (N_i^{eff}) for the signal components.

sample	i	N_i	N_i^{eff}
$J/\psi\,(\to \mu^+\mu^-)h^\pm$	π	29.6 ± 6.9	29.1 ± 6.9
	K	685 ± 27	692 ± 27
$J/\psi\,(\to e^+e^-)h^\pm$	π	21.9 ± 7.4	21.2 ± 7.4
	K	601 ± 26	605 ± 26

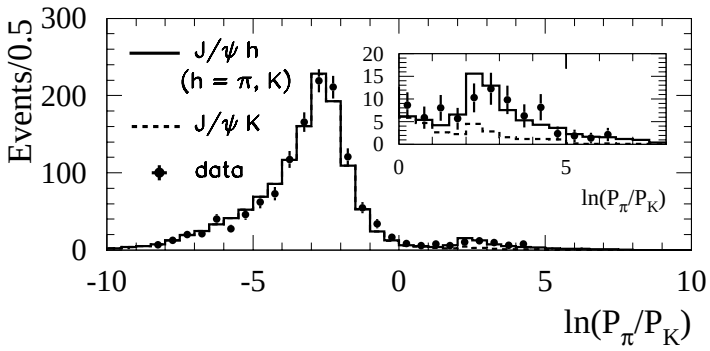

Figure 4.25: The $\ln(P_\pi/P_K)$ distribution for events in the data sample (after the subtraction of the background component in each bin) and from Monte Carlo simulations of $J/\psi\,\pi^\pm$ and $J/\psi\,K^\pm$ events; the distributions are normalized to the yields extracted from the maximum likelihood fit.

charged hadron:

$$|\theta_C - \theta_{C,\pi}| < 0.01 \quad \to \quad \text{pion-like event} \tag{4.29}$$

$$|\theta_C - \theta_{C,K}| < 0.01 \quad \to \quad \text{kaon-like event ,} \tag{4.30}$$

where $\theta_{C,\pi}$ and $\theta_{C,K}$ are the expected values of the Cherenkov angle in the pion and kaon hypothesis respectively. Figure 4.29 shows the comparison between the distributions in D for "pion-like" and "kaon-like" background events; the comparison between the S distributions is also shown. Figure 4.30 shows the comparison between the distributions in m_{ES} for "pion-like" and "kaon-like" background events.

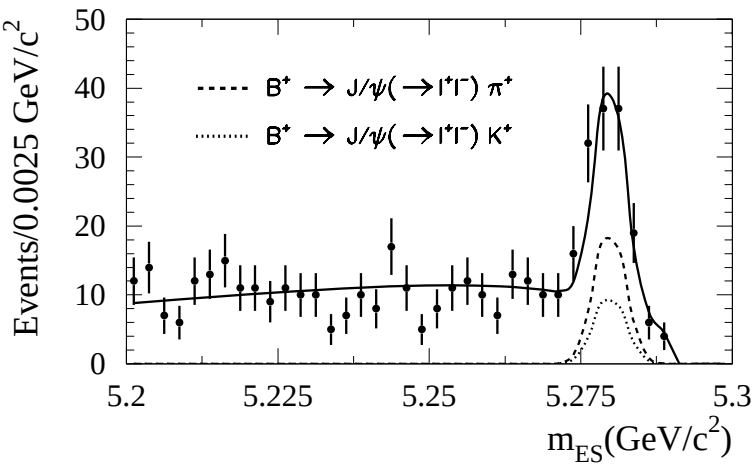

Figure 4.26: The m_{ES} distribution for events with $\ln(P_\pi/P_K) > 0$ compared with the fit result (solid curve); the dashed and dotted curves represent the fitted contributions from the $J/\psi\,\pi^{\pm}$ and the $J/\psi\,K^{\pm}$ components.

Table 4.13: Original yield N_i, correction Δ_i and corrected yield N_i^{eff} for the signal components.

i	N_i	Δ_i	N_i^{eff}
π	52 ± 10	1.1 ± 2.2	51 ± 10
K	1284 ± 37	-11.3 ± 8.8	1296 ± 38

4.5.2 Characterization of the θ_C PDFs

The PDFs for the variable θ_C are determined from the distributions for pions and kaons in $D^{*+} \to D^0\pi^+$, $D^0 \to K^-\pi^+$ decays. The PDFs are parameterized as Gaussian functions with mean values and widths that depend on the momentum of the track:

$$t_\pi(\theta_C) = t_{bkd\pi}(\theta_C) = \frac{1}{\sqrt{2\pi}\sigma_\pi(p)}\, e^{-(\theta_C - \theta^m_{C,\pi}(p))^2/2(\sigma_\pi(p))^2} \tag{4.31}$$

$$t_K(\theta_C) = t_{bkdK}(\theta_C) = \frac{1}{\sqrt{2\pi}\sigma_K(p)}\, e^{-(\theta_C - \theta^m_{C,K}(p))^2/2(\sigma_K(p))^2}\,. \tag{4.32}$$

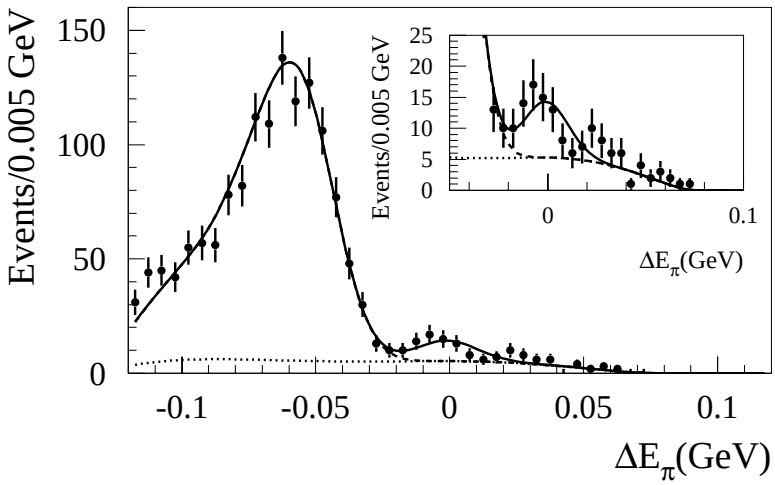

Figure 4.27: The ΔE_π distribution for events with $m_{ES} > 5.27\,\mathrm{GeV}/c^2$ compared with the fit result (solid curve). The dotted curve represents the fitted contribution from the background alone, while the dashed curve represents the fitted contribution from the sum of background and $J/\psi K^\pm$ components.

The mean values are parameterized as:

$$\theta^m_{C,\pi}(p) = \theta_{C,\pi} + \theta^{off}_{C,\pi}(p) \tag{4.33}$$
$$\theta^{off}_{C,\pi}(p) = p_{0,\pi} + p_{1,\pi} \cdot p + p_{2,\pi} \cdot p^2 \tag{4.34}$$

$$\theta^m_{C,K}(p) = \theta_{C,K} + \theta^{off}_{C,K}(p) \tag{4.35}$$
$$\theta^{off}_{C,K}(p) = p_{0,K} + p_{1,K} \cdot p + p_{2,K} \cdot p^2 \,, \tag{4.36}$$

where $\theta_{C,\pi}$, $\theta_{C,K}$ are the expected values of the Cherenkov angle, and $\theta^{off}_{C,\pi}(p)$, $\theta^{off}_{C,K}(p)$ are empirical offsets. The widths are parameterized as:

$$\sigma_\pi(p) = s_{0,\pi} + s_{1,\pi} \cdot p + s_{2,\pi} \cdot p^2 \tag{4.37}$$
$$\sigma_K(p) = s_{0,K} + s_{1,K} \cdot p + s_{2,K} \cdot p^2 \,. \tag{4.38}$$

Table 4.14 summarizes the values of the parameters.

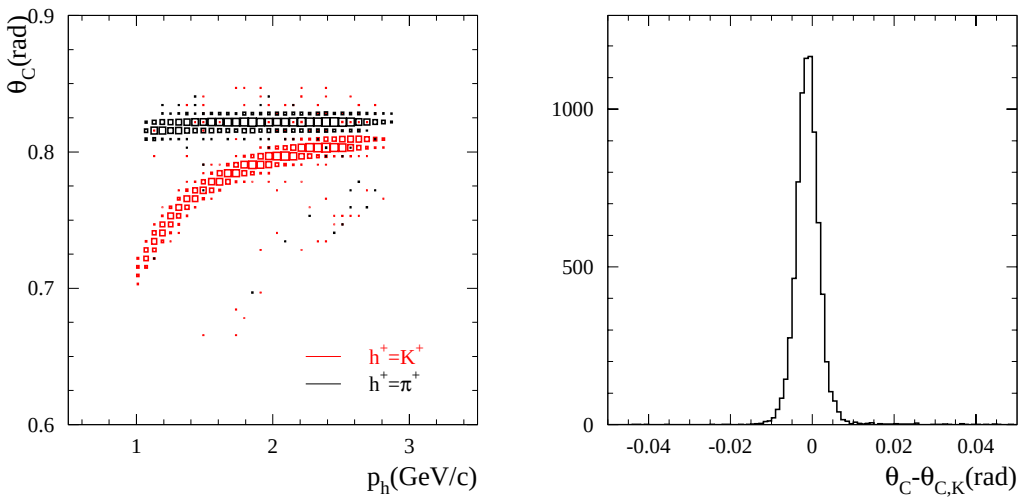

Figure 4.28: (left plot): The Cherenkov angle vs. momentum distribution for the final state charged hadron in $B^\pm \to J/\psi\,\pi^\pm$ and $B^\pm \to J/\psi\,K^\pm$ simulated events. (right plot): The difference between the measured and expected Cherenkov angles for a kaon in $B^\pm \to J/\psi\,K^\pm$ simulated events. The expected value has been computed according to the momentum of the track and in the kaon mass hypothesis.

4.5.3 Likelihood fit results

The fit with the modified likelihood function is performed to a restricted sample of events. Indeed we consider only tracks in a fiducial region defined by the angular acceptance of the DIRC ($0.45 < \theta_h < 2.5\,rad$) and for which the Cherenkov angle is available ($\theta_C > 0$). In addition we require that the DIRC signal is very well separated from the noise: $n_\gamma - n_\gamma^{bkd} > 10$, where n_γ is the number of collected photons. Finally, we require that the measured Cherenkov angle is not compatible with the angle expected for a proton ($|\theta_C - \theta_{C,p}| > 2 \times \sigma_{\theta_C}$, where σ_{θ_C} is the Cherenkov angle resolution). Table 4.15 summarizes the efficiencies of the above requirements, as estimated with kaons and pions from D^* decays. It is evident that the requirement on the number of collected photons has a different efficiency for pions and kaons.

The fit has been performed separately on the 697 $B^\pm \to J/\psi\,(\to \mu^+\mu^-)h^\pm$ and the 680 $B^\pm \to J/\psi\,(\to e^+e^-)h^\pm$ candidates of the data sample. Table 4.16 shows the fitted yields. The tests performed with simulated samples of known composition give deviations from the expected yields that are consistent with 0. However, because of the limited statistics of the simulated samples, we

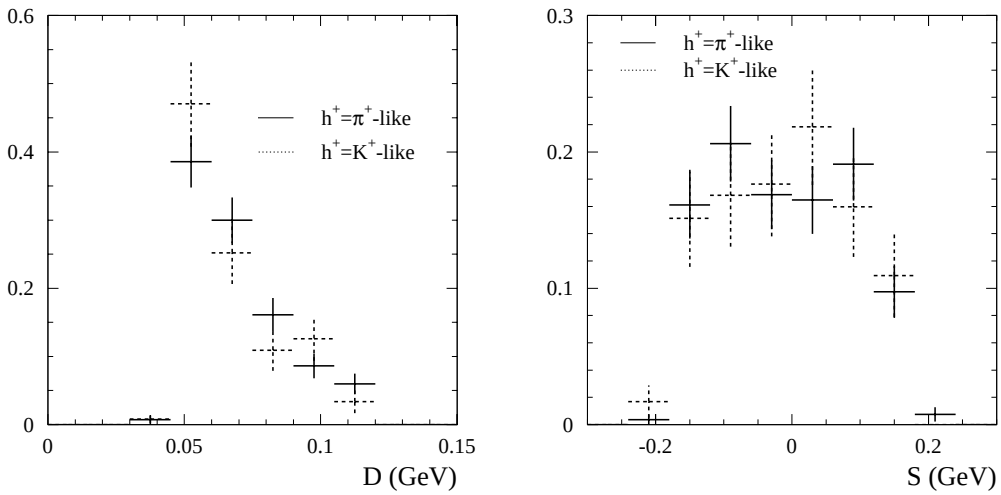

Figure 4.29: (left plot): The D distributions for "pion-like" and "kaon-like" events in the m_{ES} sideband. (right plot): The S distributions for "pion-like" and "kaon-like" events in the m_{ES} sideband.

correct the fitted yields for the small observed deviations. The original and the corrected yields (N_i^{eff}) are compared in Table 4.17.

4.5.4 Ratio of branching fractions

The ratio of branching fractions has been determined as:

$$\frac{\mathcal{B}(B^{\pm} \to J/\psi\,\pi^{\pm})}{\mathcal{B}(B^{\pm} \to J/\psi\,K^{\pm})} = \frac{N_{\pi}^{eff}}{N_{K}^{eff}} \times \frac{\epsilon_K(n_\gamma)}{\epsilon_\pi(n_\gamma)}\,. \tag{4.39}$$

In the above equation $\epsilon_K(n_\gamma)$ and $\epsilon_\pi(n_\gamma)$ represent the efficiencies of the requirements on the number of collected photons in the DIRC (reported in Table 4.15). The result can be compared with the measurement obtained without the use of the PID information (see Table 4.18). We obtain that the addition of particle identification does not significantly change the statistical precision of the results. Estimating the error on the difference Δ between the measurements as $\sigma_\Delta = \sqrt{|\sigma_1^2 - \sigma_2^2|}$ we obtain a combined discrepancy of 1.6σ.

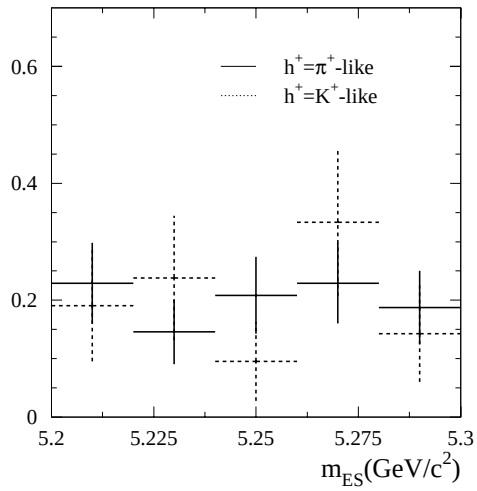

Figure 4.30: The m_{ES} distributions for "pion-like" and "kaon-like" events in both the ΔE_K and ΔE_π sidebands.

4.6 Systematic uncertainties

4.6.1 PDFs parameterizations

The uncertainties on the fixed parameters of the PDFs represent a source of systematic error on the observed yields N_π and N_K. Since:

$$\frac{\mathcal{B}(B^{\pm} \to J/\psi\,\pi^{\pm})}{\mathcal{B}(B^{\pm} \to J/\psi\,K^{\pm})} = \frac{N_\pi - \Delta_\pi}{N_K - \Delta_K}\,, \tag{4.40}$$

where Δ_π and Δ_K are the applied corrections to the fitted yields, the systematic error on N_π and N_K affects also the ratio of branching fractions measurement.

We have varied each of these parameters by $\pm 1\sigma$, and have repeated the likelihood fit. For each PDF, the standard deviation of the new results with respect to the observed yields is assumed as a contribution to the systematic uncertainty on N_π and N_K. The contributions due to the parameter r (fraction of the events under the core Gaussian of the signal) and R (fraction of the peaking background events) are estimated separately.

The several contributions have been quadratically added to give the total systematic errors on the yields N_π and N_K. Propagating these errors, we obtain a contribution of 0.0007 to the systematic error on the ratio of branching

Table 4.14: Values of the parameters used in the $t_i(\theta_C)$ PDFs (for momenta measured in GeV/c and θ_C in *mrad*.)

$p_{0,\pi}$	$p_{1,\pi}$	$p_{2,\pi}$
0.4823 ± 0.20	-0.6917 ± 0.19	0.1224 ± 0.042
$s_{0,\pi}$	$s_{1,\pi}$	$s_{2,\pi}$
5.670 ± 0.18	-1.638 ± 0.17	0.2504 ± 0.037
$p_{0,K}$	$p_{1,K}$	$p_{2,K}$
-2.02 ± 0.19	1.237 ± 0.17	-0.2029 ± 0.037
$s_{0,K}$	$s_{1,K}$	$s_{2,K}$
6.235 ± 0.1645	-2.058 ± 0.15	0.3248 ± 0.032

Table 4.15: The efficiencies of the additional requirements in the data sample selection. The efficiencies are quoted separately for pion and kaon tracks.

	θ_C cut	n_γ cut	proton rejection cut
ϵ_π	$(84.44 \pm 0.49)\%$	$(80.56 \pm 0.28)\%$	$(99.78 \pm 0.07)\%$
ϵ_K	$(85.24 \pm 0.27)\%$	$(76.24 \pm 0.29)\%$	$(99.80 \pm 0.04)\%$
ϵ_K/ϵ_π	1.009 ± 0.007	0.9464 ± 0.0049	1.0002 ± 0.0008

fractions.

4.6.2 Uncertainties on the corrections

From Eq. 4.40, we can see that the uncertainties on the corrections Δ_π and Δ_K, related to the statistics of the simulated samples, represent another contribution to the systematic error on the ratio of branching fractions. The uncertainties are propagated with the systematic errors on N_π and N_K, obtaining a contribution of 0.0017.

4.6.3 Inaccuracies in Monte Carlo simulations

The systematic uncertainty coming from inaccuracies in Monte Carlo simulations is limited by the following choices:

1. The parameters of the core Gaussians in $f_{\pi,K}$ and $h_{\pi,K}$ are extracted

Table 4.16: Yields extracted with a likelihood fit using the PID information.

	$J/\psi\,(\to \mu^+\mu^-)h^\pm$	$J/\psi\,(\to e^+e^-)h^\pm$
N_π	21.1 ± 5.2	15.5 ± 5.1
N_K	439 ± 21	377 ± 20
$N_{bkd\pi}$	175 ± 14	195 ± 14
N_{bkdK}	62.1 ± 8.4	93 ± 10

Table 4.17: Original (N_i) and corrected yields (N_i^{eff}) for the signal components.

sample	i	N_i	N_i^{eff}
$J/\psi\,(\to \mu^+\mu^-)h^\pm$	π	21.1 ± 5.2	21.9 ± 5.2
	K	439 ± 21	441 ± 21
$J/\psi\,(\to e^+e^-)h^\pm$	π	15.5 ± 5.1	16.5 ± 5.1
	K	377 ± 20	379 ± 20

from the fit.

2. The parameters of the tail Gaussian in $f_{\pi,K}$ are expressed in terms of the parameters of the core Gaussian; only the "scaling factors" $m_l - m_n$ and σ_l/σ_n are determined from simulations.

3. The requirements $|\Delta E_\pi| < 120\,\mathrm{MeV}$ and $|\Delta E_K| < 120\,\mathrm{MeV}$, used to select the data sample, are very soft, both for $B^\pm \to J/\psi\,\pi^\pm$ and for $B^\pm \to J/\psi\,K^\pm$ events. Therefore the efficiency of these requirements is weakly dependent on possible inaccuracies in the description of the ΔE_π and ΔE_K distributions.

In order to estimate the systematic error due to any residual effects, we have performed the fit on a sample simulated with broader ΔE resolution. The sample has been selected from 15,000 $B^\pm \to J/\psi\,\pi^\pm$ and 43,000 $B^\pm \to J/\psi\,K^\pm$ events. We have performed the fit using also the nominal simulation, and the ratio between the extracted yields N_π and N_K in the two cases is computed. The systematic error has been estimated as half of the difference of the two ratios, obtaining a negligible contribution.

Table 4.18: Measurements of $\mathcal{B}(B^\pm \to J/\psi\,\pi^\pm)/\mathcal{B}(B^\pm \to J/\psi\,K^\pm)$ obtained with the original (fit 1) and a modified likelihood function (fit 2) that includes particle identification for $h^\pm$.

sample	fit 1	fit 2	Δ/σ_Δ
$J/\psi\,(\to \mu^+\mu^-)h^\pm$	$(4.2 \pm 1.0)\%$	$(4.7 \pm 1.1)\%$	1.1
$J/\psi\,(\to e^+e^-)h^\pm$	$(3.5 \pm 1.2)\%$	$(4.1 \pm 1.3)\%$	1.2

Table 4.19: Contributions to the systematic error on the ratio of branching fractions.

Source	$\sigma_{sys}[\mathcal{B}(B^\pm \to J/\psi\,\pi^\pm)/\mathcal{B}(B^\pm \to J/\psi\,K^\pm)]$
PDFs parameterization	0.0007
Δ_π and Δ_K corrections	0.0017
MC inaccuracies	$< 10^{-4}$
TOT.	0.0019

4.6.4 Total systematic error

Table 4.19 summarizes the several contributions to the systematic error on the ratio of branching fractions. They have been added quadratically to obtain the total systematic error.

4.7 Summary

We have measured the ratio of branching fractions $\mathcal{B}(B^\pm \to J/\psi\,\pi^\pm)/\mathcal{B}(B^\pm \to J/\psi\,K^\pm)$, analyzing a data set corresponding to an integrated luminosity of $20.7\,\mathrm{fb}^{-1}$. We have observed 51 ± 10 $B^\pm \to J/\psi\,\pi^\pm$ events, and the ratio of branching fractions has been determined to be:

$$\frac{\mathcal{B}(B^\pm \to J/\psi\,\pi^\pm)}{\mathcal{B}(B^\pm \to J/\psi\,K^\pm)} = [3.91 \pm 0.78(stat.) \pm 0.19(syst.)]\%\,. \tag{4.41}$$

Chapter 5

Search for direct CP-violation in $B^{\pm} \to J/\psi\,\pi^{\pm}$ and $B^{\pm} \to J/\psi\,K^{\pm}$ decays

In this chapter we describe a study of direct CP-violation in the $B^{\pm} \to J/\psi\,\pi^{\pm}$ and $B^{\pm} \to J/\psi\,K^{\pm}$ channels. Using an approach similar to the one developed for the ratio of branching fractions measurement, we determine at one time the CP-violating charge asymmetry observables $\mathcal{A}_{\pi}$ and $\mathcal{A}_{K}$. The asymmetry observable $\mathcal{A}_{K}$ is also determined with a "cut-based" analysis.

Since in the Standard Model the $B^{\pm} \to J/\psi\,K^{\pm}$ mode is not expected to show significant direct CP-violation, it is used as a control mode to test the analysis procedure. Furthermore, any evidence of CP-asymmetry in this channel would represent a clue to New Physics.

No previous measurements are available for the $B^{\pm} \to J/\psi\,\pi^{\pm}$ channel. A search for direct CP-violation in $B^{\pm} \to J/\psi\,K^{\pm}$ decays was performed by the CLEO collaboration, obtaining no evidence of asymmetry [42]:

$$\mathcal{A}_{K} = 0.018 \pm 0.043\,(stat.) \pm 0.004\,(syst.)\,. \tag{5.1}$$

The data set considered for this study is the same one of the $\mathcal{B}(B^{\pm} \to J/\psi\,\pi^{\pm})/\mathcal{B}(B^{\pm} \to J/\psi\,K^{\pm})$ measurement, corresponding to an integrated luminosity of $20.7\,\mathrm{fb}^{-1}$.

5.1 Cut-based analysis for $\mathcal{A}_K$ determination

This analysis is based on the reconstruction and selection of a sample of $B^\pm \to J/\psi\,K^\pm$ events. We determine the CP-asymmetry observable as:

$$\mathcal{A}_K = \frac{N^- - N^+}{N^- + N^+}\,, \tag{5.2}$$

where N^+ and N^- are the extracted yields for the two charge-conjugate channels.

5.1.1 Events selection

We reconstruct a $B^\pm \to J/\psi\,K^\pm$ candidate as the combination of a J/ψ candidate and a charged track, as described in Section 4.1. The kaon mass hypothesis is assigned to the track. In addition, we use as kaon candidates only tracks in a fiducial volume where an accurate modeling of the detector material is available ($0.41 < \theta_{lab} < 2.54\,rad$), and for which the tracking efficiency is accurately measured. For this reason the kaon candidate must include at least 12 DCH hits, must have $p_T > 100\,\mathrm{MeV}/c$, and point back to the nominal interaction point within $1.5\,cm$ in the xy-plane and $3\,cm$ along the z-axis.

The final selection of the B candidates is made according to the values of ΔE and of the energy substituted mass m_{ES} (see Section 4.1.3). We require $|\Delta E| < 120\,\mathrm{MeV}$ and $m_{ES} > 5.2\,\mathrm{GeV}/c^2$; if more than one candidate is selected per event, then the one with the lowest $|\Delta E|$ is chosen. Figure 5.1 shows the distributions of the selected $B^- \to J/\psi\,K^-$ and $B^+ \to J/\psi\,K^+$ candidates in the $(\Delta E, m_{ES})$ plane.

The $(\Delta E, m_{ES})$ plane is divided in several regions. We define the ΔE signal region as $|\Delta E| < 3\sigma(\Delta E)$, and the ΔE sideband as $|\Delta E| > 4\sigma(\Delta E)$, where $\sigma(\Delta E)$ is the energy resolution for $B^\pm \to J/\psi\,K^\pm$ events, determined from data (see Table 4.3); we take into account differences in the resolution for $J/\psi\,(\to \mu^+\mu^-)h^\pm$ and $J/\psi\,(\to e^+e^-)h^\pm$ events. Table 5.1 summarizes the definitions. The candidates in the signal box are defined as the candidates belonging to the ΔE signal region and with $5.27 < m_{ES} < 5.29\,\mathrm{GeV}/c^2$; this cut on m_{ES} corresponds to the requirement $|m_{ES} - M_{B^\pm}| < 3\sigma(m_{ES})$, where $M_{B^\pm}$ is the $B^\pm$ mass as reported by the PDG [8], and $\sigma(m_{ES})$ is the resolution in m_{ES} determined from data (see Table 4.3).

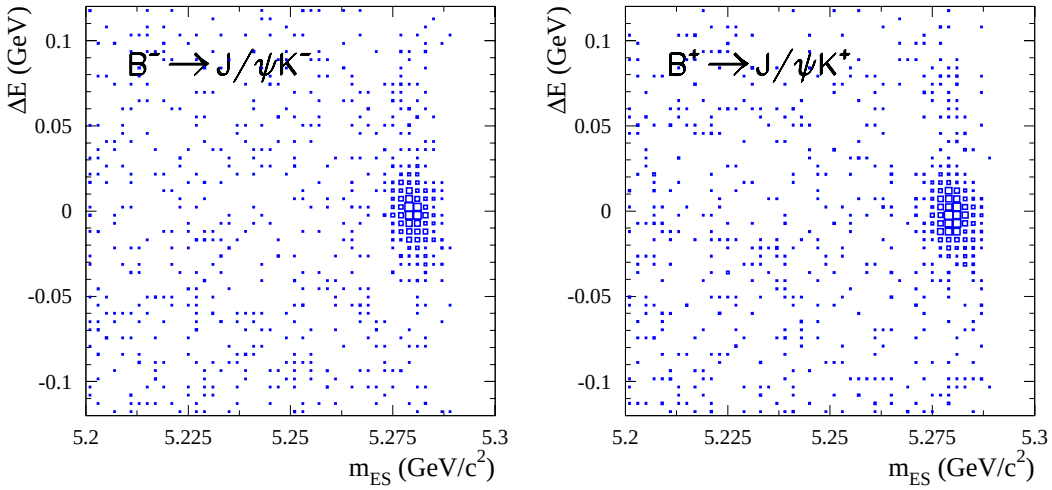

Figure 5.1: The ΔE vs. m_{ES} distribution for the selected $B^- \to J/\psi K^-$ (left plot) and $B^+ \to J/\psi K^+$ (right plot) candidates.

Table 5.1: Definitions of the ΔE signal region and the ΔE sideband for the data sample.

	$J/\psi(\to \mu^+\mu^-)h^\pm$	$J/\psi(\to e^+e^-)h^\pm$
ΔE signal region	$\lvert\Delta E\rvert < 30.3\,\mathrm{MeV}$	$\lvert\Delta E\rvert < 38.4\,\mathrm{MeV}$
ΔE sideband	$\lvert\Delta E\rvert > 40.4\,\mathrm{MeV}$	$\lvert\Delta E\rvert > 51.2\,\mathrm{MeV}$

As it will be described in Section 5.1.3, we determine the $B^\pm \to J/\psi K^\pm$ yields fitting the distributions in m_{ES} of the events in the ΔE signal region.

5.1.2 Tracking efficiency correction

Neglecting possible charge asymmetries in tracking efficiency can be the source of a systematic error in our measurement. Indeed, denoting with $\langle\epsilon^-_{trk}\rangle_K$ ($\langle\epsilon^+_{trk}\rangle_K$) the tracking efficiency for negative (positive) particles averaged over the kaon spectrum in $B^\pm \to J/\psi K^\pm$ decays, the condition:

$$\langle\epsilon^-_{trk}\rangle_K \neq \langle\epsilon^+_{trk}\rangle_K \tag{5.3}$$

implies that the correct expression for the asymmetry observable is:

$$\mathcal{A}_K = \frac{N^- - r_K \cdot N^+}{N^- + r_K \cdot N^+} \,, \tag{5.4}$$

in which the quantity r_K is defined as:

$$r_K = \frac{\langle \epsilon^-_{trk} \rangle_K}{\langle \epsilon^+_{trk} \rangle_K} \,. \tag{5.5}$$

In order to take into account possible charge asymmetries due to the tracking, the distributions to fit are re-weighted by the tracking efficiencies (measured as explained in Section 2.2.1). Each entry in a distribution is weighted by a quantity $w^\pm(p_T, m, \theta, \phi)$ defined as:

$$w^\pm(p_T, m, \theta, \phi) = \frac{1}{\epsilon^\pm_{trk}(p_T, m, \theta, \phi)} \,, \tag{5.6}$$

where the variables (p_T, m, θ, ϕ) refer to the kaon candidate and denote its transverse momentum, the track multiplicity in the event, its polar and azimuthal angles. Charge-dependent tracking efficiency tables reporting $\epsilon^\pm_{trk}$ measured in bins of (p_T, m, θ, ϕ) are used in this procedure. There are 5610 bins in each table: 11 bins in p, 17 bins in m, 10 bins in θ, and 3 bins in ϕ. If the yields are extracted fitting the re-weighted distributions, the asymmetry observable is still given by Eq. 5.2.

In order to express in a compact formula the number of entries in each bin of a re-weighted distribution, we use the following notations:

1. the indices i and j are associated to generic bins of the distribution;
2. the index k is associated to a generic bin of the tracking efficiency table;
3. w_k is the weight from the k-th bin of the tracking efficiency table ($w_k = 1/\epsilon_{trk}(k)$);
4. m_{ik} ($m_{ik} = 0, 1, 2, \dots$) is the number of entries in the i-th bin of the original distribution that have been re-weighted by w_k.

The number of entries N^0_i in the i-th bin of the original distribution is given by:

$$N^0_i = \sum_k m_{ik} \,, \tag{5.7}$$

while the number of entries N_i in the i-th bin of the re-weighted distribution is:

$$N_i = \sum_k m_{ik} w_k \,. \tag{5.8}$$

The uncertainty associated to N_i is given by:

$$\sigma^2(N_i) = \sum_k m_{ik} w_k^2 + m_{ik}^2 \sigma^2(w_k) \,, \tag{5.9}$$

where the component linear in m_{ik} represents the contribution from the Poissonian uncertainty of the bin content, and the component quadratical in m_{ik} represents the contribution from the statistical uncertainty of the tracking efficiencies:

$$\sigma^2(w_k) = \sigma^2[\epsilon_{trk}(k)] \cdot w_k^4 \,. \tag{5.10}$$

5.1.3 Yields determination

Figure 5.2 shows the original m_{ES} distributions for the 736 $B^- \to J/\psi K^-$ and 742 $B^+ \to J/\psi K^+$ candidates in the ΔE signal region. After the re-weighting procedure we obtain the distributions in Fig. 5.3: in this case we have 779.1 $B^- \to J/\psi K^-$ and 785.4 $B^+ \to J/\psi K^+$ candidates.

We fit simultaneously the re-weighted distributions with the sum of an ARGUS and a Gaussian function (see Fig. 5.4): the ARGUS function (defined in Eq. 4.6) describes the background component, while the Gaussian function describes the signal peak. The events under each Gaussian represent the yields of the charge conjugate signals. In the fit we constrain the widths of the two Gaussians to be equal. We also constrain the shape parameters of the two ARGUS functions to be equal. If the fit is performed without this constraint (see Fig. 5.5) we obtain consistent values of the shape parameters.

5.1.4 Peaking background

As discussed in Section 4.3.2, a fraction of background events from other $B \to J/\psi X$ decays does not distribute in m_{ES} according to an ARGUS function, but is described by a Gaussian peak around the $B^\pm$ mass. Denoting

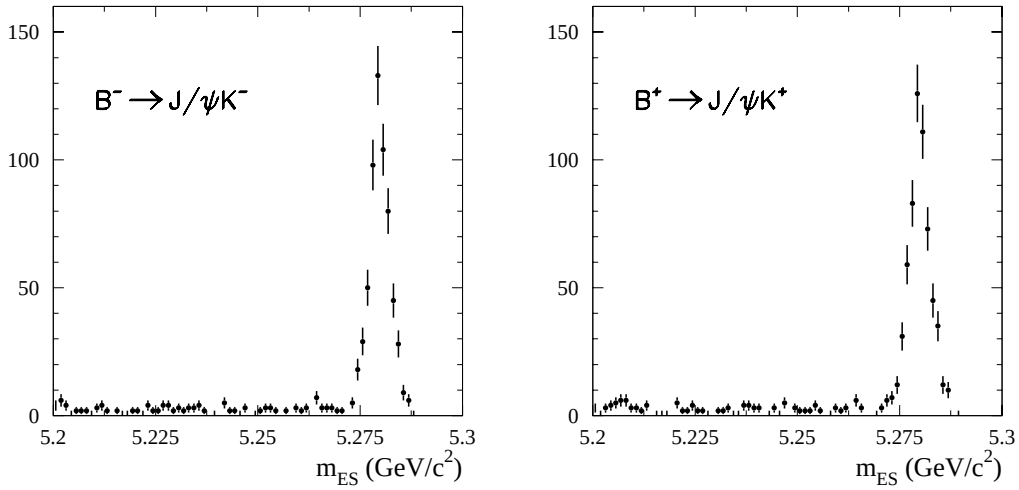

Figure 5.2: The m_{ES} distributions for the $B^- \to J/\psi\,K^-$ (left plot) and $B^+ \to J/\psi\,K^+$ (right plot) candidates in the ΔE signal region. There are 736 $B^- \to J/\psi\,K^-$ and 742 $B^+ \to J/\psi\,K^+$ candidates.

with N_{pk} the number of peaking background events in the ΔE signal region, their subtraction leads to the following formula for the asymmetry observable:

$$\mathcal{A}_K = \frac{N^- - N^+}{N^- + N^+ - N_{pk}}\,. \tag{5.11}$$

In the above equation we have assumed that the peaking background is charge-symmetrical; this assumption is discussed in Section 5.1.8, where also the corresponding systematic error is computed.

The number of peaking background events N_{pk} is estimated with a fit to the m_{ES} distribution in the ΔE signal region for simulated inclusive J/ψ events (with the $B^{\pm} \to J/\psi\,K^{\pm}$ component subtracted) that have passed the same selection of the data sample. The distribution is fitted with the sum of a Gaussian and an ARGUS function (see Fig. 5.6). A sample corresponding to an equivalent luminosity of $83.8\,\mathrm{fb}^{-1}$ has been used. Scaling to $20.7\,\mathrm{fb}^{-1}$ we obtain: $N_{pk} = 6.2 \pm 2.4$.

5.1.5 Statistical uncertainty on the extracted yields

Since the same weight can be applied to entries in different bins i and j, the errors on the yields receive an additional contribution from the off-diagonal

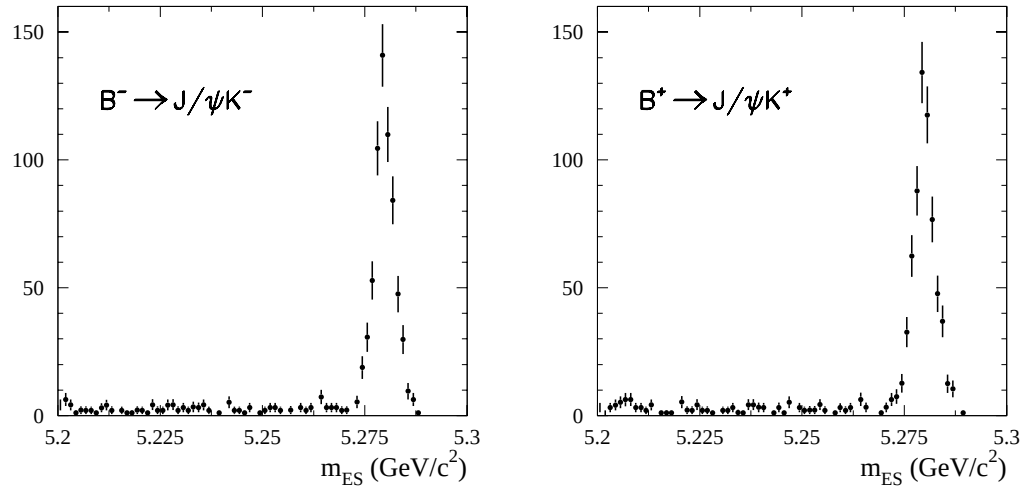

Figure 5.3: The re-weighted m_{ES} distributions for the $B^- \to J/\psi K^-$ (left plot) and $B^+ \to J/\psi K^+$ (right plot) candidates in the ΔE signal region. There are 779.1 $B^- \to J/\psi K^-$ and 785.4 $B^+ \to J/\psi K^+$ candidates.

terms of the covariance matrix S_{ij}:

$$S_{ij} = \begin{cases} \sum_k m_{ik} m_{jk} \sigma^2(w_k) & (i \neq j) \\ \\ \sigma^2(N_i) & (i = j)\,. \end{cases} \tag{5.12}$$

We have computed the elements of S_{ij} according to Eq. 5.12 and have estimated the separate contributions to $\sigma^2(N)$ in the following way:

1. contribution from statistical fluctuations of the bins content:

$$\sigma_P^2(N) = \sum_i \sum_k m_{ik} w_k^2\,; \tag{5.13}$$

2. contribution from uncorrelated errors on N_i:

$$\sigma_u^2(N) = \sum_i \sum_k m_{ik}^2 \sigma^2(w_k)\,; \tag{5.14}$$

3. contribution from correlations between N_i and N_j:

$$\sigma_c^2(N) = \sum_{i \neq j} \sum_k m_{ik} m_{jk} \sigma^2(w_k)\,. \tag{5.15}$$

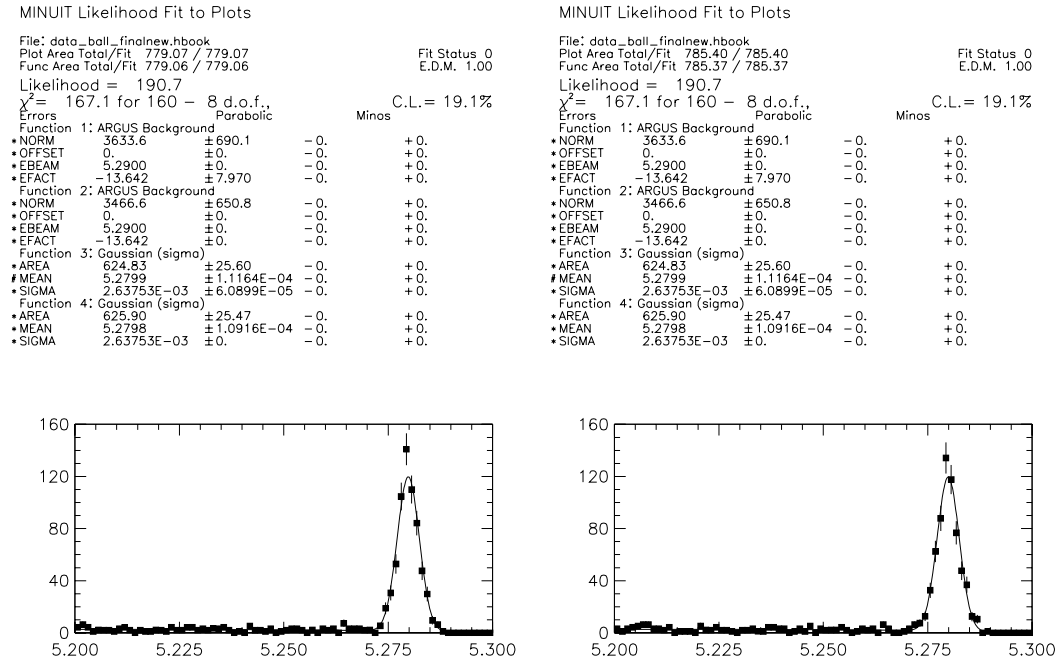

Figure 5.4: The fit to the re-weighted m_{ES} distributions for the $B^- \to J/\psi\,K^-$ (left plot) and $B^+ \to J/\psi\,K^+$ (right plot) events in the ΔE signal region; each distribution is fitted with the sum of an ARGUS and a Gaussian function; the shape parameters ("EFACT") of the ARGUS functions are constrained to assume the same value.

In all the above sums the indices i and j are restricted to the bins corresponding to $5.27 < m_{ES} < 5.29\,\mathrm{GeV}/c^2$. Table 5.2 summarizes the results of our estimates. It is evident that $\sigma_P^2(N)$ represents the dominant contribution to the errors on the yields.

5.1.6 CP-asymmetry measurement

Table 5.3 summarizes the yields and the level of the background under the signal (estimated integrating the fitted ARGUS function in the signal box). We determine the CP-asymmetry observable to be:

$$\mathcal{A}_K = 0.001 \pm 0.030\,, \tag{5.16}$$

where the error is statistical only.

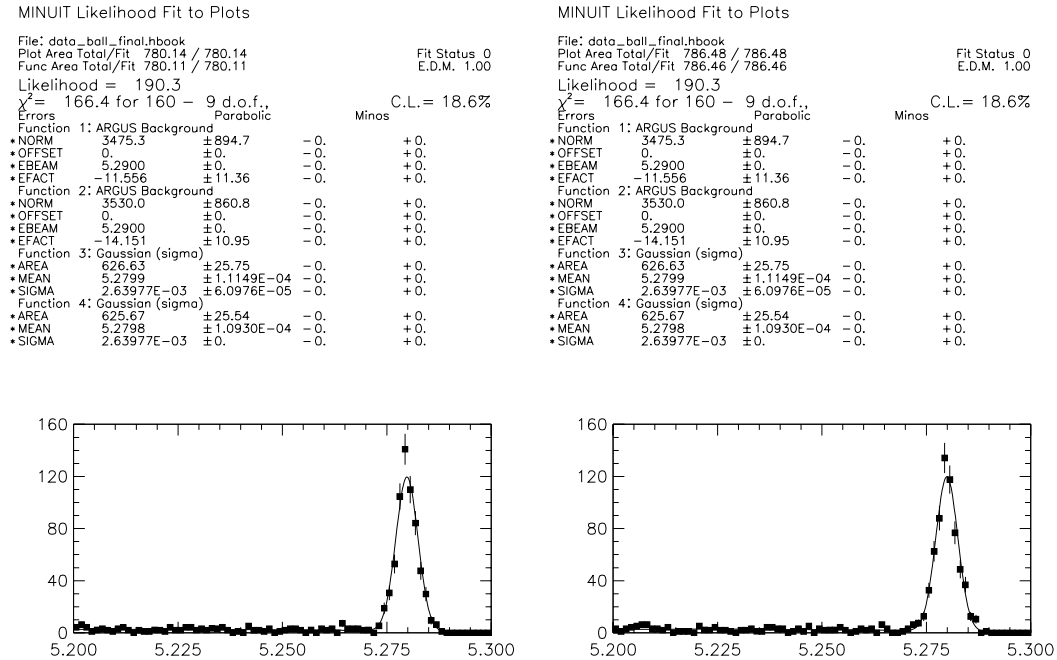

Figure 5.5: The fit to the m_{ES} distributions for the $B^- \to J/\psi K^-$ (left plot) and $B^+ \to J/\psi K^+$ (right plot) candidates in the ΔE signal region; each distribution is fitted with the sum of an ARGUS and a Gaussian function; no constraints are applied between the shape parameters ("EFACT") of the ARGUS functions.

5.1.7 Tests on simulated samples

The analysis procedure described in the previous sections has been tested on Monte Carlo simulations of generic $b\bar{b}$ and inclusive J/ψ events. We apply the same reconstruction and selection criteria of the data sample. The m_{ES} distributions for the events in the ΔE signal region are corrected for tracking efficiency as described in Section 5.1.2, and are fitted with the sum of an ARGUS and a Gaussian function (see Fig. 5.7 and Fig. 5.8). Table 5.4 summarizes the estimated yields and asymmetries. There is no evidence of significant charge asymmetry for the fitted yields.

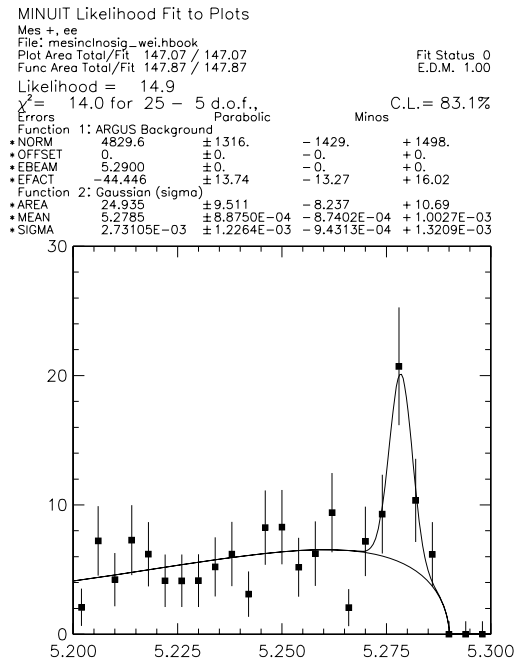

Figure 5.6: The fit to the m_{ES} distribution for simulated inclusive J/ψ events (with the $B^{\pm} \to J/\psi\,K^{\pm}$ component subtracted) in the ΔE signal region.

5.1.8 Systematic uncertainties

Differences in K^+ vs. K^- detection efficiency

Kaons that interact inelastically in the detector material before the DCH could be undetected. For this reason, the different cross-sections for nuclear interactions of K^+ and K^- represent a source of fake charge asymmetry in our measurement. This effect is not reflected in the tracking efficiency tables used for the re-weighting, because of the dominance of the pion component in the sample of tracks used for the tracking efficiency determination. In order to estimate this fake asymmetry, we have performed a calculation based on the values of the cross-sections for nuclear interactions as a function of momentum [43]. We use an accurate model of the detector material before the DCH, and a simplified model of the geometry of the detector.

Let us consider N_0 kaons traversing a layer of material of thickness x; the

Table 5.2: Breakdown of the contributions to the statistical uncertainty on N^- and N^+.

	N^-	N^+
$\sigma_P^2(N)$	682.7	688.3
$\sigma_u^2(N)$	0.103	0.055
$\sigma_c^2(N)$	0.0024	0.0039
$\sqrt{\sigma_P^2(N)+\sigma_u^2(N)+\sigma_c^2(N)}$	26.24	26.13

Table 5.3: Estimated yields and background under the signal peak.

	N^-	N^+
yields	626 ± 26	625 ± 26
background	20 ± 5	21 ± 5

number of kaons N that pass through it without interacting will be given by:

$$N = N_0 e^{-x/\lambda} \,, \tag{5.17}$$

where λ is the mean free path between inelastic interactions. In our calculation all the lengths are expressed in $g/\,cm^2$ and λ is estimated as:

$$\lambda^{-1} = \frac{N_A}{A}\sigma(p)A^{0.7} \,, \tag{5.18}$$

where N_A is the Avogadro constant, A is the atomic weight of the material and $\sigma(p)$ is the inelastic kaon-nucleon cross-section, as a function of the momentum p of the kaon; the factor $A^{0.7}$ takes into account the dependency of the cross-section on the atomic number of the material. The detector elements contributing to the amount of material are schematized as 9 cylindrical layers, each one with a certain thickness l. Table 5.5 summarizes the parameters used in the calculation. It is worthwhile to note that the actual thickness traversed by a kaon is a function of its polar angle:

$$x = l/\sin\theta \,. \tag{5.19}$$

We divide the (p, θ) space in 120 two-dimensional bins: 20 bins in p from 1 to 3 GeV/c and six bins in θ (bin edges: 20°, 40°, 60°, 80°, 100°, 120°, 150°). The fraction $f_j(p_j, \theta_j)$ of kaons in the j-th bin is obtained from Monte

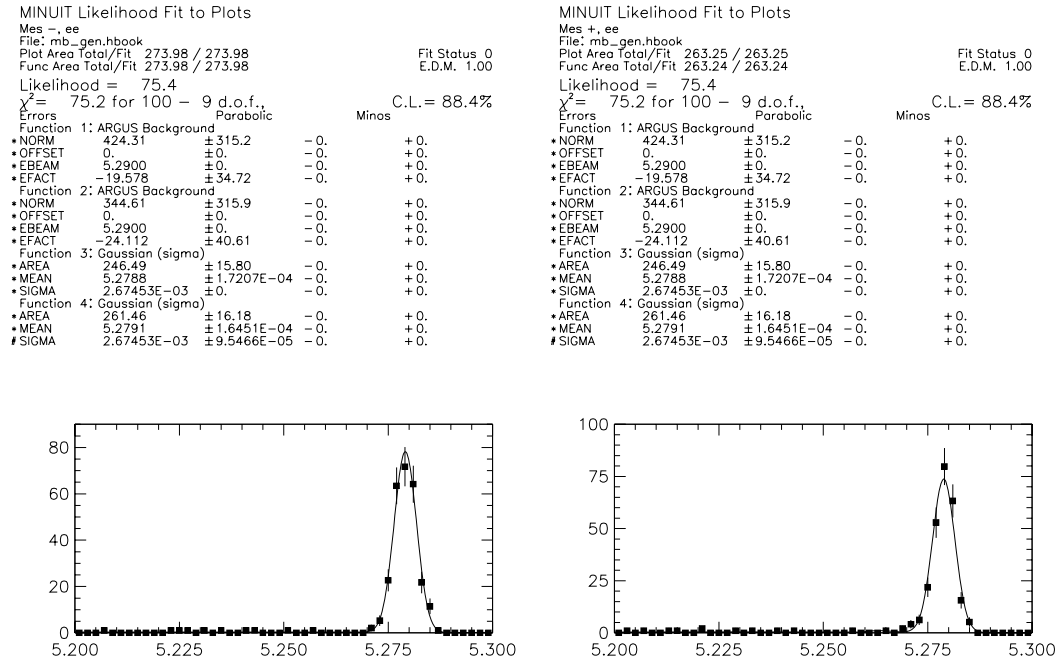

Figure 5.7: The fit to the m_{ES} distributions for generic $b\overline{b}$ events selected as the data sample. (left plot): B^- candidates in the ΔE signal region; (right plot): B^+ candidates in the ΔE signal region.

Carlo simulations of $B^{\pm} \to J/\psi\,K^{\pm}$ events. We compute the fraction of kaons passing through the material without interacting as:

$$F_K^{\pm} = \sum_j a_j^{\pm} f_j \ , \tag{5.20}$$

where $a_j^{\pm}$ is the suppression factor for the j-th bin:

$$a_j^{\pm} = \prod_{i=1}^{9} e^{-x_i(\theta_j)/\lambda_i^{\pm}(p_j)} \ . \tag{5.21}$$

In the above equation the index i runs over the detector elements in Table 5.5. Finally, the fake asymmetry $\mathcal{A}_F$ is given by:

$$\mathcal{A}_F = \frac{F_K^- - F_K^+}{F_K^- + F_K^+} \ . \tag{5.22}$$

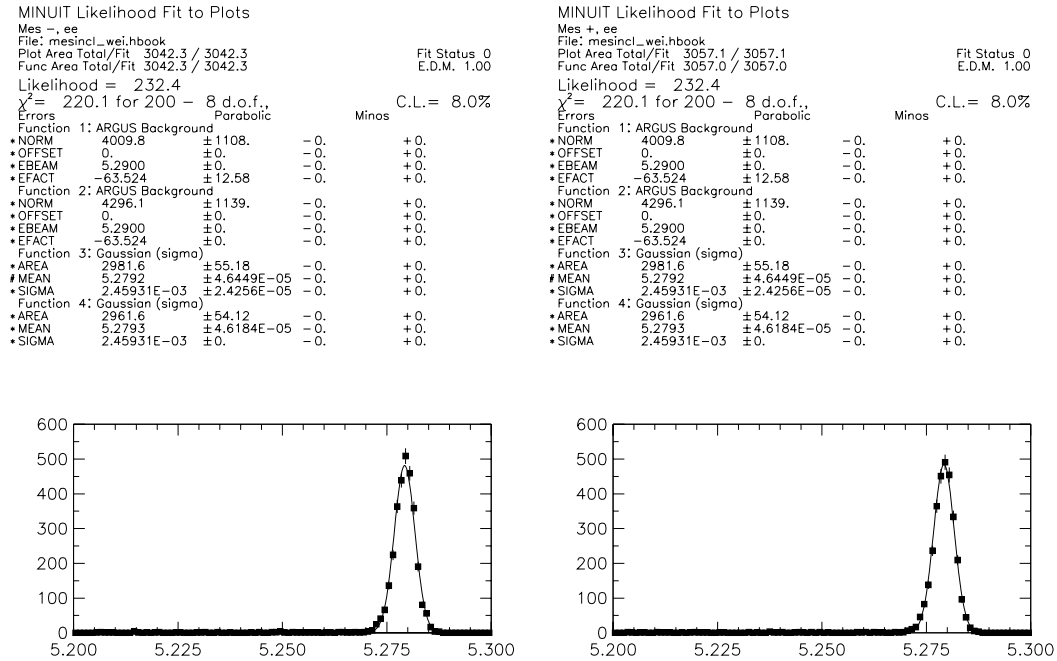

Figure 5.8: The fit to the m_{ES} distributions for inclusive J/ψ events selected as the data sample. (left plot): B^- candidates in the ΔE signal region; (right plot): B^+ candidates in the ΔE signal region.

We estimate $F_K^- = 0.9878$ and $F_K^+ = 0.9956$, obtaining:

$$\mathcal{A}_F = -0.0039\,. \tag{5.23}$$

We correct our CP-asymmetry determination by $-\mathcal{A}_F$ and assign $|\mathcal{A}_F|$ as a contribution to the systematic error.

Peaking background asymmetry

An asymmetry of the peaking background in the ΔE signal region adds a contribution to the measured $\mathcal{A}_K$. Indeed, writing $\mathcal{A}_K$ as:

$$\mathcal{A}_K = \frac{(N^- - N_{pk}^-) - (N^+ - N_{pk}^+)}{N^- + N^+ - N_{pk}}\,, \tag{5.24}$$

and using:

$$\mathcal{A}_{pk} = \frac{(N_{pk}^- - N_{pk}^+)}{N_{pk}}\,, \tag{5.25}$$

Table 5.4: Summary of the tests performed on simulated samples.

	N^-	N^+	$\mathcal{A}$
generic $b\overline{b}$	261 ± 17	246 ± 16	0.030 ± 0.046
inclusive J/ψ	2962 ± 54	2982 ± 55	-0.003 ± 0.013

Table 5.5: Model of the detector material before the DCH. For each layer of material we report its thickness l and the atomic weight A.

Detector element	Material	l (g/cm^2)	A
Beam pipe	Au	0.008	196.967
	Be	0.157	9.012
	Ni	0.008	58.693
	H_2O	0.147	18.015
	Ni	0.008	58.693
	Be	0.094	9.012
SVT	Si	0.350	28.086
Support tube	C	0.460	12.011
DCH support	Be	0.185	9.012

we have:

$$\mathcal{A}_K = \frac{N^- - N^+}{N^- + N^+ - N_{pk}} - \frac{\mathcal{A}_{pk} \times N_{pk}}{N^- + N^+ - N_{pk}} \,. \tag{5.26}$$

If the peaking background is charge-symmetrical the second term vanishes and we obtain Eq. 5.11.

In our determination of the CP-asymmetry we have assumed that the peaking background is charge-symmetrical. This assumption has been verified with the study of the m_{ES} distributions for the events in the ΔE sideband (defined in Table 5.1). We fit each distribution with the sum of a Gaussian and an ARGUS function and constrain the widths of the two Gaussians to have the same value as the signal Gaussians. In addition, we constrain the shape parameters of the ARGUS functions to be equal (see Fig. 5.9). We obtain $N^- = 38.2 \pm 8.5$, $N^+ = 38.1 \pm 8.2$, with no evidence of charge asymmetry of the peaking background within the error:

$$A_{pk} = 0.00 \pm 0.15 \,. \tag{5.27}$$

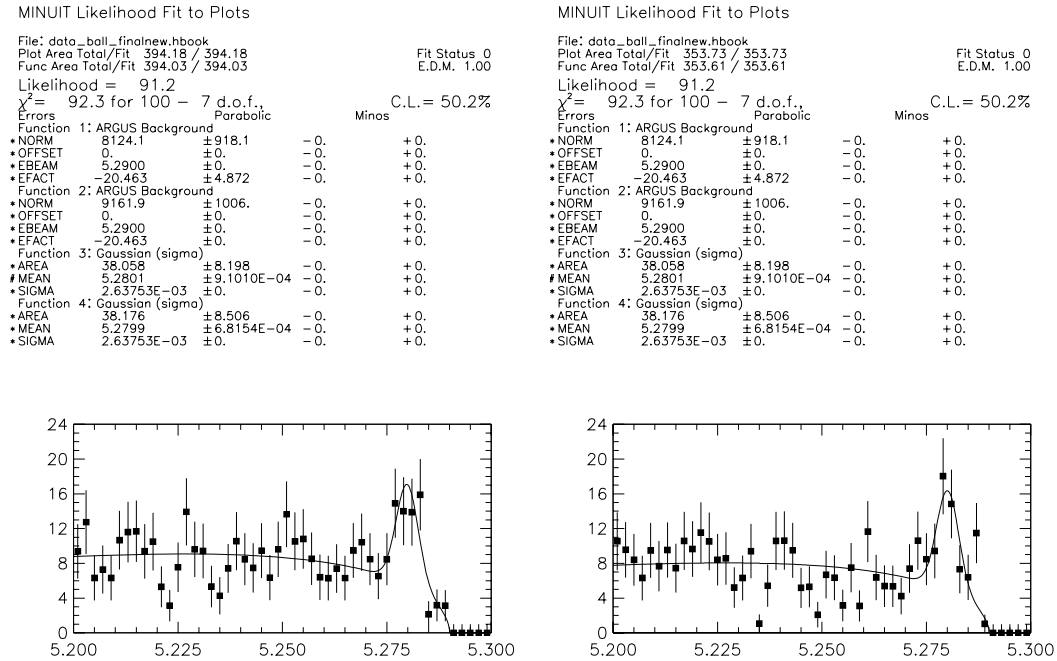

Figure 5.9: The fit to the m_{ES} distribution for the B^- (left plot) and the B^+ (right plot) candidates in the ΔE sideband.

The uncertainty on $\mathcal{A}_{pk}$ adds a contribution to the systematic error:

$$\sigma_{sys}^{pk} = \sigma(\mathcal{A}_{pk}) \times \frac{N_{pk}}{N^- + N^+ - N_{pk}} \,. \tag{5.28}$$

Using $N_{pk} = 6.2 \pm 2.4$ and $\sigma(\mathcal{A}_{pk}) = 0.15$, we obtain:

$$\sigma_{sys}^{pk} = 0.0008 \,. \tag{5.29}$$

Statistical uncertainty on N_{pk}

The statistical uncertainty on the value of N_{pk} gives a negligible contribution (1.5×10^{-6}) to the systematic error.

Total systematic error

Table 5.6 summarizes the several contributions to the systematic error. They are quadratically summed to obtain the total systematic error. We obtain:

$$\sigma_{sys}^{TOT} = 0.004 \tag{5.30}$$

Table 5.6: Contributions to the systematic error.

	σ_{sys}
K^+ vs. K^- detection efficiency	0.0039
Peaking background asymmetry	0.0008
Peaking background stat. uncertainty	$< 10^{-5}$
TOT.	0.004

5.1.9 Results

We have searched for direct CP-violation in $B^\pm \to J/\psi\,K^\pm$ decays with a "cut-based" analysis. No evidence of CP-violation has been found, in agreement with the expectation from the Standard Model. The measured CP-violating charge asymmetry is:

$$\mathcal{A}_K = 0.005 \pm 0.030(stat.) \pm 0.004(syst.)\,. \tag{5.31}$$

5.2 Unbinned likelihood fit-based analysis.

This analysis is based on the approach developed for the $\mathcal{B}(B^\pm \to J/\psi\,\pi^\pm)/\mathcal{B}(B^\pm \to J/\psi\,K^\pm)$ measurement and described in the previous chapter. We reconstruct and select a sample of $B^\pm \to J/\psi\,h^\pm$ ($h = \pi, K$) events and define the charge asymmetry observables $\mathcal{A}_\pi$, $\mathcal{A}_K$, $\mathcal{A}_{bkd}$ as:

$$\mathcal{A}_i = \frac{N_i^- - N_i^+}{N_i^- + N_i^+} \qquad i = \pi, K, bkd\,, \tag{5.32}$$

where $N_\pi^\pm$, $N_K^\pm$ and $N_{bkd}^\pm$ are the yields for the $J/\psi\,\pi^\pm$, the $J/\psi\,K^\pm$, and the background component in the sample respectively. The asymmetry observables are determined performing an unbinned maximum likelihood fit to the selected data sample.

5.2.1 Events selection

The reconstruction and selection of the B candidates has already been described in Section 4.1. In addition, the track h must be in the fiducial volume $0.41 < \theta_{lab} < 2.54\,rad$ and must satisfy the requirements described in Section 5.1.1. Finally, we define the variables ΔE_π, ΔE_K and the energy

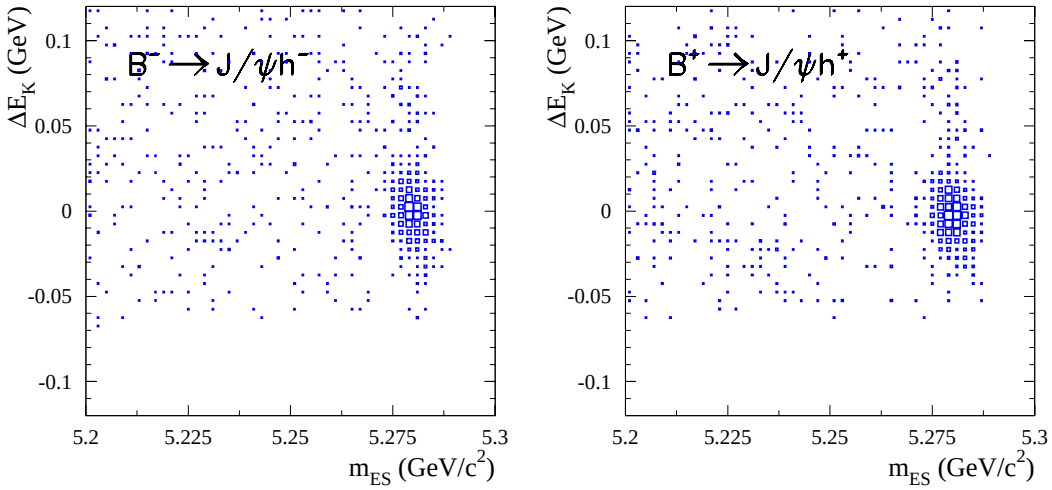

Figure 5.10: The distribution of the data sample in the $(m_{ES}, \Delta E_K)$ plane.

substituted mass m_{ES} (see Section 4.1.3) and require $|\Delta E_\pi| < 120\,\text{MeV}$, $|\Delta E_K| < 120\,\text{MeV}$, and $m_{ES} > 5.2\,\text{GeV}/c^2$. Figure 5.10 shows the distribution in the $(m_{ES}, \Delta E_K)$ plane of the selected 982 $B^- \to J/\psi\, K^-$ and 970 $B^+ \to J/\psi\, K^+$ candidates.

5.2.2 Likelihood function

The *CP*-violating charge asymmetries $\mathcal{A}_\pi$, $\mathcal{A}_K$ and $\mathcal{A}_{bkd}$ are determined with an unbinned maximum likelihood fit to the data sample. We have maximized a likelihood function L' similar to the likelihood in Eq. 4.10:

$$L'(N_i) = e^{-\sum_i N_i} \prod_{j=1}^{M} \sum_i P'_i(\Delta E_\pi^j, \Delta E_K^j, {m_{ES}}^j, q^j)\, N_i \,, \tag{5.33}$$

where j is the index of the event, i is the index of the hypothesis ($i = \pi, K, bkd$), $N_i = N_i^+ + N_i^-$, and M is the total number of events in the data sample. The arguments of the P'_i PDFs are the kinematical variables $(\Delta E_\pi, \Delta E_K, m_{ES})$ and the charge q of the final-state charged hadron. We factorize the P'_i PDFs as:

$$P'_i(\Delta E_\pi, \Delta E_K, m_{ES}, q) = P_i(\Delta E_\pi, \Delta E_K, m_{ES})\, c_i(q) \,, \tag{5.34}$$

Table 5.7: Quantities determined from the likelihood fit. The parameters p_i^{ee} ($i = \pi, K, bkd$) represent the fraction of $J/\psi(\to e^+e^-)h^\pm$ events in a certain hypothesis. The parameters m_n and σ_n are the mean and width of the ΔE resolution function; M and σ_M are the mean and width of the m_{ES} resolution function. These parameters are doubled because we allow for different values for $J/\psi(\to e^+e^-)h^\pm$ and $J/\psi(\to \mu^+\mu^-)h^\pm$ events; in addition, we allow for different values of m_n and M for $B^+ \to J/\psi\,h^+$ and $B^- \to J/\psi\,h^-$ events.

Parameters	#
N_i	3
$\mathcal{A}_i$	3
p_i^{ee}	3
m_n	$1 \times 2 \times 2$
σ_n	1×2
M	$1 \times 2 \times 2$
σ_M	1×2
TOT.	21

where $c_i(q)$ represents the probability for the final state charged hadron in a certain event hypothesis to have charge q. The $c_i(q)$ PDFs can be expressed in terms of the asymmetry observables A_i:

$$c_i(q) = \frac{1}{2}[(1 - A_i)f^+(q) + (1 + A_i)f^-(q)]\,, \tag{5.35}$$

where the functions $f^\pm(q)$ are defined as:

$$f_\pm(q) = \begin{cases} 1 & if\ q = \pm 1 \\ \\ 0 & if\ q = \mp 1\,. \end{cases} \tag{5.36}$$

The $P_i(\Delta E_\pi, \Delta E_K, m_{ES})$ are the PDFs in Eq. 4.10, characterized as described in Section 4.3.2.

We perform the fit to the entire data sample of 1952 candidates. The parameters determined from the likelihood fit are summarized in Table 5.7.

5.2.3 Tests on simulated samples

The reliability of the fit for the determination of the asymmetry has been tested on simulated samples of known compositions. They are constituted by

Table 5.8: Results of the fit to simulated samples of known composition. The two samples differ for the background source: sample 1 uses continuum + generic $b\overline{b}$ events, while sample 2 uses inclusive J/ψ events.

	Sample 1		Sample 2	
	Expected	Fitted	Expected	Fitted
N_π	50	53.1 ± 8.4	188	191 ± 14
N_K	1000	996 ± 32	3754	3744 ± 57
N_{bkd}	301	302 ± 18	368	375 ± 19
$\mathcal{A}_\pi$	-0.08	0.05 ± 0.16	0.000	0.025 ± 0.083
$\mathcal{A}_K$	-0.036	-0.043 ± 0.032	-0.007	-0.013 ± 0.016
$\mathcal{A}_{bkd}$	0.030	0.031 ± 0.060	0.044	0.093 ± 0.057

Table 5.9: Fitted asymmetry $\mathcal{A}_K$ as a function of the expected asymmetry in sample 2.

Expected $\mathcal{A}_K$	Fitted $\mathcal{A}_K$
0	-0.009 ± 0.016
0.25	0.243 ± 0.016
0.50	0.491 ± 0.014
0.75	0.740 ± 0.012

a mix of signal and background events that have passed the same selection of the data sample. In each simulated sample there is a definite background source: continuum $q\overline{q}$ ($q = u, d, s, c$) and generic $b\overline{b}$ ("sample 1"), and inclusive J/ψ ("sample 2"). The $B^\pm \to J/\psi\,\pi^\pm$ and $B^\pm \to J/\psi\,K^\pm$ events in each sample are in the ratio of $\sim 5\%$.

The asymmetries $\mathcal{A}_i$ determined with the likelihood fit are compared with the known charge asymmetries of the components in the samples. Table 5.8 summarizes the results of the tests: we do not have any significant disagreement of the fit results with the expected asymmetries.

Table 5.9 shows the value of the fitted asymmetry $\mathcal{A}_K$ in sample 2 as a function of the expected asymmetry of the $B^\pm \to J/\psi\,K^\pm$ component. The fitted asymmetry reproduces the expected asymmetry within the error.

Table 5.10: The results of the fit to the data sample.

	π	K	bkd
N_i	43.1 ± 9.0	1190 ± 36	719 ± 29
$\mathcal{A}_i$	0.01 ± 0.22	-0.001 ± 0.030	0.018 ± 0.039
p_i^{ee}	0.48 ± 0.11	0.467 ± 0.015	0.562 ± 0.020

Table 5.11: Parameters of the PDFs extracted from the fit.

	m_n (MeV)	σ_n (MeV)	M (GeV/c^2)	σ_M (MeV/c^2)
$J/\psi\,(\to \mu^+\mu^-)h^+$	-1.8 ± 0.6	9.3 ± 0.3	5.2799 ± 0.0001	2.39 ± 0.07
$J/\psi\,(\to \mu^+\mu^-)h^-$	-0.6 ± 0.6	9.3 ± 0.3	5.2799 ± 0.0001	2.39 ± 0.07
$J/\psi\,(\to e^+e^-)h^+$	-2.4 ± 0.8	11.0 ± 0.5	5.2799 ± 0.0001	2.71 ± 0.09
$J/\psi\,(\to e^+e^-)h^-$	-0.2 ± 0.8	11.0 ± 0.5	5.2797 ± 0.0001	2.71 ± 0.09

5.2.4 Fit results

Table 5.10 reports the fitted yields and asymmetries for the data sample, while Table 5.11 reports the values of the fitted PDFs parameters. We obtain:

$$\mathcal{A}_\pi = 0.01 \pm 0.22 \tag{5.37}$$

$$\mathcal{A}_K = -0.001 \pm 0.030\,, \tag{5.38}$$

where the error is statistical only. Figure 5.11 shows the probability contour plot for the asymmetry observables $\mathcal{A}_\pi$ and $\mathcal{A}_K$. The correlation coefficient ρ_{A_π,A_K} between the asymmetries is -0.032.

In order to estimate the confidence level of the fit, we have considered 2000 simulated samples. The number of $J/\psi\,\pi^{\pm}$, $J/\psi\,K^{\pm}$, and background events in each sample is extracted from Poissonian distributions, having the measured yields as mean. The values of $(\Delta E_\pi, \Delta E_K, m_{ES})$ for each event are extracted from the PDFs used in the likelihood fit. The charge q for each event is alternatively $+1$ and -1. For each sample we have evaluated $-\ln\max(L)$, which is distributed as in Fig. 5.12. We compute the confidence level of the fit (58.6%) as the fraction of events with $-\ln\max(L)$ greater than the value observed for the data sample.

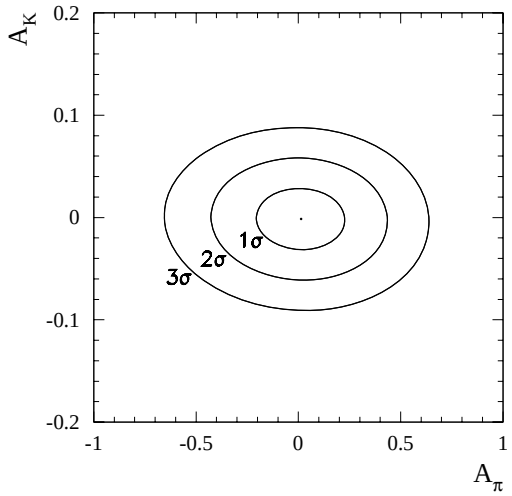

Figure 5.11: The probability contour plot for the asymmetries $\mathcal{A}_\pi$ and $\mathcal{A}_K$. The curves correspond to 1, 2 and 3 standard deviations.

5.2.5 Systematic uncertainties

PDFs parameterizations

The uncertainties on the fixed parameters of the PDFs represent a source of systematic error on the asymmetries. We have varied each of these parameters by $\pm 1\sigma$, and have repeated the likelihood fit. For each PDF, the standard deviation of the new results with respect to the observed asymmetries is assumed as a contribution to the systematic uncertainty on $\mathcal{A}_\pi$ and $\mathcal{A}_K$. The contributions due to the parameter r (fraction of the events under the core Gaussian of the signal) and R (fraction of the peaking background events) are estimated separately.

The several contributions have been quadratically added to give the total systematic errors on $\mathcal{A}_\pi$ and $\mathcal{A}_K$, obtaining $\sigma_{sys}^{PDF}(\mathcal{A}_\pi) = 0.0056$ and $\sigma_{sys}^{PDF}(\mathcal{A}_K) = 1.9 \times 10^{-4}$.

Tracking efficiency corrections

The fitted asymmetries $\mathcal{A}_i^{fit}$ in Eq. 5.37 and Eq. 5.38 do not take into account possible charge asymmetries in tracking efficiency. Denoting with $\langle \epsilon_{trk}^{\pm} \rangle_\pi$ ($\langle \epsilon_{trk}^{\pm} \rangle_K$) the tracking efficiencies averaged over the pion (kaon) spec-

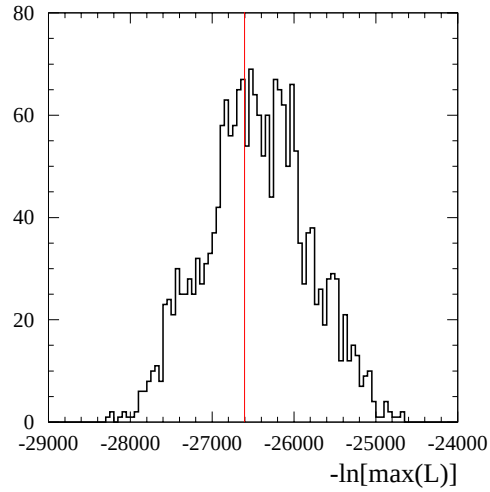

Figure 5.12: The distribution of $-\ln\max(L)$ for 2000 simulated samples. The vertical line marks the value of the $-\ln\max(L)$ for the data sample.

trum in $B^\pm \to J/\psi\,\pi^\pm$ ($B^\pm \to J/\psi\,K^\pm$) decays, the condition:

$$\langle\epsilon^-_{trk}\rangle_i \neq \langle\epsilon^+_{trk}\rangle_i \qquad (i = \pi, K)\,, \tag{5.39}$$

implies that the correct expression for the asymmetry observables is:

$$\mathcal{A}_i = \frac{(1+r_i)\mathcal{A}_i^{fit} + (1-r_i)}{(1-r_i)\mathcal{A}_i^{fit} + (1+r_i)} \qquad (i = \pi, K)\,, \tag{5.40}$$

in which the quantity r_i is defined as:

$$r_i = \frac{\langle\epsilon^-_{trk}\rangle_i}{\langle\epsilon^+_{trk}\rangle_i} \qquad (i = \pi, K)\,. \tag{5.41}$$

In order to compute $\langle\epsilon^-_{trk}\rangle_i$ and $\langle\epsilon^+_{trk}\rangle_i$ we have used the tracking efficiency tables mentioned in Section 5.1.2. Monte Carlo simulations of $B^\pm \to J/\psi\,\pi^\pm$ ($B^\pm \to J/\psi\,K^\pm$) events are used to obtain the fraction of events with the pion (kaon) characterized by a value of (p_T, m, θ, ϕ) in the m-th bin of the table. Denoting this fraction of events with $f_\pi(m)$ ($f_K(m)$), we compute:

$$\langle\epsilon^\pm_{trk}\rangle_i = \sum_m f_i(m)\,\epsilon^\pm_{trk}(m)\,, \tag{5.42}$$

and the corresponding uncertainty:

$$\sigma^2(\langle\epsilon^{\pm}_{trk}\rangle_i) = \sum_m f_i^2(m)\,\sigma^2[\epsilon^{\pm}_{trk}(m)] + \sigma^2[f_i(m)]\,[\epsilon^{\pm}_{trk}(m)]^2\,. \tag{5.43}$$

The first term in the above sum represents the contribution from the statistical uncertainty on the tracking efficiency measurements, while the second term represents the contribution from the statistics of the simulated samples. They contribute to the error on r_i:

$$\frac{\sigma^2(r_i)}{r_i^2} = \frac{\sigma^2(\langle\epsilon^{+}_{trk}\rangle_i)}{\langle\epsilon^{+}_{trk}\rangle_i^2} + \frac{\sigma^2(\langle\epsilon^{-}_{trk}\rangle_i)}{\langle\epsilon^{-}_{trk}\rangle_i^2}\,, \tag{5.44}$$

and finally to the error on $\mathcal{A}_i$:

$$\sigma^2(\mathcal{A}_i) = \left|\frac{\partial\mathcal{A}_i}{\partial\mathcal{A}_i^{fit}}\right|^2 \times \sigma^2(\mathcal{A}_i^{fit}) + \left|\frac{\partial\mathcal{A}_i}{\partial r_i}\right|^2 \times \sigma^2(r_i)\,. \tag{5.45}$$

Thus, the first term in the sum of Eq. 5.43 affects the statistical error on $\mathcal{A}_i$, while the second term is considered a contribution to the systematic error on the asymmetry measurement. We obtain:

$$r_\pi = 0.9972 \pm 0.0052 \tag{5.46}$$

$$r_K = 1.0006 \pm 0.0041\,. \tag{5.47}$$

The errors on r_π and r_K are due to the statistics of the simulated samples, while the contribution of the statistical uncertainty on the tracking efficiency measurements is negligible (3×10^{-4}).

The correction to the fitted asymmetries and their statistical precision is negligible. The contributions to the systematic error due to the statistics of the simulated samples are:

$$\sigma^{MC}_{sys}(\mathcal{A}_\pi) = 0.0026 \tag{5.48}$$

$$\sigma^{MC}_{sys}(\mathcal{A}_K) = 0.0020\,. \tag{5.49}$$

Differences in K^+ vs. K^- detection efficiency

The fake asymmetry due to the different cross-sections for nuclear interactions of K^+ and K^- has been estimated in Section 5.1.8:

$$\mathcal{A}_F = -0.0039\,. \tag{5.50}$$

We correct $\mathcal{A}_K$ by $-\mathcal{A}_F$ and assign $|\mathcal{A}_F|$ as a contribution to the systematic error on $\mathcal{A}_K$.

Table 5.12: Contributions to the systematic error.

	$\sigma_{sys}(\mathcal{A}_\pi)$	$\sigma_{sys}(\mathcal{A}_K)$
PDFs parameterization	0.0056	0.0002
K^+ vs. K^- detection efficiency		0.0039
MC statistics	0.0026	0.0020
TOT.	0.0062	0.0044

Total systematic error

Table 5.12 summarizes the several contributions to the systematic error on $\mathcal{A}_\pi$ and $\mathcal{A}_K$. They are quadratically summed to obtain the total systematic errors:

$$\sigma_{sys}^{TOT}(\mathcal{A}_\pi) = 0.006 \tag{5.51}$$

$$\sigma_{sys}^{TOT}(\mathcal{A}_K) = 0.004\,. \tag{5.52}$$

5.2.6 Results

We have searched for direct CP-violation in the $B^{\pm} \to J/\psi\,\pi^{\pm}$ and $B^{\pm} \to J/\psi\,K^{\pm}$ channels with an unbinned likelihood fit approach. The measured CP-violating charge asymmetries are:

$$\mathcal{A}_\pi = 0.01 \pm 0.22(stat.) \pm 0.006(syst.) \tag{5.53}$$

$$\mathcal{A}_K = 0.003 \pm 0.030(stat.) \pm 0.004(syst.)\,. \tag{5.54}$$

5.3 Summary

We have analyzed a data set corresponding to an integrated luminosity of $20.7\,\mathrm{fb}^{-1}$ to search for direct CP-violation in the $B^{\pm} \to J/\psi\,\pi^{\pm}$ and $B^{\pm} \to J/\psi\,K^{\pm}$ channels. The CP-violating charge asymmetries are determined to be:

$$\mathcal{A}_\pi = 0.01 \pm 0.22(stat.) \pm 0.006(syst.) \tag{5.55}$$

$$\mathcal{A}_K = 0.003 \pm 0.030(stat.) \pm 0.004(syst.)\,. \tag{5.56}$$

The asymmetry in $B^{\pm} \to J/\psi\, K^{\pm}$ decays can be compared with the result from a "cut-based" analysis:

$$\mathcal{A}_K = 0.005 \pm 0.030(stat.) \pm 0.004(syst.)\,. \tag{5.57}$$

No evidence of direct CP-violation has been found, which is in agreement, for the $B^{\pm} \to J/\psi\, K^{\pm}$ channel, with the Standard Model expectation.

Conclusions

In this thesis a study of the non-leptonic decay $B^{\pm} \to J/\psi\,\pi^{\pm}$ has been presented. The analysis is based on data collected at *BABAR* in 1999-2000, for an equivalent luminosity of $20.7\,\mathrm{fb}^{-1}$.

The ratio of branching fraction $\mathcal{B}(B^{\pm} \to J/\psi\,\pi^{\pm})/\mathcal{B}(B^{\pm} \to J/\psi\,K^{\pm})$ has been determined with an approach based on a maximum likelihood fit to a reconstructed sample of $B^{\pm} \to J/\psi\,h^{\pm}$ ($h = \pi, K$) decays. A signal of 51 ± 10 $B^{\pm} \to J/\psi\,\pi^{\pm}$ events is observed, and the ratio $\mathcal{B}(B^{\pm} \to J/\psi\,\pi^{\pm})/\mathcal{B}(B^{\pm} \to J/\psi\,K^{\pm})$ is determined to be:

$$\frac{\mathcal{B}(B^{\pm} \to J/\psi\,\pi^{\pm})}{\mathcal{B}(B^{\pm} \to J/\psi\,K^{\pm})} = [3.91 \pm 0.78(stat.) \pm 0.19(syst.)]\%\,,$$

which is in agreement with previous measurements (but with a substantially lower uncertainty), and with theoretical expectations.

Using the same approach, the *CP*-violating charge asymmetry observables for the $B^{\pm} \to J/\psi\,\pi^{\pm}$ and $B^{\pm} \to J/\psi\,K^{\pm}$ decays have been determined to be:

$$\begin{aligned} \mathcal{A}_{\pi} &= 0.01 \pm 0.22(stat.) \pm 0.006(syst.) \\ \mathcal{A}_{K} &= 0.003 \pm 0.030(stat.) \pm 0.004(syst.)\,. \end{aligned}$$

These results are consistent with no direct *CP*-violation in these channels, and confirm the Standard Model expectation for $B^{\pm} \to J/\psi\,K^{\pm}$ decays. The determination for the $B^{\pm} \to J/\psi\,K^{\pm}$ channel can be also compared with the result from an analysis based on an alternative ("cut-based") approach:

$$\mathcal{A}_{K} = 0.005 \pm 0.030(stat.) \pm 0.004(syst.)\,.$$

All the measurements reported here are affected by a systematic error which is much smaller than the statistical error, therefore new data being accumulated by *BABAR* will allow further improvements.

Bibliography

[1] S.L. Glashow, Nucl. Phys., **22** (1961) 579.

[2] S. Weinberg, Phys. Rev. Lett., **19** (1967) 1264.

[3] A. Salam, Elementary Particle Theory (ed. N. Svartholm), Almqvist and Wiksell (1968).

[4] M. Kobayashi e T. Maskawa, Prog. Th. Phys., **49** (1973) 652.

[5] S.L. Glashow, J. Iliopoulos and L. Maiani, Phys. Rev. D, **2** (1970) 1285.

[6] N. Cabibbo, Phys. Rev. Lett., **10** (1963) 531.

[7] J.H. Christenson *et al.*, Phys. Rev. Lett., **13** (1964) 138.

[8] D.E. Groom *et al.*, Eur. Phys. Jour. C, **15** (2000) 1.

[9] L. Wolfenstein, Phys. Rev. Lett., **51** (1983) 1945.

[10] C. Jarlskog, Phys. Rev. Lett., **55** (1985) 1039.

[11] A.J. Buras, in: Probing the Standard Model of Particle Interactions, F. David and R.Gupta eds., 1988 Elsevier Science B.V., hep-ph/9806471.

[12] F.J. Gilman, K. Kleinknecht and B. Renk, Eur. Phys. Jour. C, **15** (2000) 110.

[13] Y. Grossman, Y. Nir, S. Plaszczynski and M.H. Schune, Nucl. Phys. B, **511** (1998) 69.

[14] A. Alavi-Harati *et al.*, Phys. Rev. Lett., **83** (1998) 22.

[15] G. Lüders, Ann. Phys., **2** (1957) 1.

[16] W.F. Weisskopf, E.P. Wigner, Z. Phys., **63** (1930) 54.

[17] L. Wolfenstein, Eur. Phys. Jour. C, **15** (2000) 115.

[18] Y. Nir and H. Quinn, Ann. Rev. Nucl. Part. Sci., **42** (1992) 211.

[19] *BABAR* Collaboration, B. Aubert *et al.*, submitted to Phys. Rev. Lett., hep-ex/0107013.

[20] PEP-II-An Asymmetric B Factory: Conceptual Design Report, SLAC-PUB-418 (1993)

[21] *BABAR*-Letter of Intent, SLAC-443, June 1994

[22] *BABAR*-Technical Design Report, SLAC-R-95-457, March 1995

[23] K.G. Wilson, Phys. Rev., **179** (1969) 1499.

[24] J.D. Bjorken, in: New Developments in High Energy Physics, edited by E.G. Floratos and A. Verganelakis, Nucl. Phys. B Proc. Suppl., **11** (1989) 325.

[25] M. Neubert, Phys. Rep., **245** (1994) 259

[26] N. Isgur and M.B. Wise, Phys. Lett. B, **232** (1989) 113.

[27] N. Isgur and M.B. Wise, Phys. Lett. B, **237** (1990) 527.

[28] CDF Collaboration, T. Affolder *et al.*, Phys. Rev. Lett., **85** (2000) 4668

[29] *BABAR* Collaboration, B. Aubert *et al.*, submitted to Phys. Rev. Lett., hep-ex/0107049.

[30] M. Bauer, B. Stech and M. Wirbel, Z. Phys. C, **29** (1985) 637.

[31] M. Bauer, B. Stech and M. Wirbel, Z. Phys. C, **34** (1987) 103.

[32] M. Neubert and B. Stech, in: Heavy Flavours II, World Scientific, eds. A.J. Buras and M. Linder, hep-ph/9705292.

[33] Ciuchini *et al.*, Eur. Phys. Jour. C, **9** (1999) 43.

[34] I. Dunietz, Phys. Lett. B, **316** (1993) 561.

[35] CLEO Collab., M. Bishai *et al.*, Phys. Lett. B, **369** (1996) 189.

[36] CDF Collab., F. Abe *et al.*, Phys. Rev. Lett., **77** (1996) 5176.

[37] G.C. Fox and S. Wolfram, Nucl. Phys. B, **149** (1979) 413.

[38] R. Sinkus and T. Voss, Nucl. Instr. Meth. A, **391** (1997) 360.

[39] A. Drescher *et al.*, Nucl. Instr. Meth. A, **237** (1985) 464.

[40] M. Jacob and G.C. Wick, Ann. Phys. (N.Y.), **7** (1959) 404.

[41] ARGUS Collab., H. Albrecht *et al.*, Phys. Lett. B, **185** (1987) 218.

[42] CLEO Collab., G. Bonvicini *et al.*, Phys. Rev. Lett., **84** (2000) 5940.

[43] D.E. Groom *et al.*, Eur. Phys. Jour. C, **15** (2000) 1, pag.234-235.